La Rivista del Nuovo Cimento
https://doi.org/10.1007/s40766-024-00050-3

REVIEW PAPER

Positron emission tomography: its 65 years and beyond

N. Belcari[1,2] · M. G. Bisogni[1,2] · A. Del Guerra[1,2]

Received: 13 November 2023 / Accepted: 29 December 2023

Abstract

Positron emission tomography (PET) is a well-established imaging technique for "in-vivo" molecular imaging. In this review, after a brief history of PET, its physical principles and the technology developed for bringing PET from a bench experiment to a clinically indispensable instrument are presented. The limitations and performance of the PET tomographs are discussed, both for the hardware and software aspects. The status of the art of clinical, pre-clinical and hybrid scanners (i.e., PET/CT and PET/MR) is reported. Finally, the actual trend and the recent and future technological developments are illustrated. The current version of this paper is the second edition of the original version published in 2016 (Rivista del Nuovo Cimento, Vol 39(4) 2016, pp. 156–213). The authors decided to keep the same structure of the paper, operating corrections of some typos, and adjustments. However, we added a description of the most recent PET developments that took place in the last 10 years completed with the addition of the most relevant references. These topics are now described in detail and cover the last two chapters of the paper.

This article is a revised version of https://doi.org/10.1393/ncr/i2016-10122-6.

Change summary Major revision, updated and expanded.

Change details Chapters 1 to 8 have been corrected for some typos and minor adjustments have been made. Chapter 9 has been updated and expanded reflecting the current status of PET technology and application. Chapter 9 now includes an updated review of total-body PET, organ-specific PET systems, ultra-fast timing PET, PET monitoring in particle therapy and new sections on the impact of artificial intelligence in PET and on the social, environmental and economic sustainability of PET. Some new figures in chapter 9 have also been added. Chapter 10 has been also updated and expanded. The number of references has increased from 172 to 281.

✉ N. Belcari
nicola.belcari@unipi.it

1 Dipartimento di Fisica, Università di Pisa, Pisa, Italy

2 INFN, Sezione di Pisa, Pisa, Italy

Published online: 18 March 2024

1 History of PET

Positron emission tomography (PET) is an imaging technique where a positron-emitting radiotracer is injected into the patient and spreads physiologically within the body: the radioisotope activity distribution is proportional to the drug concentration. The emitted positron annihilates with an electron in tissue, thus producing two back-to-back 511 keV photons. These two photons are detected in electronic (time) coincidence by using opposing pairs of detectors. The 3D image of the activity distribution is obtained by means of analytical or statistical reconstruction algorithms.

PET is based on several building blocks that are strictly related to various Nobel Prize Laureates in Physics, Chemistry, Physiology and Medicine. The discovery of the positron (C. D. Anderson: 1936 Nobel Laureate in Physics "for his discovery of the positron") did not only experimentally confirm the prediction of antimatter made by Dirac, but, together with the fundamental theory of the radioactive β decay, forms the theoretical basis of the PET technique. However, in order to have the proper radioisotopes to be used in medical applications it was necessary to invent a suitable accelerator to produce the so-called "physiological radioisotopes" such as ^{11}C, ^{13}N, ^{15}O and ^{18}F that are the most used β^+ emitters in PET. In this respect, Ernest Orlando Lawrence received the Nobel Prize in Physics in 1939 "for the invention and development of the cyclotron and for the results obtained with it, especially with regard to artificial radioactive elements". The next step was to understand the principle of a radiotracer, i.e., to validate the concept that "the changing of an atom in a molecule with its radioisotope will not change its chemical and biological behaviour significantly". For this discovery, György Hevesy was awarded the 1943 Nobel Prize in Chemistry. Because of this principle, the movement, distribution and concentration of a molecule can be measured by loading the molecule with a radioisotope and detecting the product of its γ or β decay. The availability of an appropriate photon detector is another fundamental step for the PET technique and this gap was filled by the discovery of the inorganic scintillator NaI:Tl made by Robert Hofstadter (Nobel Laureate in Physics in 1961). Finally to produce the 3D images, PET makes use of the reconstruction principles theoretically described by Radon, the so-called Radon transform [1]; this image reconstruction method was the same one utilized by Godfrey N. Hounsfield and Allan M. Cormack, who both received the Nobel prize in Physiology or Medicine in 1979 "for the development of computer-assisted tomography" (CAT), now called CT.

Positron emission tomography was born more than 70 years ago, when William Sweet presented the first preliminary idea of PET at the dedication of the Research Building of the Massachusetts General Hospital on May 16, 1951 [2]. In 1952, Gordon L.Brownell and William Sweet [3] built the very first prototype of a PET brain scanner that made use of two opposite NaI:Tl crystals coupled to two photomultipliers as detectors and of an ink plotter as an imaging device (Figs. 1, 2).

At Washington University in St. Louis, Michel Ter-Pogossian was a pioneer in the use of positron-emitting radioactive tracers. He and his group in 1974 developed the first "PET Unit". Because of this, he is often addressed as the "Father of PET" [4].

The next developments were carried out in the '70 by James Robertson at Brookhaven, Chris Thompson and collaborators at Montreal Neurological Institute, who built the first tomograph called Positome [5], (Fig. 3), but especially by Ed Hoff-

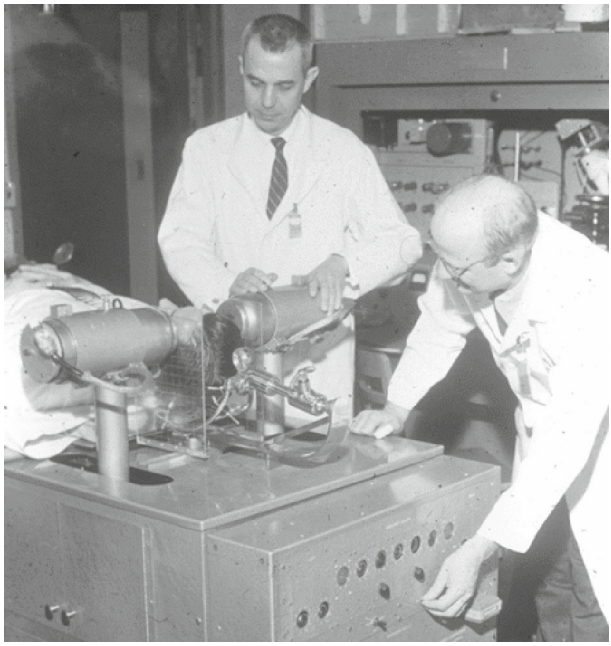

Fig. 1 Dr. G.L. Brownell (left) and Dr. Aronow are shown with the first PET scanner . (Reproduced from [3])

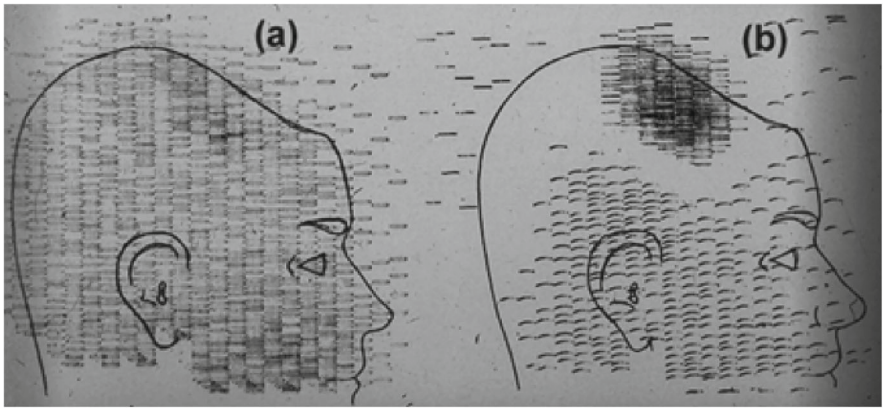

Fig. 2 Coincidence and unbalanced scans of a patient with recurring brain tumor. obtained with the first PET scanner. Coincidence scan **a** of a patient showing recurrence of tumor under previous operation site, and unbalance scan **b** showing asymmetry to the left . (Reproduced from [3])

man and Michael Phelps at UCLA, who built the first tomograph based on 48 NaI:Tl detectors that showed the potentiality of PET in Neurological studies and in Functional brain imaging (Fig. 4). The UCLA group also wrote a series of papers on the "quantitation" of PET images that are still a fundamental reference [6–11] for everyone who wants to learn about PET.

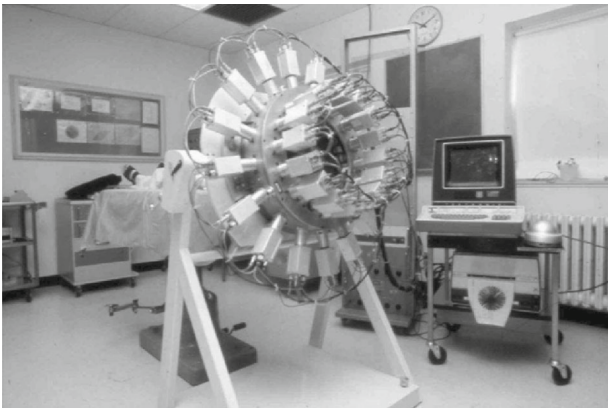

Fig. 3 Photo of the original PET scanner developed by Chris Thompson and collaborators at Montreal Neurological Institute, called Positome . (Courtesy of Christopher J Thompson, McGill University, Ca, 2015)

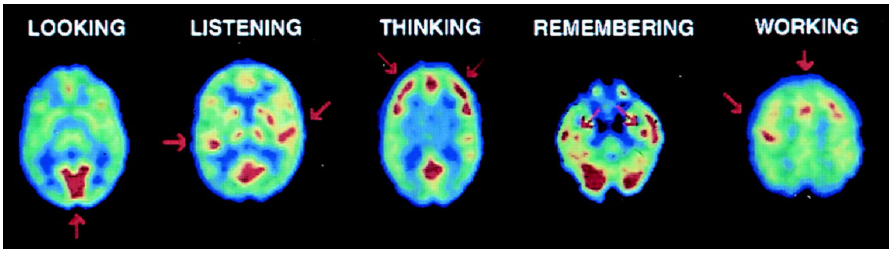

Fig. 4 PET studies of glucose metabolism (by means of ^{18}FDG) to map the human brain's response in performing different tasks. From Left to right:(LOOKING) Subjects looking at a visual scene activated visual cortex; (LISTENING) Listening to a mystery story with language and music activated left and right auditory cortices; (THINKING) Counting backwards from 100 by sevens activated frontal cortex; (REMEMBERING) Recalling previously learned objects activated hippocampus bilaterally; (WORKING) Touching thumb to fingers of right hand activated left motor cortex and supplementary motor system. Images are transaxial cross-sections of the brain with the front at the top. The highest metabolic rates are in red, with lower values from yellow to blue . (Courtesy of Drs. Michael Phelps & John Mazziotta, UCLA School of Medicine, 2015)

In 1974, the Lawrence Berkeley Laboratory (LBL) group was the first one to suggest that the Bismuth Germanate (BGO) could be an excellent crystal for PET due to its high density and high effective atomic number (Z_{eff} = 74). Soon, the BGO replaced NaI:Tl and became the crystal of election for PET for the following 20 years. The next breakthrough in PET technology was due to Mike Casey and Ronald Nutt (1986) [12] who suggested that instead of using the 1:1 coupling between one crystal and one photomultiplier (PMT), it was much more effective to use a single crystal with cuts of various depths seen by 2×2 photomultipliers (see Sect. 4.3). This detector arrangement, called *block detector* has been in use in almost all PET clinical tomographs until a few years ago with the advent of solid-state photodetectors (see Sect. 9.1.

The last technological breakthrough was the discovery of a new scintillator, the Lutetium Oxyorthosilicate (LSO:Ce) that has a similar density and Z_{eff} as BGO,

but with a much greater photon yield and faster decay time, down to 40 ns from the 300 ns of BGO (see Sect. 4.1). This provides an increased spatial, energy and time resolution with a reduction of scatter and random coincidence contribution that has allowed to move from a 2D to a 3D reconstruction over the entire Field of View (FOV) of the tomograph. Finally, the invention of the PET/CT scanner [13] was the final improvement of PET that has now become an indispensable instrument for the diagnosis, staging and prognosis of cancer. The PET/CT, attributed to David Townsend and Ronald Nutt, was named by TIME Magazine as the medical invention of the year in 2000. The next steps are the PET story of today with the introduction of the Position-Sensitive Photomultipliers (PS-PMT), Solid-State Photodetectors (APD and SiPM) and even faster scintillators: its current and future improvements will be properly illustrated in the sections of this review paper.

2 Molecular imaging

Molecular imaging is a discipline of biomedical research that has been growing rapidly in recent years. It can be defined as "the visual representation, characterization and quantification of biological processes that take place in a living being at the cellular and sub-cellular level" [14]. Therefore the images obtained reflect cellular and molecular pathways, as well as mechanisms of evolution of a pathology. To achieve this ambitious goal, molecular imaging needs the convergence of various methods of imaging of molecular and cellular biology, chemistry, medicine and pharmacology, medical physics, mathematics and computer science in a highly interdisciplinary new field of research.

Molecular imaging requires high sensitivity and high spatial resolution. The molecular processes must be monitored quantitatively and qualitatively in vivo over time. In this respect, each imaging modality presents its unique set of advantages and drawbacks. Table 1 presents a spectrum of the most common molecular imaging techniques: PET, single-photon emission computed tomography (spect), optical bioluminescence, optical fluorescence, magnetic resonance imaging (MRI) and X-ray computed tomography (CT).

The variety of optimal performance that is necessary cannot be furnished by a single technique. This suggests that more than one modality should be used, either in series or combined in one hybrid modality, e.g., PET/CT or PET/MR. These combined imaging systems will be further described in Sects. 7.1 and 9.3, respectively. Also because of this necessity of complementarity of information in medicine, a new term has been recently introduced of *personalized medicine*. "Personalised medicine can be broadly described as a customization of healthcare that accommodates individual differences as far as possible at all stages in the process, from prevention, through diagnosis and treatment, to post-treatment follow-up" [15]. Although the full discussion of personalized medicine is beyond the scope of this paper it is important to briefly address the role of medical imaging and molecular imaging in this new conception of healthcare.

Personalized medicine is based on the joint information deriving from genomic data, proteomics, pharmacogenomics, theranostic and radiogenomics, where the investigations by medical imaging and especially molecular imaging, i.e., PET, are building

Table 1 A list of the most common imaging techniques with their main performance related to molecular imaging

Imaging technique	Source of signal	Spatial resolution	Sensitivity (mol/l)	Quantitative/ morphological information
PET	γ-rays (511 keV)	1–4 mm	$10^{-11} - 10^{-12}$	+++/+
SPECT	γ-rays (<300 keV)	0.3–10 mm	$10^{-10} - 10^{-11}$	++/+
Optical bioluminescence	Visible light	3–5 mm	$10^{-15} - 10^{-17}$ (theoretical)	+(++)/n.a
Optical fluorescence	Visible light and NIR	2–3 mm	$10^{-9} - 10^{-12}$ (probable)	+(++)/n.a
MRI	Radio waves	25–100 μm	$10^{-3} - 10^{-5}$	++/+++
CT	X-rays (40–120 keV)	10–200 μm	n.a	n.a./+++

blocks of this scenario. The European Society of Radiology (ESR) has suggested using the term *precision medicine* (instead of personalized medicine), simply defined as "providing the right treatment to the right patient at the right time" [16]. Imaging is essential in personalized prevention, in the selection of treatment, and in the evaluation of the treatment response, i.e., in all steps of personalized medicine (prevention, diagnosis, therapy and follow-up). The capability of providing quantitative information and its very high sensitivity are the properties that make PET indispensable in this new field of medicine.

3 Physical principles of PET

3.1 The PET measurement

In PET, a tracer labeled with a positron (β^+) emitting radioisotope is injected into the patient. The emitted positron annihilates with an electron in tissue, thus producing two almost back-to-back 511 keV photons. These two photons are detected in time coincidence by using opposing pairs of detectors. The activity distribution of the radioisotope represents an image of the tracer distribution/concentration that provides an insight of the physiology and/or pathology of the patient. The scheme of the PET principle is depicted in Fig. 5.

The objective of a PET scan is the measurement of the activity distribution $\rho(x, y, z)$ of a β^+ emitting radioisotope. Thanks to the nearly-collinear emission of the γ-ray pair from the annihilation of the positron with an electron (Sect. 3.3) it is possible to define the line L along which the annihilation occurred. L is usually called *Line-of-Flight* or LOF.

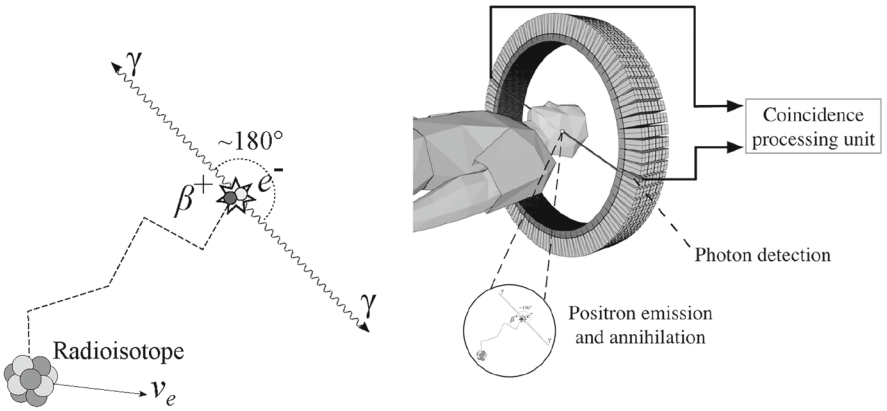

Fig. 5 Principle of PET. (Left): a positron (β^+) is emitted by a radioisotope together with an electron neutrino (ν_e). The positron slows down in tissue until it reaches thermal equilibrium and annihilates with an electron. (Right): detection of the photons in time coincidence by two opposing detectors

The activity distribution $\rho(x, y, z)$ is measured in terms of projections (N_γ) along lines L using the *line integral operator*:

$$N_{\gamma-\gamma} = k \int_L \rho(x, y, z) \mathrm{d}L. \tag{1}$$

This is an ideal model, that assumes zero positron range (Sect. 3.2), no deviation from collinearity (Sect. 3.3) and ideal behavior of the detector (Sect. 5.5). In the practical situation, the lines L are defined by all the possible lines of response (LORs) connecting a detector i to a detector j. Then, Eq. (1) can be written as

$$N_{ij} = k \int_{\mathrm{LOR}_{ij}} \rho(x, y, z) \mathrm{d}L. \tag{2}$$

3.2 Positron emission

The positron-emitting radioisotopes are atoms whose nuclei have an excess of protons with respect to the number of neutrons and decay to a stable configuration through β^+ decay:

$$_Z X \rightarrow _{Z-1} Y^* + \beta^+ + \nu_e. \tag{3}$$

The daughter nucleus can be in an excited state $_{Z-1}Y^*$ with a successive γ decay to the ground state $_{Z-1}Y$. The β^+ decay is a three-particle decay, but because of its mass, the kinetic energy of the recoil nucleus can be neglected. Hence, it is reasonable to assume that the released energy is shared between the β^+ and the ν_e. The β^+ spectrum can be calculated by fundamental quantum mechanics, starting from the decay probability per second (for a full treatise see [17]):

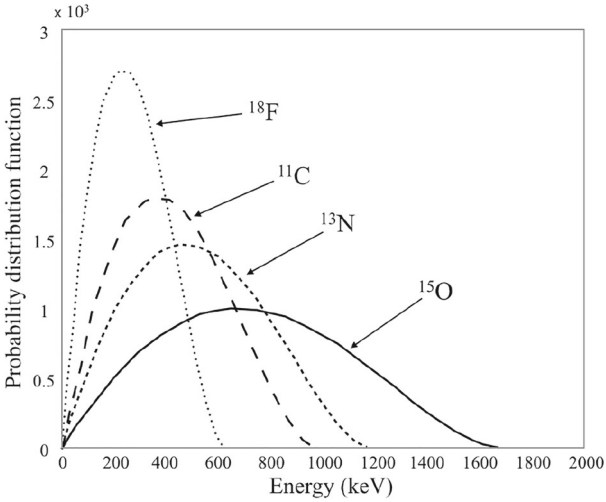

Fig. 6 β^+ spectrum of most used positron emitters radioisotopes as a function of the positron kinetic energy (from [18], chapter 8, p. 293)

$$W = \frac{2\pi}{\hbar}\left|\Psi_{\beta^+}(0)\right|^2\left|\Psi_{\nu_e}(0)\right|^2\left|\mathcal{M}\right|^2\left|g\right|^2\frac{\mathrm{d}n}{\mathrm{d}E}, \tag{4}$$

where $\left|\Psi_{\beta^+}(0)\right|$ is the expectation value of the plane wave function β^+ within the nucleus (i.e., at $r = 0$), $\left|\Psi_{\nu_e}(0)\right|$ is the expectation value of the plane wave function of the ν_e within the nucleus (i.e., at $r = 0$), $\mathcal{M}$ is the probability amplitude of the decay, g is the coupling constant of the decay, $\mathrm{d}n/\mathrm{d}E$ is the density of the final states and $2\pi/\hbar$ is a normalization factor.

After a straightforward calculation, one obtains the probability of emission of a β^+ with a momentum between p and $p + \mathrm{d}p$:

$$P(p)\mathrm{d}p = \frac{\mathcal{M}^2 g^2}{2\pi^3\hbar^7 c^3}\left[\sqrt{p_{\max}^2c^2 + m_e^2c^4} - \sqrt{p^2c^2 + m_e^2c^4}\right]p^2\mathrm{d}p, \tag{5}$$

where $p_{\max}$ is the maximum momentum of the β^+ and m_e is the mass of the β^+. The β^+ spectrum vs. momentum is symmetric with respect to its mean value and goes to 0 as p^2, both for $p \to 0$ and $p \to p_{\max}$. If one represents the same spectrum as a function of the kinetic energy and applies the proper Coulombian corrections obtains the β^+ kinetic energy spectrum as depicted in Fig. 6 for some of the most used β^+ emitter radioisotopes. $T_{\max}$ is the maximum kinetic energy of the β^+. The spectrum is now asymmetric. It is often adopted the approximation that T_{mean} is about 1/2 $T_{\max}$, as opposite to a β^- decay spectrum where T_{mean} is approximated as 1/3 $T_{\max}$.

The emission of a positron source is subjected to the standard exponential decay law:

$$N(t) = N_0 e^{-\lambda t}, \tag{6}$$

Table 2 Reactions used for $\beta+$ source production: the column of energies shows the energy of the incident projectiles; the last column refers to the number of atoms necessary to obtain an activity of 1 mCi . (Adapted from [18], chapter 8, p. 295)

Produced radioisotope	Nuclear reaction	Energy (MeV)	Atoms/mCi
^{11}C	^{14}N(p,α)^{11}C	10–20	$6.5{\cdot}10^{10}$
^{13}N	^{13}C(p,n)^{13}N	10–11	$3.2{\cdot}10^{10}$
	^{16}O(p,α)^{13}N	10–16	
^{15}O	^{14}N(d,n)^{15}O	6–10	$6.6{\cdot}10^{9}$
	^{15}N(p,n)^{15}O	10	
	^{16}O(p,pn)^{15}O	>17	
	^{16}O(^{3}He,α)^{15}O	8	
^{18}F	^{20}Ne(d,α)^{18}F	> 6	$3.5{\cdot}10^{11}$
	^{16}O(^{3}He,p)^{18}F	>8	
	^{16}O(^{4}He,pn)^{18}F	>25	
	^{18}O(p,n)^{15}O	>10	

where N_0 is the number of nuclei at $t = 0$ and λ is the decay constant of the radioisotope, i.e., the inverse of the mean-life of the decay ($\lambda = 1/\tau$). The number of disintegrations per second is defined as the source activity A:

$$A(t) = -\frac{\mathrm{d}N(t)}{\mathrm{d}t} = \lambda N(t) = \frac{1}{\tau} \cdot N(t). \tag{7}$$

The activity is measured in Becquerel (1Bq = 1 disintegration/s), but a still much used unit is the Curie ($1\text{Ci} = 3.7\times10^{10}$ Bq) and its sub-multiples. The time which is necessary to halve the number of initial radioactive nuclei is called half-life ($T_{1/2}$) and is given by $T_{1/2} = \ln 2/\lambda$. After a number n of half-lives from $t = 0$, the number of remaining radioactive nuclei N_n is given by

$$N_n = N_0 \cdot (1/2)^n. \tag{8}$$

Positron sources are not stable in nature, so they have to be artificially produced by bombarding stable isotopes with positively charged particles. Table 2 lists some of the reactions to produce the most used PET radioisotopes. The accelerator of choice is a Cyclotron with a typical proton energy of 10–20 MeV, i.e., with enough energy to overcome the Coulomb barrier of the target nuclei. The produced nucleus has a different Z value from the target nucleus; thus the two species are chemically separable.

The radioisotopes as listed in Table 2 are called physiological radioisotopes because their corresponding stable isotopes are main constituents of the human body: ^{11}C, ^{13}N, ^{15}O are in fact isotopes of ^{12}C, ^{14}N, ^{16}O, respectively. On the other hand, ^{18}F can very easily replace an oxydrile OH^-; hence it can be used to label any organic molecule. All these radioisotopes have a short lifetime. This has the advantage of using most of the activity injected into the patient during the PET examination, thus reducing

Table 3 Physical properties of the so-called physiological radioisotopes

Radioisotope	Half-life (min)	Positron average kinetic energy (MeV)	Positron kinetic energy endpoint (MeV)	Positron average range in water (mm)
^{11}C	20.4	0.385	0.960	1.2
^{13}N	10.0	0.491	1.198	1.6
^{15}O	2.0	0.735	1.732	2.8
^{18}F	109.8	0.242	0.633	0.6

the radioactive waste disposal problems and respecting the principle of a tracer that requires a minimal amount to be used. However, it has also some disadvantages, especially for the very short lifetime radioisotopes, e.g., ^{15}O: the cyclotrons for its production should be "on-site", where "on-site" means that the delivery time from production to the patient should be of the order of the radioisotope half-life. Table 3 presents the main physical properties of these radioisotopes.

3.3 Annihilation of the positron

Positrons are emitted with a kinetic energy spectrum and they lose their energy mostly through multiple Coulomb interactions in the biological tissue. This process can be described by the so-called *continuous slowing down approximation* (c.s.d.a). A competing process is bremsstrahlung which is more important at high energy. Finally, the positron reaches thermal equilibrium with the medium and then annihilation with an electron occurs. The total path of the positron is called *path length*, whereas the distance between the emission point and the position where thermal equilibrium is reached is called range [19]. The range of the positron depends on the density and Z of the medium. In water, the average range of the positrons emitted from most PET radionuclides is about 1–3 mm, as reported in Table 3. When the positron annihilation occurs with an electron of the medium, in first approximation it is assumed that both the positron and the electron are at rest. In this case, because of energy and momentum conservation, the annihilation can only generate two back-to-back γ-rays of 511 keV each. However, this is not entirely true because even if the positron has a thermal energy ($3/2KT$ =1/40 eV at 27 °C) that can be considered negligible, the electron is bound to the atom with an energy that cannot be ignored. If we consider the annihilation in the center of mass of the system, the collinearity and the equal sharing of energy is maintained. Since in the laboratory reference frame, the center of mass is not at rest, the collinearity of the two photons is lost due to the angle transformation from one reference frame to the other, the so-called *Lorentz boost*. This non-collinearity results in a Gaussian dispersion centered at 180° of about 0.5° FWHM when a positron annihilates in water. More precisely, let us consider a reference frame $R_{\text{C.M.}}$ moving with velocity v in the x direction with respect to a laboratory reference frame R_{lab} (Fig. 7).

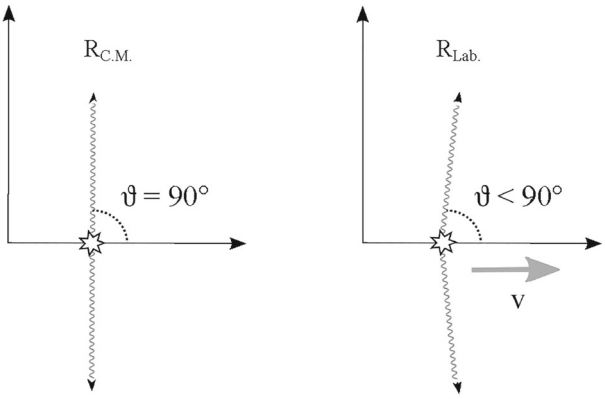

Fig. 7 Two γ's annihilation: (left) in the center of mass reference frame; (right) in the laboratory frame

The Lorentz transformation for an angle θ is given by

$$\tan\theta' = \frac{\sin\theta}{\gamma(\cos\theta + \beta)}, \tag{9}$$

where θ' is the angle between the velocity v of $R_{\text{C.M.}}$ with respect to R_{lab} and the direction of the emitted photon as seen in the laboratory reference and θ is the angle between the emitted photon and the velocity v as seen from the center of mass reference frame; γ is the relativistic factor $1/\sqrt{1-\beta^2}$ and $\beta = v/c$. A complete derivation of this formula can be found for instance in Ref. [20].

The maximum value of θ' is for $\theta = \pi/2$. In this case,

$$\tan\theta'_{\text{min}} = \frac{1}{\gamma\beta}. \tag{10}$$

As an example, if we consider an electron bound to the hydrogen atom, $\beta \simeq 1/137$, $\gamma \simeq 1$ resulting in $\tan\theta'_{\text{min}}$=137 and therefore $\theta'_{\text{min}} = 89.6°$ ($\theta = 90°$). In this situation, both photons undergo the same aberration and the minimum angle between them is no longer 180° but 179.2°.

There is also a non-negligible probability of annihilation in flight, i.e., before the positron is thermalized. This process depends mostly upon the positron energy and the surrounding medium property (density, Z). The cross-section for the annihilation of a positron in flight via 2γ emission was given by Dirac [21]:

$$\sigma_{2\gamma} = Z\pi \cdot r_0^2 \cdot \frac{1}{\gamma+1}\left[\frac{\gamma^2+4\gamma+1}{\gamma^2-1}\log\left(\gamma+\sqrt{\gamma^2-1}\right) - \frac{\gamma+3}{\sqrt{\gamma^2-1}}\right], \tag{11}$$

where r_0 is the classic radius of the electron, and, $\gamma = E/m_e c^2$ with E the positron energy given by the kinetic energy plus the rest mass. For PET radioisotopes and water as medium (approximately 70% of the human body is made of water), the in-flight

annihilation is about 2% of the entire annihilation process. An annihilation via 3γ emission is also possible, but it is usually not considered, because has a much lower probability, with a cross-section:

$$\sigma_{3\gamma} = \frac{\sigma_{2\gamma}}{372} \ll \sigma_{2\gamma}. \tag{12}$$

An extensive experimental study of the distribution of the non-collinearity of the annihilation γ-rays in water has been done by Colombino and Fiscella [22]. The experiment shows that the distribution is not a single Gaussian curve, but is the convolution of two Gaussian components with a different σ. The data were taken in a temperature range from +22 °C and − 144 °C. The two components have different behavior with temperature:

- a narrower component, $|\Delta\theta| < 4$ mrad at $\simeq$ 300 K, which is dependent on the temperature
- a broader component, $|\Delta\theta| > 4$ mrad, which is temperature-independent

The narrower component width is consistent with the calculation based on the Fermi momentum of the bound electron [23]. The broader component can only be explained with the existence of a particle in a status with a higher momentum, thus suggesting the presence of an additional phenomenon of annihilation, the decay of the positronium, a bound quantum state of the electron and positron orbiting around their center of mass. The existence of an electron–positron bound state was predicted by Mohorovicic [24], but the first theoretical calculations were only published by Pirenne [25]. Martin Deutsch reported the first experimental evidence of its formation in gas in 1951 and named *Positronium* [26]. An extensive review on positronium can be found in [27].

The broader component of the non-collinearity distribution of the two annihilation γ's is due to the higher momentum of the upper bound state of the positronium. In fact, the *electron–positron* system has two minimum energy configurations: *para-positronium*, a singlet state ^1S with opposite spin ($J = 0, \uparrow\downarrow$), and half-life in vacuum $T_{1/2} \simeq 0.1$ ns; *ortho-positronium*, a triplet state ^1P with parallel spin ($J = 1, \uparrow\uparrow$) with a half-life in vacuum $T_{1/2} \simeq$100 ns. Higher level states such as ^2S are formed very seldom. Hence, because of $J = 1$ the ortho-positronium constitutes about 3/4 of the bound states.

The para-positronium has a leading self-decay for self-annihilation (the bound system collapses) in two γ's, but the annihilation could also happen with a free electron (pick-off) that has a lifetime in the water of about 1 ns. The ortho-positronium main self-annihilation is in three photons; decays in five photons have been observed with a negligible probability. However, because its natural decay time is so long ($\simeq$ 100 ns) the 1 ns pick-off process with free electrons is preferred. A summary of the annihilation process, their characteristic, lifetime and angular deviation from collinearity in water is shown in Table 4. In summary, the dominant process is 2γ's decay with two non-collinearity behaviors: the narrow one coming from the annihilation at rest from non-bound states of the positron and from the para-positronium decay, whereas the broader deviation derives from the ortho-positronium decay via electron pick-off.

Table 4 Summary of the positron annihilation processes . (Adapted from reference [18], Chapter 8, p. 301)

State	Annihilation process	Comments	Lifetime	Angular deviation
Non-bound	In-flight via 2γ emission	Of the order of 2%, coulomb interactions and bremsstrahlung preferred	~1 ps	Narrow
	At rest via 2γ emission	Standard PET situation	~1 ns	Narrow
	At rest via 3γ emission	Improbable		
	At rest via more than 3γ emission	More and more improbable		
Positronium	Para-positronium self-annihilation	1/4 of the bound states, preferred annihilation for para-positronium	~100 ps	Narrow
	Para-positronium pick-off	Improbable	~1 ns	Narrow
	Ortho-positronium self-annihilation	Via 3γ, it is anticipated by pick-off	~100 ns	Narrow
	Ortho-positronium pick-off	3/4 of the bound states	~1 ns	Large

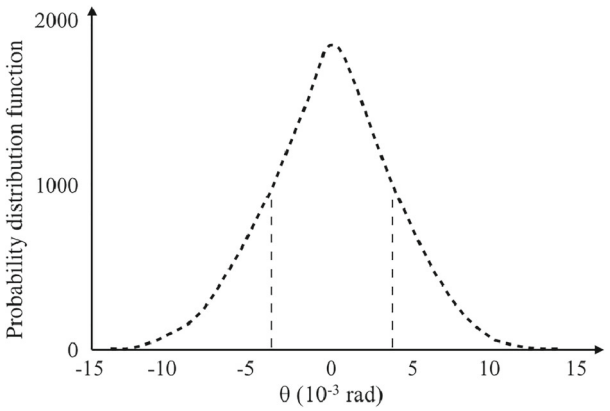

Fig. 8 Distribution of the deviation from 180° for the 2γ's annihilation in water at 4 °C. The FWHM is about 8 mrad, However, the curve has two Gaussian components: a narrow one and a large one (see text) [22]

It is usually assumed that this non-collinearity of the two photons in PET (i.e., in water) has an FWHM of about 8 mrad or approximately 5° (Fig. 8). Its effect on the PET spatial resolution has been parametrized by the empirical formula [28]:

$$\text{FWHM} = 0.0022 \times D, \tag{13}$$

where D is the distance between the pair of detectors that sensing the two γ-rays in coincidence (see Sect. 5.5).

4 Radiation detectors for PET

The basic step in a PET measurement is to obtain the spatial coordinates of the line of response where the count, corresponding to a positron emission and its further annihilation, is detected.

This can be achieved by measuring, for both γ rays, the coordinates $P(x, y, z)$ of the first interaction in a detector. Hence, the ideal PET detector must be able to: identify the position of the first interaction of a 511 keV γ-ray in the detector itself, measure the energy released in the interaction or in the series of interactions and carry information on the arrival time (at least for making the coincidence measurement possible).

Various detector technologies can be used to provide all of this information. Many technological solutions borrowed from other fields of physics have been adapted for use in PET, from wire chambers to solid-state detectors. For example, conventional wire chambers with some sort of gamma converter were proposed for PET applications. One of the most successful solutions was the so-called HIDAC camera [29]. The HIDACs are multi-wire proportional gas chambers with the addition of a conversion/multiplication structure made up of a laminated plate containing interleaved lead and insulating sheets and drilled so as to form a dense honeycomb structure. Incoming photons interact in lead layers producing Compton- and photoelectrons. If the produced electrons enter the holes they are drifted in gas by a high electric field with a velocity higher than the breakdown speed. In this way, a first avalanche multiplication is induced in gas. Further multiplication is at the arrival of the electrons in proximity to the anode wires, where the electric field is extremely intense. X and Y coordinates of the position of the photon interaction are extracted by determining the centroid of anode and cathode wire signals which are orthogonal to each other.

These systems have the capability of achieving a high spatial resolution. They were used to build a pre-clinical PET system called Quad-HIDAC-PET with an extremely high spatial resolution [30]. On the other hand, the low detection efficiency and the poor time resolution result in unacceptable limitations for the design of an effective clinical PET system.

As of today, the most reliable solution is the use of a scintillating material coupled with a photodetector.

4.1 Scintillation detectors

Scintillation detectors consist of a dense crystalline material that acts as an interacting medium. When a photon of enough energy interacts inside it and releases all or part of its energy, the scintillator emits visible light isotropically. Scintillators are available in the form of organic or inorganic compounds and can be in a solid or liquid state. The most common form of radiation detector for nuclear medicine is a solid inorganic material. The intensity of the emitted light (e.g., the number of low-energy light photons) is usually proportional to the released energy. The measure of the proportionality constant is the so-called *light yield* and is usually given in photons/MeV. Thanks to an appropriate doping material that creates energy traps between the valence band and the conduction band, the scintillator acts as a wavelength shifter from one photon of

high energy (very short wavelength) to a large number of longer wavelength photons with an emission spectrum that is characteristic for each scintillator but always in the visible or near-visible range. The emission spectrum of the scintillator has a minimal overlap with its own absorption spectrum. This means that the material is transparent to the scintillation light, thus maximizing the actual light yield that not only considers the γ-ray energy to light photons conversion efficiency but also the capability of extracting the produced light. The main advantage of the scintillator approach is that these low-energy photons can be easily detected by standard photodetectors such as photomultiplier tubes and converted to an electric current pulse. In this process, the original information on the energy released by the interacting photon is preserved. For this reason and for the relatively high stopping power $\mu_{511\text{keV}}$ (linear attenuation coefficient in the range of 0.3–1 cm^{-1} at 511 keV, for inorganic crystals) scintillators are widely used γ-ray detectors for almost all PET scanners.

An important consideration when choosing the most appropriate scintillator for PET is the compromise among different features: detection efficiency (expressed by the linear attenuation coefficient at 511 keV and related to the crystal density and effective atomic number of the material), conversion efficiency (expressed by the light yield), the output spectrum (usually indicated by the peak wavelength) and the time over which the light is emitted (the light is usually emitted with a fast light flash followed by an exponentially decaying intensity with a decay time characteristic for each scintillator, from tens to hundreds of ns). For measuring the original energy of the incident γ-ray, all the energy must be released inside the scintillator. This can happen in a single photoelectric interaction followed by a fluorescence emission or in a multiple Compton scattering process. The occurrence of one or the other modality may affect the capability of measuring the position of the first interaction as required for PET. For this reason, the relative probability between photoelectric and total interaction in the scintillating material (photofraction) is also an essential feature when choosing a PET scintillator. Table 5 reports the most widely used scintillators for PET.

For the high cost of photomultiplier tubes, solutions based on photosensitive proportional wire chambers using a gas mixture based on tetrakis-(dimethylamino)-ethylene (TMAE) were proposed in combination with BaF_2 scintillator [33]. With the advent of more cost-affordable photomultipliers and of the refinement of the block detector concept (see Sect. 4.3), the configuration scintillator/photomultiplier tube has represented for years the favorite solution for PET detectors.

4.2 Photomultiplier tubes

The use of photomultipliers is the most common way to detect and measure the light produced in a scintillating material following the γ-ray interaction. A PhotoMultiplier Tube (PMT) is a device capable of converting visible or near-visible light into an electric signal. In its simplest form, the PMT is made of a vacuum glass envelope containing a series of electrodes called dynodes. The inner surface of the glass entrance window is coated with a thin layer of a material that easily releases electrons as energy is deposited (photoelectric emission). This part of the PMT is called photocathode since it is kept at a negative potential so that electrons are accelerated away from it. The

Table 5 Properties of scintillating materials used in PET. Values adapted from [31, 32] and other sources

Material	Density g/cm^3	Light yield	Decay time (ns)	μ_{511} keV cm^{-1}	Photofraction at 511 keV (%)
Sodium iodide (NaI:Tl)	3.67	41000	230	0.34	17
Bismuth germanate (BGO)	7.13	8200	300	0.96	40
Lutetium Oxyorthosilicate (LSO:Ce)	7.40	30000	40	0.87	32
Lutetium Yttrium Oxyorthosilicate (LYSO:Ce)	7.10	32000	40	0.82	30
Gadolinium Oxyorthosilicate (GSO:Ce)	6.71	8000	60	0.70	25
Yttrium Aluminum Perovskite (YAP:Ce)	5.37	~21000	27	0.46	4.2
Lutetium Aluminum Perovskite (LuAP:Ce)	8.3	12000	18	0.95	30
Barium Fluoride (BaF_2)	4.89	1400 (fast) 9500 (slow)	0.6 (fast) 630 (slow)	0.43	
Lantanum Bromide ($LaBr_3$:Ce)	5.08	63000	16	0.47	15

probability of an electron to be emitted for each light photon reaching is called quantum efficiency (QE) and is about 15–25%. An electrostatically focusing structure drives the emitted electrons to the first dynode. Each dynode is held to a higher potential than the previous one by a voltage divider resistor chain. When stroked by an electron dynodes emit 3–4 sary electrons that are in turn accelerated to the next dynode. After 8–12 acceleration steps, depending on the number of dynodes, each generated electron produces around 10^6 secondary electrons that are collected by the anode on the opposite side of the photocathode. The anode is connected to an output wire exiting the glass envelope. The number 10^6 represents the typical amplification factor of a PMT. Thus, the PMT can be usually schematized as a source of current.

In general, when used in PET, photodetectors have to provide information on the position of the light source, i.e., the spatial coordinates of the point where the interaction occurs, on the total amount of light produced (proportional to the energy released by the γ-ray) and also on the time of the interaction.

Photomultipliers are well suited for this task having a relatively high quantum efficiency to preserve the energy information. They are fast enough with sub-ns electron

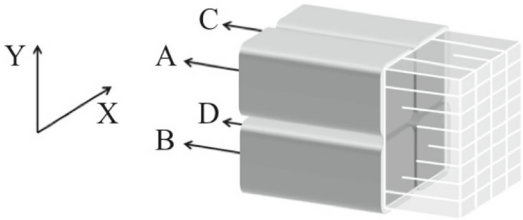

Fig. 9 Scheme of a block detector

transit time and are easy to assemble in compact position-sensitive structures such as the so-called *block detector* that was introduced for PET by M. Casey and R. Nutt in 1986 [12] and has been the chosen solution for the majority of clinical PET systems presently in use.

4.3 The block detector

Figure 9 shows a scheme of a typical block detector. A scintillator block of about 40 mm wide, 20 mm thick, originally made of BGO, is sawed up to a certain depth, into smaller elements (usually, and improperly, called pixels). The empty space between elements is filled with a white reflective material to optically separate them and to ensure the maximum efficiency in light transport toward the photodetector. The light emerging from the scintillator is sampled by four square (in its latest form) single channel PMTs arranged on a 2×2 matrix. The position of the crystal element where the interaction occurs can be derived from the four signals produced by the PMTs using a simple formula for X and Y:

$$X = \frac{(S_A + S_B) - (S_C + S_D)}{(S_A + S_B + S_C + S_D)}; Y = \frac{(S_A + S_C) - (S_B + S_D)}{(S_A + S_B + S_C + S_D)}, \tag{14}$$

where S_i is the signal produced by the ith PMT and $(S_A + S_B + S_C + S_D)$ is proportional to the total energy released in the scintillator. To ensure a good spatial linearity the saw cuts are deeper near the block sides and progressively more superficial as the cuts are close to the center.

X and Y are then the coordinates in the PMTs space and are usually stored in a 2D histogram (usually called *flood histograms*) that results in a series of peaks each corresponding to a certain pixel. This representation suffers from significant space distortion with respect to the real positions due to a poor spatial sampling. In addition, peaks are broadened due to the statistical fluctuation of the PMT signals and the possibility of having multiple interactions in the scintillator block (inter-crystal scatter events), thus resulting in some overlaps with the adjacent ones. However, pixel positions can be normally identified and well separated when pixels are not too small. The process of assigning a pair of X and Y coordinates to an event occurring in a certain pixel is called *pixel identification* and it is performed through the generation of a *look-up-table*, i.e., a series of regions are drawn around the peak positions, filling the whole histogram space. Each region is then assigned to a pixel according to its

position. Events generating a X–Y coordinated within a certain region are, in turn, assigned to that pixel.

5 The PET system

5.1 Coincidence detection

In the previous sections, we have seen how it is possible to detect and measure the position of the interaction of γ-rays. Thus, the positions of the interactions of the two γ-rays generated in a positron–electron annihilation define an LOR. The position of annihilation is then supposed to occur along this line. This process is called *electronic collimation* for the analogy with the passive collimation used in other nuclear medicine imaging techniques such as scintigraphy and SPECT.

The problem is then to recognize a pair of γ-rays as being generated by the same annihilation process. For this purpose, the information on the time of arrival of a γ-ray into the detector can be used. The two γ-rays are simultaneously generated and then, apart from some delay that may occur due to a difference in distance from the annihilation point to the two detectors, they are simultaneously detected. The selection of the annihilation γ-ray pair is made using the arrival time information. It is called detection in time coincidence or, in brief, *coincidence detection*. The event associated with the occurrence of detection in time coincidence of two γ-rays is called *coincidence event*, while in a *single event* only one γ-ray is detected. For this reason, it is important to be able to determine when a photon has struck a detector. In this way, the time of all detected events can be compared to determine which ones arrived closely enough in time to be identified as an annihilation pair. The ability of a pair of detectors to determine the time difference in arrival of the annihilation photons is known as the *coincidence time resolution* or CTR and is typically of the order of a few nanoseconds. Using a scintillator, the CTR is ultimately limited by the stochastic process in the emission of light. This uncertainty depends on the scintillator decay time and light yield. Other important parameters are the time structure of the pulse (e.g., scintillation rise time) and light transport properties of the scintillating material (including the reflection properties of the material used to separate crystal elements) affecting both light yield and pulse shape. There are various theories for the dependence of CTR from the decay time (τ_{dec}) of the scintillator and the number of light photons detected (N_{ph}) [34–36]. There is in general consensus that

$$\mathrm{CTR} \propto \frac{(\tau_{\mathrm{dec}})^{\alpha}}{\sqrt{N_{\mathrm{ph}}}}$$

where α is a constant in the $0 < \alpha < 1$ range, whose value is commonly assumed to be $\alpha = 1/2$. Hence, to have a small CTR, it is necessary to have a short decay time and a high light yield of the scintillator [37].

The maximum difference in time for a pair of detected γ-rays to be identified as a coincidence event is called *time window*. In order to avoid missing coincidence events, the time window should be at least 2 times τ. Typically, for a BGO-based

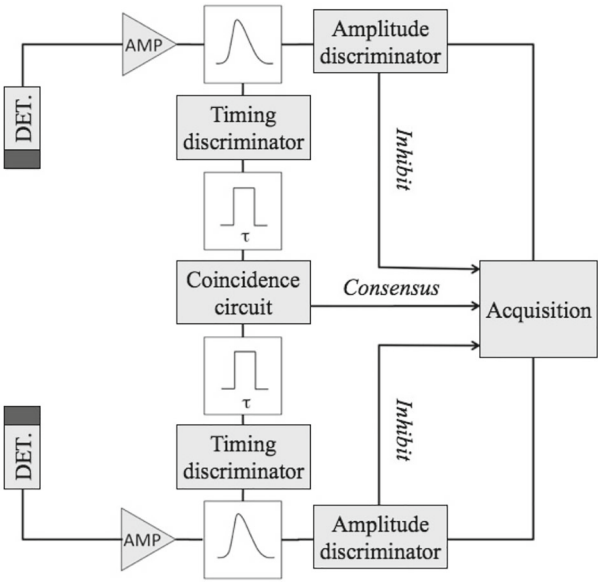

Fig. 10 Scheme of a simplified data acquisition system for a PET with two detectors only

PET system, τ is approximately 5–6 ns FWHM while for LSO it is reduced down to 2–3 ns. In addition, it must be considered that the minimum time window must be at least larger than the maximum delay that may occur due to the finite traveling speed. For example, for a typical clinical PET size, the maximum traveling distance is 70 cm which corresponds to 2.3 ns of maximum time delay. The timing window that is used in PET scanners is typically between 4 and 20 ns.

5.2 Data acquisition system

A typical PET data acquisition system can be described as a two-branch structure. On one side, there is the timing circuitry that provides the coincidence information and enables the data acquisition of the involved detectors, while on the other side, position and energy signals are converted into digital values.

Figure 10 illustrates the PET data acquisition for a two-detector system. Along the timing branch, the PMT signal is preamplified with a fast amplifier (to preserve the time information) and fed into a discriminator that produces a digital signal when a γ-ray is detected. In order to improve the time resolution the discriminator could be a CFD (constant fraction discriminator), thus minimizing the uncertainty on the measure of the arrival time due to pulse height variations. The width of the digital signal generated by the CFD is set to be equal to the time window τ. The timing pulses are amplified and fed into a coincidence circuitry. In this simplified example, the coincidence circuitry can be a logic *AND* between the two logic signals that generate a coincidence signal when the two signals have a certain overlap. In this way, a coincidence is accepted

when the time difference in the γ-ray arrival is within $\pm\tau$. Hence, the effective time coincidence window is actually $2\ \tau$.

Along the other branch, signals from the PMTs (four in the case of a block detector) are digitized only if enabled by the coincidence signal. The extension of this concept to a multiple detector system can be obtained by implementing a more complex coincidence circuitry that is able to detect the pair of blocks where the coincidence occurred, thus providing a trigger signal to enable the data acquisition for the involved blocks only.

5.3 PET geometries

The core of a PET system is the set of detectors that are positioned around the object under study to detect pairs of annihilation γ-rays. The tomographic acquisition requires the collection of a full set of line integrals defined by the possible lines of response sampling the object along the spatial and angular coordinates. There are several detector arrangements that are able to properly sample the LORs. For example, similarly to SPECT, the detectors can rotate around the object. In this case, at least a pair of detectors positioned at opposite locations is necessary to perform the electronic collimation. This configuration may be convenient only when a limited number of detectors is available. A much more convenient detector arrangement is the *ring geometry*. This geometry allows many different LORs to be sampled simultaneously without any detector movement. Each detector can acquire data when in coincidence with any detector belonging to an opposite arc of detectors, thus defining a sort of wedge (Fig. 11). The intersection of all the similarly defined wedges is the field-of-view (FOV) of the PET system. More formally the FOV is the region of space that is sampled enough to provide a full set of LORs for the tomographic reconstruction. In a ring geometry, it is a circle centered on the scanner axis. Thus, a single-ring PET provides images of slices of the object with an axial extension equal to the detector size along the ring axis.

In order to increase the FOV size along the axial directions modern PET systems comprise more rings of detectors with a typical axial extension of 15–20 cm. As of today, all clinical PET systems feature a multi-ring geometry.

5.4 From 2D to 3D PET

Multi-ring PET systems are classified into two categories: 2D and 3D scanners. In 2D PET, coincidences among detectors belonging to two different rings are not allowed and thus a single ring records data coming from a single slice of object/patient. This simplification makes the image reconstruction process easier (see Sect. 6.6). In addition, in order to limit the number of single events reaching a single detector, each ring is physically separated from the adjacent one with a septum made of a high Z material. The 3D PET scanners are also able to record inter-ring coincidences (Fig. 12). Only with the advent of more advanced reconstruction algorithms and more powerful hardware resources the management of these 3D data has become possible [38]. Compared to the intrinsically 2D systems, the 3D modality is a big step forward in terms of system sensitivity with a maximum increase of about the number of rings. In

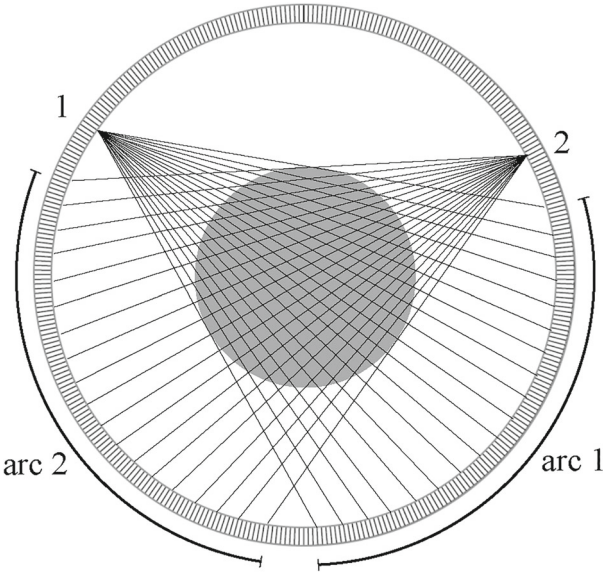

Fig. 11 Pictorial view of the detectors in coincidence with a single block, e.g, detector 1 (2) is in coincidence with all detectors in arc 1 (2). The subtended arc defines the borders of the field-of-view. The full FOV is given by the intersections of all arcs

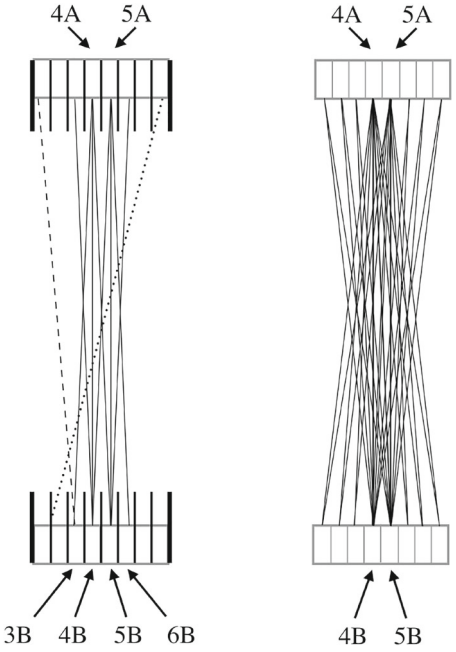

Fig. 12 Axial section of a 2D and 3D PET showing the limited angle acceptance for LORs inclined along the scanner axis in 2D PET. Left: 2D mode with septa. In this case, detectors of a ring are in coincidence with the same ring or lying in the neighboring rings, e.g., block 4A is in coincidence with 3B, 4B and 5B only. The picture only shows all the acceptable LORs involving detectors 4A, 5A, 4B and 5B. The LOR indicated by the dashed line is rejected by the 2D mode coincidence system, while the dotted LOR is blocked by the septum between blocks 2B and 3B. Right: 3D mode. All possible LORs are accepted. For example, block 4A is allowed to record coincidences with all rings. The picture shows all the acceptable LORs involving detectors 4A, 5A, 4B and 5B

practice, it is possible to limit the maximum distance among rings (usually called *ring difference*) for a coincidence to be acceptable. In spite of the quality of the 3D image reconstruction technique, the spatial resolution, especially along the axial direction, degrades as the ring difference increases. In the past, some PET systems were available with retractable septa in order to allow switching between 2D and 3D modalities, since the 2D mode has the capability to better reject scattered events, as well as being more insensitive to the activity outside the FOV. Such features were important in the past for some specific clinical cases but, as of today, novel technologies make it possible to have an intrinsically 3D PET system as the clinical standard.

5.5 Spatial resolution issues: technological aspects

The limitations in spatial resolution of PET due to the physics of the $\beta+$ have been already discussed in Sect. 3. The best achievable spatial resolution is also limited by other factors related to the detection process and the technology in use.

In general, the spatial resolution of a PET system is not constant along the whole FOV and the three-dimensional Point Spread Function (PSF) is not isotropic. This fact is related to the geometry of a PET system that does not sample all the lines of flight in the same way. Assuming a ring geometry, radial, tangential and axial directions are naturally defined and the FWHM of the PSF is normally not the same along the three directions. The degradation of the spatial resolution is essentially due to the uncertainty in the determination of the line-of-flight (LOF) that depends upon factors related either to the detector geometry or to the physics of the detection process. The following considerations are elaborated for a pixelated detector block as it is the most common configuration. When a coincidence is detected a pair of crystals defines the LOR. For the finite size of the detectors, the LOR is not actually a line but a region (sometimes called *tube of response* or TOR), where the annihilation has a non-zero probability to have occurred. This probability is described by a coincidence response function. For example, let us consider a pair of facing square crystals. The domain of the coincidence response function is a parallelepiped with bases defined by the crystals' faces. At equal distances from the two detectors and along the radial direction the coincidence response function is triangular in shape. From simple geometrical considerations, there is a higher probability for the γ-ray pair to have been generated at the center while the probability goes linearly to zero at the borders of the tube. In this mid-plane, the FWHM of the coincidence response function is then equal to half the size of the crystal (d) along the same direction. With similar considerations, one can understand that the FWHM of the coincidence response function worsens by moving closer to one of the two detectors as the function starts to be trapezoidal in shape. Thus, the contribution (in terms of FWHM) to the spatial resolution due to the finite crystal size is minimum at the center of the FOV and equal to $d/2$. When the crystals in a matrix are separated by a reflective material of non-negligible thickness, the value d is actually the crystal pitch, i.e., the crystal size plus the thickness of the separation material. The previous considerations are true only for facing detectors or, in general, for pairs of detectors with negligible thickness. In fact, as the crystals defining the LOR are not aligned, the finite thickness of the crystals comes into play enlarging the domain

of the response function. If there is no information on the depth of interaction (DOI) in the crystal, the coincidence response function is not negligible along the enlarged tube-of-response, thus introducing a further contribution to the FWHM on top of the $d/2$ term. This new term is usually indicated with the letter p and is called *parallax error*. In PET with ring geometry, the parallax error has a significant effect along the radial direction as the point spread function of the reconstructed image experiences a sort of radial elongation. The PSF worsens by moving far from the center of the FOV where the parallax error still has some effect only along the axial direction (and for 3D PET only).

The contribution to the FWHM of the PSF along the radial direction can be approximated by Eq. (15):

$$p = \alpha \frac{r}{\sqrt{r^2 + R^2}}, \tag{15}$$

where r is the radial position where the PSF is derived, R is the radius of the PET ring and α is a term that depends on the material and the thickness of the scintillating crystals. For example, α= 12.5 for a 30 mm thick BGO crystal [39]. The crystal pitch d and the parallax error p are both related to the geometry of the scintillator. Assuming that both crystal elements have been correctly identified as the region of space where the first interaction of the two γ-rays occurred they are the two only contributions to the spatial resolution. However, some errors may also occur in the identification of the crystal. When the crystal position is identified via *light sharing* technique, i.e., by calculating the centroid of the light spot emerging from the crystal, there is a non-negligible, position-dependent error. The source of this error is twofold: there could be a possible error in the *pixel identification* process (as discussed in Sect. 4.3) and there is the possibility of a multiple interaction in the scintillator. When the multiple interaction occurs in more than one crystal element the event is usually called an *inter-crystal scatter* or *ICS* event. As a consequence, more than one crystal produces a light spot. When using a photodetector that is able to provide the position of the centroid of the light spot only, the event may wrongly be assigned to a crystal element that is not the one where the first interaction occurred. The contributions of both *pixel identification* and *ICS* effects are included in the so-called *coding error* term that is usually indicated by the letter b. Taking into account both physical effects (described in Sect. 3) and the technological limitations here described, the best achievable spatial resolution in PET can be summarized with the following formula [28, 39]:

$$\text{FWHM} = 1.25\sqrt{(d/2)^2 + b^2 + (0.0022D)^2 + r^2 + p^2}, \tag{16}$$

where 1.25 is a term related to the further degradation of the PSF due to the non-uniform sampling of the LOR in the FOV and to the image reconstruction process. This value is estimated assuming an analytical reconstruction algorithm such as the *filtered back-projection* 6.6. The factors in the quadrature sum are due to the detector size (d), coding error (b), non-collinearity (where D is the scanner diameter), the positron range (r) and the parallax effect (p).

Various techniques have been introduced to reduce the effect of the technology-related spatial resolution degradation terms. For example, detectors able to estimate

the depth of interaction have been proposed, especially in the field of pre-clinical systems (see Sect. 8.2).

5.6 Noise in PET events

The FWHM estimation in the spatial resolution Eq. (16) is defined assuming infinite statistics, i.e., it does not include effects from noise. Noise characteristics have important implications for quantitation and detection performance in PET imaging, especially in high-resolution scanners.

Detection efficiency refers to the efficiency of a radiation measuring instrument that converts emissions from the radiation source into useful signals from the detector. A maximum detection efficiency is desirable to obtain maximum information (minimum statistical noise) with a minimum amount of activity, i.e., with a dose reduction.

The detection efficiency D of a radiation counting system can be defined as $D = R/A$ where R is the counting rate and A is the source activity. D is affected by several factors and can be written as a product of individual contributions: $D = g \times \varepsilon \times f \times F$, where g is the geometrical efficiency (solid angle coverage of the PET ring), ε is the intrinsic detection efficiency (obtained as the product of the 511 keV γ-rays intrinsic efficiencies of the two detectors involved in the coincidence), f is the electronic recording efficiency and F is a factor that takes into account the absorption and scattering in the object.

The geometrical efficiency g can be increased by reducing the scanner diameter and/or increasing the axial extension. However, the minimum scanner diameter is limited by patient size and by the parallax effect that worsens as the scanner radius is reduced. In turn, axial extension is limited by the cost of the building material (mainly the scintillating crystal) and by a higher scatter fraction (defined by Eq. (17)) for long-axial extension systems. On the other hand, ε can be increased by using thicker scintillating crystals, but, once again, the spatial resolution would be degraded by the increased parallax effect. In addition to statistical noise from the counting rate limitations of a PET system, various sources of noise, like the spatial resolution limitations, arise from both the physics of γ-ray interaction with matter and the adopted technology. The term *noise* in PET is often inappropriately used to describe the fluctuations in space in the measurement of a uniform activity (*uniformity measurement*). A more appropriate definition is the *image roughness* that is usually given in terms of the standard deviation of the measured value.

Apart from the already discussed statistical limitations, uniformity is also limited by the presence of LOR not appropriately recorded. A recorded LOR is meaningful only when is generated by a true count. A *true* count is a coincidence event where the γ-ray pair is generated by a single annihilation event and both γ-rays are detected without experiencing any other interaction along their path. In fact, only under these conditions, the LOR passes by (or more correctly, the tube-of-response contains) the annihilation point.

Actually, not all the LORs generated by the coincidence detection pass through (with all limitations discussed in Sects. 3 and 5.5) the annihilation point. Hence, not all the LORs generated by a coincidence detection of two γ-rays give *true* counts. Figure 13

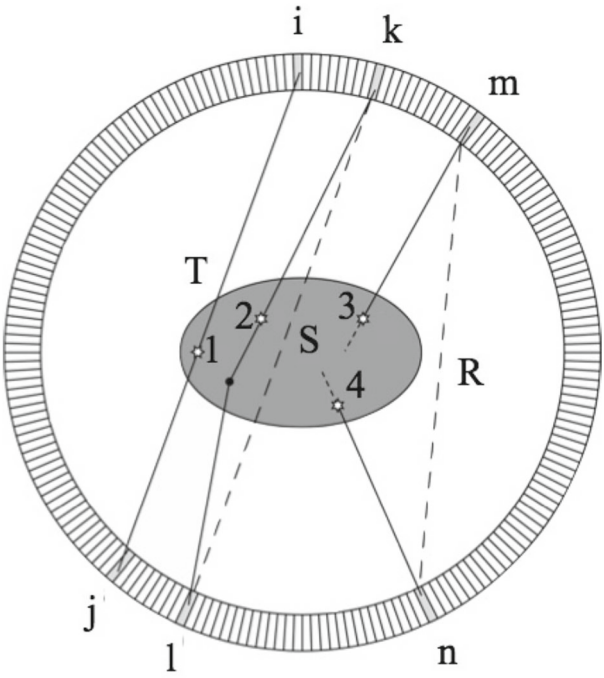

Fig. 13 Pictorial example of *true* (T), *scattered* (S) and *random* (R) counts (see text)

shows three possible types of events that can be recorded by a PET as a coincidence. The annihilation occurring in location 1 corresponds to a *true* count (usually indicated by the letter T) between detectors i and j. In the event originating from position 2, at least one of the two γ-rays experiences a scattering along its path. The LOR generated in this way, recorded by detectors k and l, does not pass through the annihilation point. Such type of event is called *scattered* (S) count. γ-ray emissions from points 3 and 4 occur simultaneously. The two γ-rays, although detected in time coincidence by m and n detectors are not generated by the same annihilation. They are accidentally detected in coincidence and this type of event is usually called accidental or *random* (R) events. Also in this case the generated LOR is not correlated to any annihilation point. The sum of T, S and R events are called *prompt* (P) counts, where only *true* counts contain useful information for the image reconstruction. Another possible type of event is the so-called *multiple* count where more than two single events are recorded within the same coincidence time window. This event generates an ambiguity in deciding which is the γ-ray pair actually generated in a single annihilation, and thus this type of multiple event must be discarded. Note that the definition of *true*, *random*, *scattered* and *multiple* counts assumes perfect detectors.

The measured *true* (R_T) and *scattered* (R_S)count rates vary linearly with the activity present in the FOV (for a given activity distribution). On the other hand, the ratio between T and S can be usually considered constant. An important figure indicating the relative weight of the effect of *scattered* events on the reconstructed image is the *scatter fraction* (SF), which is defined as

$$\mathrm{SF} = \frac{R_\mathrm{S}}{(R_\mathrm{T} + R_\mathrm{S})}. \tag{17}$$

Scattered counts generate a low spatial frequency background that reduces the contrast in the reconstructed image. The spatial distribution of the intensity of the background generated by *scattered* counts depends on the activity distribution and the shape and size of the patient. However, a significant fraction of *scattered* counts can be discarded. In the first instance, a *scattered* event can be intrinsically discarded because the pair of hit detectors are not geometrically in coincidence. This happens when a large scattering angle occurs. Once a *prompt* event is acquired it is still possible to exclude a fraction of the *scattered* events using the energy information. In addition to the angular deviation, the Compton scattering also entails a loss of energy for the γ-ray. For a given γ-ray with energy E_γ, the relation between the scattering angle θ and the residual energy E'_γ is given by

$$E'_\gamma(\theta) = \frac{E_\gamma}{1 + \left(\frac{E_\gamma}{m_e c^2}\right)(1 - \cos\theta)}, \tag{18}$$

where m_e is the mass of the electron at rest. According to Eq. (18) the scattered photon has as energy $1/3 \times 511\mathrm{keV} < E'_\gamma < 511$ keV. Figure 14 (left), shows the behavior of the residual energy E'_γ versus the scattering angle θ. Thus, by measuring the energy of the incoming γ-ray, those that have been scattered can be recognized as being $E < 511$ keV. It is important to note that the angular distribution of the scattered photons at 511 keV is peaked in the forward direction (small θ values), i.e., residual energies close to 511 keV are more probable than the others. In fact, the differential cross-section $\mathrm{d}\sigma/\mathrm{d}\Omega$ for the Compton scattering is given by the *Klein–Nishina formula*, expressed in $[\mathrm{cm}^2\mathrm{sr}^{-1}\mathrm{electron}^{-1}]$:

$$\frac{\mathrm{d}\sigma_c}{\mathrm{d}\Omega}(\theta) = r_e^2 \frac{1 + \cos^2\theta}{2} \frac{1}{[1 + E_\gamma^2(1 - \cos\theta)]^2} \left\{1 + \frac{E_\gamma(1 - \cos\theta)^2}{(1 + \cos^2\theta)[1 + E_\gamma(1 - \cos\theta)]}\right\}, \tag{19}$$

where $\mathrm{d}\Omega$ is an infinitesimal solid angle element, E_γ is the energy of the photon, r_e is the classical electron radius.

The relationship between the scattering angle and the differential cross-section $(\mathrm{d}\sigma_c/\mathrm{d}\Omega)_N$, normalized to the maximum value, for a 511 keV γ-ray is reported in Fig. 14 (right). In this case, 50% of all Compton interactions are characterized by a scattering angle of 60° or less. Using Eqs. (18) and (19), it is possible to establish a relationship between E'_γ and $(\mathrm{d}\sigma_c/\mathrm{d}\Omega)_N$ that is actually the energy spectrum of an object-scattered γ-ray (Fig. 15).

The ability of the detector to determine the energy of the photon is known as the energy resolution. Typical values for the energy resolution of LSO read out by PMTs is 15–20% at 511 keV. Due to the finite value of the detector energy resolution, it is not possible to set a fine energy threshold at 511 keV but a wider energy window EW can be set. Increasing the width of the EW increases the fraction of scattered counts (larger SF) and the accepted scattered counts may be subjected to larger and larger

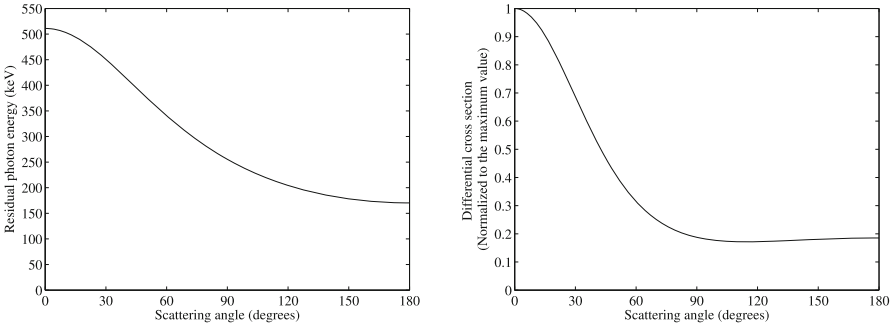

Fig. 14 Left: plot of the energy of the Compton scattered photon (E'_γ) as a function of the scattering angle θ. Right: the relationship between the scattering angle and the differential cross-section $(\mathrm{d}\sigma_c/\mathrm{d}\Omega)_N$, normalized to the maximum value. Both plots are calculated for a 511 keV incident γ-ray

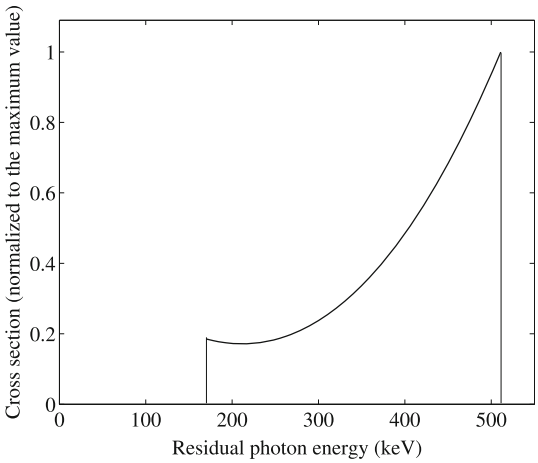

Fig. 15 Energy spectrum of a 511 keV γ-ray after a single Compton scattering in an object normalized to the maximum value. Energy values range between 173.3 keV (i.e., 511/3 keV) and 511 keV

scattering angles. The higher the energy resolution, the narrower the energy window can be set and a smaller fraction of scattered events is included. This energy selection is critical especially for the large number of scattered photons with an energy close to 511 keV, as shown in Fig. 15. Typical scatter fraction values in PET may range from 15–20% up to 50% in obese patients.

It must also be noted that what a PET detector measures is not the γ-ray energy but the energy of the photoelectron plus fluorescence photon (photoelectric interaction), recoil electrons (Compton interaction) or the sum when multiple interactions in the detector occur. Since the energy of the incoming γ-ray is a piece of critical information only full-energy interactions are acceptable. On the other hand, single interactions are preferred for the better spatial information provided. Hence, only photoelectric interactions in the detector are adequate to provide useful information for image reconstruction. For this reason, a scintillator with a high photofraction (at 511 keV) is required for PET (LSO has a photofraction of 32%).

As already discussed, when setting an energy window around the full-energy peak (typically 450–650 keV in clinical PET) a fraction of scatter events is still included.

For this reason, a number of methods to correct the effect of the *scattered* events in the degradation of image quality have been developed and are applied before or during the reconstruction process. They are usually classified with the term *scatter* correction and used to restore the object contrast in the final image (see Sect. 6.3).

While *scattered* events typically generate a structured background, *random* events generate a more uniform background. Nevertheless, their importance becomes significant as the activity, and then the single count rate, increases. In fact, to obtain quantitative data in PET it is necessary to estimate the rate of random coincidences in the measured data in each LOR. The *random* count rate can be expressed as [40]

$$R_{ij} = C_i \times C_j \times 2\tau, \tag{20}$$

where C_i and C_j are the singles count rate on detector i and j and τ is the coincidence time window. Hence, R_{ij} is proportional to the square of the activity in the field-of-view.

A narrow time window is then necessary to reduce *random* counts.

The noise equivalent count rate (NECR) is the figure of merit that quantifies the amount of background and statistical noise characteristic of a given PET scanner, thus evaluating the effect of the presence of *scattered* and *random* counts.

The formulation of NECR is as follows:

$$R_{\mathrm{NEC}} = \frac{R_{\mathrm{T}}^2}{R_{\mathrm{TOT}}}, \tag{21}$$

where R_{TOT} is the sum of *true* (R_{T}), *random* (R_{R}) and *scatter* (R_{S}) count rates:

$$R_{\mathrm{TOT}} = R_{\mathrm{T}} + R_{\mathrm{S}} + kR_{\mathrm{R}}, \tag{22}$$

and where k is a factor that takes into account the method used for estimating random counts, usually $k > 1$, while $k = 1$ for noiseless random counts.

Figure 16 shows an example of True, Scatter, Random and NECR curves as a function of the activity concentration.

As described above, the capability of a PET system to reject *scattered* and *random* counts is related to the energy and timing resolution of the detector, respectively. Both features can be improved with a careful selection of the scintillator characteristics. In particular, a high light yield, increasing both timing and energy resolution, is required. In addition, the time characteristics of the scintillation pulse (scintillation decay time) are also critical for time resolution. Although LSO:Ce and LYSO:Ce are well-established solutions for PET, research in this field is still an active topic especially for time-of-flight applications (see Sect. 7.5).

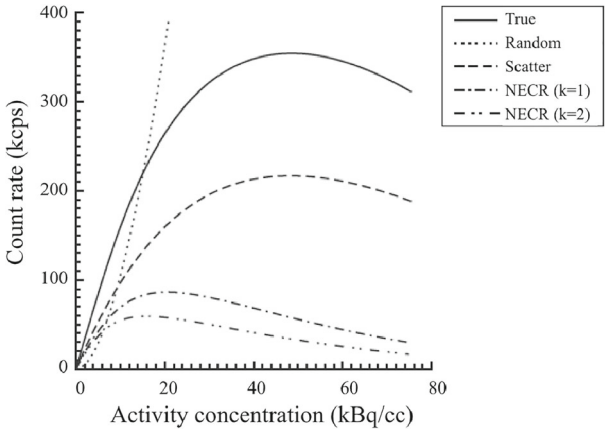

Fig. 16 Example of True, Scatter, Random and NECR curves as a function of the activity concentration obtained following NEMA NU 2 (2001) procedure. NECR data are reported for both extreme cases of $k = 1$ and $k = 2$. Data are taken with the GE Discovery SRX PET/CT system . (Data courtesy of IFC-CNR Pisa, Italy)

6 Software

6.1 Data representation: the sinogram

Raw data in PET are usually stored in *list mode format* where each entry of the list contains the coordinates of the LOR, i.e., by the physical coordinates of the two pixels that have been hit, energy, time and any other information that may be appropriate. This type of data representation is not convenient either for storage (it can easily reach tens of GB in file size) or for image reconstruction; hence, some pre-processing and reformatting are necessary.

First, it should be considered that events are recorded at different times. As time passes the radioisotope activity decreases. A *decay correction* is then necessary to ensure that the measurement of the activity density $\rho(x, y, z)$ is relative to a precise time point (typically the beginning of the acquisition or the time of the injection). An event n collected at a certain time point t_n should then be corrected by a (multiplicative) decay correction factor C_{decay}:

$$C_{\text{decay}} = e^{\frac{t_n - t_0}{\tau}}, \tag{23}$$

where t_0 is the time the reconstructed image is referred to and τ is the decay constant of the radioisotope in use.

In addition, the decay of the radioisotope has also to be considered when *dead time correction* is performed. Any acquisition system is affected by dead time. When the count rate remains constant the dead time correction factor is a constant multiplicative factor. However, as the count rate, in our case, is varying, dead time correction must be performed on an event-by-event basis.

After both decay and dead time corrections have been performed, events can be stored in *histogram mode data format*. In this case, data are stored indicating the corrected count rate recorded in each line-of-response LOR_{ij}. Ideally, the LOR_{ij} values are now proportional to the line integrals along the LOR itself. For example, histogram data can be stored in a 2D matrix, where each element (i, j) of the matrix contains the count rate recorded by a particular pair of detectors. However, for image reconstruction purposes there is a more convenient way to store line integrals. This representation is called *sinogram*. In the simplification of a 2D scanner with one ring only, the coordinates of the matrix are given by two physical coordinates of the LOR, namely s and ϕ: s represents the geometrical distance of the LOR from the scanner axis and ϕ is the angle of inclination of the LOR. The name sinogram is due to the fact that the sinogram representation of a point source with polar coordinates r, θ in the field-of-view is a sinusoidal function with amplitude r and phase θ. This representation is pretty natural in-ring geometries, even if some rebinning is necessary to transform the LOR index to (s, ϕ) coordinates. The information loss during rebinning is largely compensated by the mathematical convenience of the sinogram representation, particularly when employing analytic image reconstruction algorithms (see Sect. 6.6).

6.2 From 2D to 3D data acquisition modes

The sinogram representation can be easily extended to multi-ring 2D PET where data from each plane are stored in a separate sinogram. The plane id can be seen then as the third coordinate of a sinogram 3D matrix. With the advent of 3D PET, the problem of representing LOR with a non-zero axial inclination, i.e., involving detectors belonging to different rings, has to be considered. For example, the id of the ring can be replaced by the id's of the two rings involved, thus making the sinogram a 4-D matrix. The problem of image reconstruction of 3D sinograms is much more complicated than 2D sinograms. For that reason, numerous algorithms for rebinning 3D sinograms to 2D sinograms have been introduced. The simplest one is the so-called single slice rebinning or SSRB where oblique sinograms are assigned to the mid-plane between the two rings involved. In this way, in a PET with n rings $2n - 1$ 2D sinograms are generated. The consequence of the SSRB rebinning is a severe degradation of the axial spatial resolution especially at the radial edges of the FOV. For this reason, the SSRB is usually applied to a limited number of oblique sinograms. Only those relative to rings that are not too axially far away are considered, i.e., there is a maximum difference in ring id that is acceptable (called *ring difference*). There are also other techniques for rebinning 3D sinograms into 2D sinograms. One of the most popular is the Fourier Rebinning or FORE that aims at the reduction of axial spatial resolution degradation [41]. In recent years, with the increase of the available computational resources, intrinsically 3D reconstruction algorithms became accessible in such a way that 2D sinogram rebinning is not necessary anymore and the full potential of 3D PET can be unleashed.

6.3 Normalization and scatter correction

The efficiency of each LOR, i.e., the probability of a certain coincidence count emitted from a point (x, y, z) in the FOV to be detected in a LOR_{ij} mainly depends on geometrical and physical factors plus the contribution of the data acquisition system. The line integral model assumes a uniform behavior in the efficiency of the various LORs. However, non-uniformity of individual detectors due to the uncertainties, e.g., in crystal size, geometry and light yield and in detector electronics behavior (as, for example, detector thresholds), may introduce inter-LOR efficiency variation with respect to the ideal value. Data *normalization* in PET is the process for compensating these non-uniformities through a multiplication factor for each LOR. Normalization values are experimentally derived from the scan of a geometrically uniform object, such as a uniform cylinder. The main challenge of this procedure is to collect enough counts per each LOR so as to obtain low noise normalization factors. The necessity of using relatively low activity density in the normalization phantom to limit both excessive dead time data loss and high random event count rate makes a normalization scan quite long to be performed. Furthermore, the relatively fast decay of ^{18}F, when used, limits the number of counts that can be collected. For that reason, rotating rod sources of ^{68}Ge, mimicking an annular source, have been used instead.

Data normalization is usually applied at the level of the sinogram, i.e., a normalization sinogram is generated from the LOR normalization values. In this case, the data normalization results in a multiplication of sinograms. Due to the relatively low statistics of normalization data, component-based variance reduction methods are implemented in order to reduce noise in the final image [6].

In Sect. 5.6, the use of an energy window has been described as a way to reduce the scatter fraction on PET data. As already discussed a very tight energy window around 511 keV cannot be used. Although it would be optimal for the rejection of scattered events, this approach would be also accompanied by a severe reduction in sensitivity for a large number of rejected true counts. After geometrical and energy discrimination, the residual scatter events present in PET data are indistinguishable from true counts. The spatial contribution of scatter counts along the FOV has a fairly low spatial frequency distribution. However, it is not totally flat but results in a "spatially structured" image. This is mainly due to the forward-peaked *Klein–Nishina formula* (Eq. (19)) at 511 keV. To minimize the effect of scatter counts in the reconstructed image that would limit image contrast and the accuracy of quantification, a procedure called *scatter correction* must be performed. It is particularly important in 3D PET, being the 2D mode using septa (now obsolete) relatively insensitive to scatter counts.

The *scatter correction* consists in estimating the number of *scatter* counts contributing to a given LOR_{ij} as a result of a Compton interaction. It is important to notice that many different Line-of-flights (all LOFs that are geometrically compatible) may generate a scatter count assigned to LOR_{ij}. In addition, the original LOF may either (i) correspond to an acceptable LOR (the emission point is within the FOV) or (ii) may be generated from the activity outside the FOV. The previous consideration is made under the assumption that only one Compton scattering occurs to only one of the two coincidence γ-rays along their travel. This assumption, called *single scattering*

approximation is particularly relevant for scatter correction as it is the simplest and easily modellable situation. In case (i) the Compton scattering acts as an attenuation process (see Sect. 6.5), being the count removed from its original LOR. Thus, it results evident how scatter and attenuation are strictly correlated being the result of the same phenomenon. Hence, it is important to understand the order of performing *scatter correction* and *attenuation correction*. *Scatter correction* should be performed first as it removes unwanted events from a LOR. After that, the *attenuation correction* restores the proper number of counts N_{ij} collected along a LOR_{ij}.

Methods for *scatter correction* can be classified according to the way the scatter count distributions are estimated. These include analytical methods [42, 43], Monte Carlo simulation techniques [44], multiple (e.g., dual [45] or triple [46]) energy window methods and model-based scatter correction algorithms [47, 48]. Analytical methods consist of fitting with a Gaussian profile the tails of the object as they appear at the edge of each projection, e.g., in the sinogram. This method assumes a uniform behavior of the scatter component along the FOV. In practice, the Gaussian fitting is applicable when the scattering object is nearly uniform and has a regular shape, e.g., a cylinder or a sphere. For example, it was demonstrated to work well in brain studies [49], but not in whole-body scanning where the object is more irregular and occupies most of the FOV (the tails are shorter and can be hardly fitted). Monte Carlo-based scatter correction utilizes the 3D reconstructed image volume (non-scatter corrected) as the source intensity distribution for a photon-tracking Monte Carlo simulation [44]. This method has the potential to be rather accurate but it is time-consuming due to the necessity to perform the Monte Carlo simulation after a first image reconstruction. Methods for scatter correction using dual-energy window work under the assumption that PET data selected using the standard energy window (e.g., 380–850 keV, as in [45]) are a combination of a *true counts* data set plus a *scatter counts* data set, while data in a lower energy window (e.g., 200–380 keV) are assumed to contain scatter data only. The scatter contribution in the upper energy window data is assumed to be a fraction of the scatter data obtained from the lower energy window. Hence, the idea is to estimate the scatter contribution from the lower energy window data and then to subtract this contribution after having multiplied it for a proper scaling factor. The scaling parameter can be derived from measurements on dedicated phantoms, e.g., from the ratios of counts from line sources due to scattered and unscattered events in the two energy windows in head-sized phantoms [45]. In the model-based scatter correction algorithm the estimation of the scatter contribution is calculated by combining the information from emission data with the image obtained from the transmission scan. Thus, the number of scatter events contributing to a LOR_{ij} is calculated using the Klein–Nishina formula (19) together with a model of the detection system. The non-scatter corrected image is assumed as the "source" and the transmission image as the "scattering" object. In general, all these methods perform well when all the activity is within the FOV. When scatter events are generated from out-FOV activity, these methods are less accurate but still sufficient to significantly improve image signal-to-noise ratio and quantification capability.

6.4 Random correction

Apart from limiting the occurrence of *random* counts as described in Sect. 5.6, methods for their correction in the reconstructed image are also available. This process is called *random correction*. It is based on a statistical estimation of the *random* counts distribution that may be either subtracted from *prompt events* online or stored as a separate histogram (with an entry for each LOR) for later processing. The estimation of the *random* count rate can be indirect or direct. In the first case, the formula (20) is used to derive R_{ij} from the *single* count rate recorded in each detector. This method is in principle precise but may be not very accurate for the systematic error due to the a-priori estimation of τ. To directly derive the *random* count rate, the so-called *delayed window technique* [19] can be used instead. In this case, an additional coincidence processor is used. The logic pulse from one detector is delayed in such a way that it has no more correlation with the other photon of the annihilation pair. When a coincidence between a delayed pulse from detector i and a prompt pulse from detector j is detected $R_{\text{delayed},ij}$ is increased by one. At the end of the acquisition, $R_{\text{delayed},ij}$ can be considered a good estimation of R_{ij}. The advantage is a more accurate estimation of the random counts even if it is characterized by a noisier distribution.

6.5 Attenuation correction

At 511 keV, the attenuation coefficient μ in soft tissues is about 0.096 cm^{-1} while in bone is about 0.17 cm^{-1}. Hence, there is a relatively high probability for a γ-ray to interact in patient tissues before reaching the surrounding PET detectors, mainly via Compton scattering or photoelectric absorption. *Scattered* counts are events that adversely affect the image quality (as seen in Sect. 5.6), by assigning a count to a wrong LOR. When a photoelectric interaction occurs along an acceptable LOF, i.e., corresponding to an LOR, the count is simply removed from that LOR. As discussed in Sect. 6.3 this may also happen as a consequence of a Compton scattering (or for multiple interactions) in the object. Formally, the line integral introduced in Sect. 3.1 should be modified as follows as a consequence of the γ-ray attenuation along a LOR_{ij}:

$$N_{ij} = k \int_{\text{LOR}_{ij}} \rho(x, y, z) \mathrm{d}L \cdot P_i \cdot P_j, \tag{24}$$

where N_{ij} is the number of counts recorded along LOR_{ij} and

$$P_i = e^{-\int_{L_i} \mu(x)\mathrm{d}x}; \quad P_j = e^{-\int_{L_j} \mu(x)\mathrm{d}x}, \tag{25}$$

are the probabilities for the two γ-rays to reach detectors i and j, respectively and L_i and L_j are the lines connecting the annihilation point to detectors i and j. Thus, the probability P for both γ-rays to reach the corresponding detectors, and then contributing to LOR_{ij}, is

$$P = P_i \cdot P_j = e^{-\int_{L_i} \mu(x)\mathrm{d}x} \cdot e^{-\int_{L_j} \mu(x)\mathrm{d}x} = e^{-\int_{L_i+L_j} \mu(x)\mathrm{d}x}. \tag{26}$$

N_{ij} can then be written as

$$N_{ij} = k \int_{\mathrm{LOR}_{ij}} \rho(x, y, z) \mathrm{d}L \cdot e^{-\int_L \mu(x)}, \tag{27}$$

where $L = L_1 + L_2$. It must be noted here that the probability for a count to be detected does not depend on the position of the annihilation point along the LOR but only on the line integral of the attenuation coefficient along the LOR itself. The quantity

$$\frac{1}{P} = e^{\int_L \mu(x)}, \tag{28}$$

is usually called attenuation correction factor (ACF)

To have an idea of the relative weight of the ACF it must be noted that $\mu_{\mathrm{softtissue}} = 0.096\mathrm{cm}^{-1}$ and then with a 40 cm diameter patient the ACF is about 50.

The effect of attenuation on the image is twofold: (i) counts are underestimated, thus highly affecting quantification; (ii) image artifacts may also occur especially when strong non-uniformities of tissues are present, such as in the human body with bone and soft tissue. However, even in the case of a uniform cylinder, the reconstructed image would show significant attenuation artifacts in the form of an underestimation of activity density at the center of the object with respect to the edges. In fact, lines crossing the center of the object are more attenuated than lines crossing the borders tangentially, thus generating a typical *cupping* artifact that is clearly visible along image profiles.

Similar to *scatter* correction, *attenuation* correction is a necessary step in image reconstruction for PET and can be performed using Eq. (28) above. There are several ways to derive the ACFs for each LOR. The most common approach consists of a direct or indirect estimation of the ACF through the measurement of the distribution of the attenuation coefficients $\mu(x, y, z)$ at 511 keV. A typical way to directly measure $\mu(x, y, z)$ is the use of the so-called transmission scan [50] that can be applied with coincident 511 keV photons (for example, from the 273 days half-life ^{68}Ge radioisotope). The method consists in measuring the attenuation of a γ-ray beam along a certain LOR in the presence of the object. The attenuation is measured by comparing the counts recorded along a certain line in the presence of the object (transmission scan) to those obtained without the object (blank scan). Attenuation data along all the LORs are collected, for example, by rotating the source around the object, thus creating a sort of transmission scan and blank scan sinograms. The LOR is thus defined by the coincidence between the near side and the opposite side detectors. Thanks to the coincidence collimation of the beam a linear source (rod) can be used. The ratio between the two sinograms gives the attenuation correction sinograms containing the ACFs to be used as a multiplication factor for the emission sinogram. The advantage of this approach stays in its relatively low technological complexity and in the accuracy of the results. However, there are several constraints: long scan times, noisy attenuation sinograms due to low statistics, need for replacement of the transmission source every 12 or 18 months. In addition, since a post-injection transmission scan is more desirable in clinical settings because it increases patient comfort and scan-

ner throughput, the transmission scan acquired after the injection of the PET tracer would suffer from contamination by 511 keV photons emitted from the PET tracer. To overcome the latter limitation, single 662 keV photons from the long half-life (30.17 years) ^{137}Cs can be used instead. However, the measurement is less accurate due to the difference between attenuation coefficients at 511 keV and 662 keV and a point source must be used for the lack of electronic collimation with the consequence of a further increase in transmission scan time. Before the advent of PET/CT systems (see Sect. 7.4), almost all clinical PET systems featured some sort of transmission scan technique based on radioactive sources to perform attenuation correction.

6.6 Image reconstruction in PET

After the sinogram with all the necessary corrections is generated, the number of counts in each bin is proportional to the line integral of the activity distribution along the line L defined by (s, ϕ) coordinates. A sinogram is usually represented with the s coordinate along the abscissa and ϕ along the ordinate. Each row, corresponding to a certain angle is called *projection*, described by $p(s, \phi)$. The mathematical process of transforming the object into its projections to form a sinogram is called *Radon transform* [1]. In general, the problem of image reconstruction (here explained for the 2D case only) is to recover the activity distribution $\rho(x, y)$ from projections $p(s, \phi)$, i.e., it is sufficient to find the inverse operation of the Radon transform to be able to obtain a tomographic image. Various methods have been developed for this purpose both relying on analytical or iterative algorithms.

A full description of the mathematics behind and of the implementation of the various methods is beyond the scope of the present paper. However, two of them are briefly described for completeness. A comprehensive description of methods for image reconstruction in PET can be found in [51, 52].

The simplest method is an analytical algorithm called Filtered Back-Projection, in brief FBP, introduced in the field of medical imaging by Shepp and Logan [53]. FBP is easy to be implemented and it is usually fast, but is characterized by image noise amplification especially when applied in low statistic acquisitions. It is the most commonly used algorithm for 2D reconstruction. A derivation of the 2D activity distribution $\rho(x, y)$ can be obtained with a process called *Back-Projection*. The value of each projection $p(s, \phi)$ is added to all image elements crossed by the line defined by the coordinates (s, ϕ). For the different coordinate systems in use for the image and the *projection* operator, a weighting factor is applied to account for the path length of the line through the pixel. The result of the back-projections process is an image $I(x, y)$ affected by a strong blurring. It can be demonstrated that, for an infinite number of angular projections and an infinite spatial sampling, the back-projection image is equivalent to the original image $\rho(x, y)$ convolved with a $1/r$ function, i.e.,

$$I(r, \theta) = \rho(r, \theta) \otimes \left| \frac{1}{r} \right|, \tag{29}$$

where polar coordinates are now used for simplicity. Both members of Eq. (29) can be Fourier transformed and by applying the convolution theorem for Fourier transform Eq. (29) can be written as

$$F(I(r,\theta)) = F\left(\rho(r,\theta)) \times F\left(\left|\frac{1}{r}\right|\right)\right), \tag{30}$$

and then, considering that $F(|1/r|) = |1/\nu|$:

$$\rho(r,\theta) = F^{-1}(F(I(r,\theta) \times |\nu|). \tag{31}$$

Equation (31) implies that $\rho(x, y)$ can be obtained by back-projecting the filtered projections. This explains the name *Filtered Back-Projection*. The frequency filter $|\nu|$ is called *ramp filter* or *Ram-Lak filter*.

In summary, the sequence of operations that have to be performed to reconstruct the image is

1. Unidimensional Fourier transform of each projection
2. Filtering each projection in the unidimensional Fourier space by multiplying by the function $|\nu|$
3. Inverse unidimensional Fourier transform of each filtered projection
4. Projecting backwards the filtered projections

The considerations above are not exact in the case of limited angular and spatial sampling. When angular sampling is not infinite, the image is affected by a typical *star artifact* since, during back-projection, counts are accumulated preferably along the angles of projection. On the other hand, the limited spatial sampling requires a *cutoff* frequency to be applied to $|\nu|$. For Shannon's sampling theorem, this frequency is equal to the Nyquist frequency $1/(2d)$, where d is the sampling step. However, the use of the ramp filter still amplifies high-frequency components during the back-projection step and in particular the high frequencies caused by statistical limitations of the projections. To reduce the noise the filtering is further modified. The most common filters are the Hamming and the Shepp–Logan filters which both result in a smoother image. FBP is a linear operator and, apart from noise problems, it is considered excellent for quantitative imaging. However, when looking at an image in detail, there could be regions where values are underestimated or even negative. This effect is related to the $|\nu|$ filtering that in the space domain is equivalent to a convolution with the sinc function. This can cause undershoot fluctuations in the image in regions where the source distribution has high gradients that are represented by high values in the frequency domain. For this reason, together with the difficulties in including the physics of the detection process within analytical image reconstruction, other solutions based on iterative algorithms have been proposed.

6.7 Iterative and PSF-based reconstruction

Iterative algorithms offer an alternative approach to the analytic techniques, improving the image quality by the use of a realistic model of the imaging system. This model is

represented by a probability matrix, called *System Matrix* (P) which correlates positron emission and coincidence γ-ray detection. Several physical parameters which describe the imaging process, such as system geometries, detector properties, photon emission and interactions, positron range and 2γ's non-collinearity can be included. Moreover, iterative algorithms have the potential to account for the stochastic nature of the PET events, making it possible to reduce noise in the reconstructed image. The cost of this improvement is a higher computational complexity. However, recent advances in computing resources and novel reconstruction algorithms allow the use of iterative methods in clinical practice. The Maximum Likelihood Expectation Maximization or ML-EM algorithm is one of the most widely used reconstruction algorithms for PET and represents the foundation for many other algorithms. It was introduced by Shepp and Vardi [54]. As for the FBP, the first implicit step of the algorithm is the discretization of the image domain: the FOV is usually subdivided into N volume elements (voxels). Once again the problem is to derive from the LOR counts n_i the value of the activity distribution in every single voxel (λ_j) defined by

$$\lambda_j = \int_{\text{voxel}\, j} \rho(x, y, z) \cdot \mathrm{d}x \cdot \mathrm{d}y \cdot \mathrm{d}z. \tag{32}$$

Note that the number of counts in each LOR was previously indicated as N_{ij} as the LOR was defined by the two detectors. Now it is expressed simply as n_i with just one index indicating the LOR. The idea behind the ML-EM algorithm is to find the activity values λ_j which maximize the probability of the measured values (n_i); this probability is represented by a likelihood function. In order to compute this function we need the *System Matrix P* that can be calculated totally, or in part, either analytically or via Monte Carlo simulations and with different levels of approximation. The size of the *System Matrix* is one of the most demanding issues for ML-EM as it can easily exceed hundreds of Gigabytes especially when physical components are included. Symmetries and the sparsity of P are useful features to compress the *System Matrix*, but the computation and compression of P remain yet a challenging step in iterative reconstruction.

The single element of P, p_{ij}, is defined as the probability that a γ-ray pair emitted from voxel j with ($j = 1; 2; 3; :::N$) is detected in the LOR i with ($i = 1; 2; 3; :::M$). It can be demonstrated that an iterative relation approaching the value of maximum likelihood is given by

$$\lambda_j^{\text{new}} = \frac{\lambda_j^{\text{old}}}{\sum_{i=1}^{M} p_{ji}} \sum_{i=1}^{M} \frac{n_i\, p_{ij}}{\sum_{j=1}^{N} \lambda_j^{\text{old}}\, p_{ij}} \tag{33}$$

The initial distribution λ_j^0 is usually chosen as uniform and non-negative. This iteration procedure is stopped when the reconstructed image is the best trade-off between spatial resolution and noise, i.e., the stopping point is determined empirically. In summary, the ML-EM algorithm can be seen as the iteration of four circular steps (Fig. 17) in the image and the data domains:

1. Forward-project image values into data domain

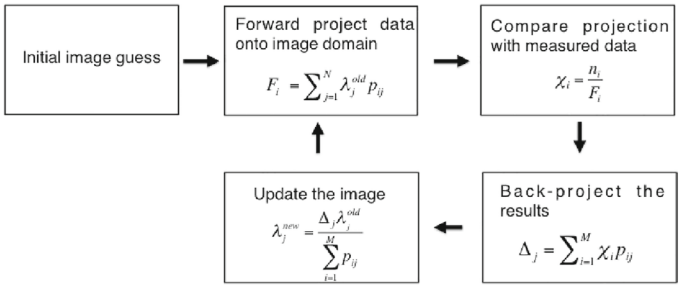

Fig. 17 Representation of the four steps in a single ML-EM iteration

2. Compare projection with measured data
3. Back-project the ratio between measured data and projected data for all LORs
4. Update image weighted by p_j

The ML-EM algorithm is intrinsically LOR-based. Despite this, sinogram-based implementations are typically used in clinical practice to reduce the computational cost of the algorithm. Even with the advent of modern computers the iterative approach to image reconstruction still remains a computationally intensive job. The introduction of increasingly more sophisticated algorithms and the use of realistic system matrix models have been slowed down by the increasing complexity of PET systems. In fact, it has been observed over the last two decades that the number of lines of response in PET scanners has grown at a rate that outpaces Moore's Law, which describes the increase of the packing density of transistors onto a microchip. Processing algorithms must carefully be optimized in order to be able to run very fast. The speeding up of iterative algorithms is an active line of research, especially after the introduction of techniques able to exploit the potential of Graphical Processing Units (GPUs) in heavy load computational tasks such as image reconstruction [55].

An example of a successful speeding-up method is the Ordered Subsets Expectation Maximization algorithm or OS-EM [56]. The idea behind OS-EM for reducing the computational load is to divide the task to be performed into more simple groups of operations. OS-EM is nothing else that a ML-EM algorithm where the set of projections is divided into M equipollent subsets. Many different criteria for filling these subsets, which are usually disjoint, have been proposed. The most used approach is to subdivide data into equally angularly spaced projections. A certain ML-EM iteration i to be performed on the entire dataset is subdivided into M sub-iterations in which the value of $\lambda_j^{i,m}$ is computed using only the data in one subset m and then it is updated to $\lambda_j^{i,m+1}$ using the data in the subset $m+1$. Once the subsets have been all considered a new iteration is applied to the first subset and so on. The power of this method stays in the fact that a complete iteration $k \rightarrow k+1$ of OS-EM is equivalent to M effective iterations of ML-EM, while the time required for each sub-iteration is approximately $1/M$ of the ML-EM iteration because of the reduced number of terms on the summation. This makes the convergence in OS-EM M times faster than ML-EM. On the other hand, it must be considered that increasing the number of subsets, the robustness of the method, and so the quality of the final image, is degraded due to the fact that the

image may be compared with insufficient data. Although OS-EM provides a significant speed upgrade for iterative reconstruction, the incorporation of a realistic image model still remains challenging. In principle, the physics of the detection process should be included in the term p_{ij} together with geometrical effects. However, this usually makes the *System Matrix P* really big and, apart from storage problems, it further increases the number of the summation terms in the ML-EM iteration with the consequence of slowing down the reconstruction process. An alternative approach is the so-called PSF-based reconstruction. The method assumes the knowledge of the Point Spread Function (PSF) of the specific PET system. The derivation of the PSF can be obtained through analytical derivations [57], Monte Carlo simulations [58, 59] or experimental measurements [60]. The inclusion of the PSF in ML-EM has been shown to improve spatial resolution and to generate less noisy images. There are several ways to include such a term in the ML-EM. For example, a common approach is to implement PSF as a convolution either with the image or with the sinogram during the reconstruction process. Both approaches are acceptable since some of the resolution loss effects are characteristics of the sinogram space (such as resolution blurring due to the detector) while others are more conceptually related to the image space such as the positron range.

7 Clinical scanners: state of the art

7.1 Hybrid imaging

Hybrid imaging can be defined as the use of information derived from images obtained with different techniques to provide the answer to a single clinical question. The power of hybrid imaging increases when the two techniques not only provide complementary information but also help each other in improving the quality of the images with respect to a stand-alone technique. When two techniques are used in combination there could be significant advantages in merging the two imaging systems in a single scanner. In this case, we refer to them as *hybrid systems*.

One brilliant example of hybrid imaging is the combination of PET and X-ray computed tomography (CT) [13].

CT is a medical imaging technique able to measure the distribution of linear attenuation coefficients ($\mu(x, y, z)$) in sections of an object. The clinical information that can be derived from $\mu(x, y, z)$ is essentially an anatomical map of different tissues or cavities within the body. In some cases, a contrast agent (in the form of a highly attenuating material, such as Iodine or Barium) is used to enhance contrast of selected organs.

The information derived from a CT scan is then highly complementary to the PET information since the CT provides an anatomical reference to the activity density map $\rho(x, y, z)$. In addition, tissues are well characterized in possible anatomical abnormalities as a consequence of diseases while PET is able to provide functional or molecular information. For example, in oncology, CT can provide the size and location of a tumor while PET provides the metabolic characterization of the lesion. Information from CT images can be further used to improve PET image quality to aid its quantification pro-

cess. For example, the knowledge of the real size of lesions (especially when small) provides useful information for correcting the measured activity in a certain volume with the most appropriate *recovery coefficient*, thus correcting for the partial volume effect.

This perfect marriage gave soon birth to the most successful hybrid system: the PET/CT. The main advantage consists of obtaining morphological and functional information almost simultaneously and without moving the patient. Images obtained in this way can be considered intrinsically fused with minimal distortions or motion blurring. A further advantage of the hybrid PET/CT is the possibility to obtain attenuation coefficients from CT to be used, after some corrections, for the attenuation correction of PET data (see Sect. 7.4), thus further improving the quantification capability of PET. The combination of PET and CT has brought such great innovation, especially in oncology, that PET/CT can be considered an imaging system itself. Since then, scientific and clinical success has also become a commercial success. As of today, no stand-alone PET systems are available on the market anymore.

7.2 PET/CT instrumentation

A PET/CT hybrid system comprises a PET scanner and a CT scanner axially juxtaposed and sharing the same geometrical axis. From the engineering point of view, the major difficulty stays in the precise mechanical integration. The two scans, even if separated, must perform in a well-known relative reference frame so as to be able to fuse the two images. Possible misalignments may be due to non-optimal translational motion of the patient bed along the axis or, e.g., to the flection of the bed itself.

The PET component of a typical PET/CT is not different from a stand-alone PET. Bigger differences can be observed in the CT component. In principle, the quality of CT images to complement the PET information can be lower than that of diagnostic CT systems where a higher spatial resolution is required. Nevertheless, to fully exploit the clinical potential of PET/CT a high-quality multi-slice CT component is mounted in high-end commercial PET/CT.

7.3 CT technology in brief

A comprehensive description of a modern CT system is beyond the scope of the present paper. However, some of the technological features of CT systems are described for a better comprehension of the potential of PET/CT. The reader is referred to Refs. [61, 62] for a full description of a CT system.

Computerized Tomography is based on the measurement of the transmission property of an X-ray beam. Similarly to the tomographic acquisition already described for PET, a CT system is able to collect line integrals of $\mu(x, y, z)$ at different angles and then reconstruct the image through algorithms that are typically analytical.

To perform this task, a CT system comprises an X-ray source and an X-ray detection system located on the opposite side of the object/patient. This entire system is able to rotate around the object so as to collect enough information for image reconstruction. The line integral is measured along a direction defined by the position of the X-ray

source and the opposite detector. For this reason, the detector is finely pixelated and extends along the necessary arc so as to cover the whole diameter of the field of view. The rotation is performed continuously as the acquisition is performed at about one round per second or less. X-ray sources for PET are high-power X-ray tubes with an output energy spectrum ranging between 80 and 140 kVp. Hence, it must be noted that the measured $\mu(x, y, z)$ distribution is obtained with a continuous spectrum of photon energies.

X-ray detectors for CT are based on ceramic scintillators coupled to solid-state photodetectors. The detector is subdivided into a sort of matrix. The size of each element of the matrix affects the spatial resolution that can be obtained in the reconstructed image. On the other hand, when elements become too small statistical limitations in the number of counts may affect the noise properties of the image, especially when a low dose is a clinical constraint. Modern CT systems feature detectors with 600–900 columns and 1–64 rows (the latter placed along the axial axis). Each element is about 0.6 mm $\times$ 1 mm. The number of rows is correlated to the number of sections (or slices) of the patient that can be obtained in a single detector rotation (without any axial motion). Scanners with a single slice of detectors are today obsolete. Scanners with more than one slice (Multi-slice CT) are classified according to the number of slices. The greater the number of slices the larger is the section of the patient that can be scanned with a single rotation and the shorter the scan time required. A lower dose could be delivered to the patient with the use of a multi-slice CT. In order to further reduce the dose to the patient at the expense of the spatial resolution, CT detector pixels can be grouped together to mimic larger pixels. As of today, all CTs feature the possibility to perform helical scanning (*spiral CT*), i.e., the patient is translated during detector rotation [61]. Tomographic data obtained during the scan are then interpolated to create missing projections. The advantages of this approach are essentially a reduction in scan time for whole body acquisition and a reduced dose delivered to the patient with respect to sequential scans, where images from standard circular acquisitions (taken at different axial positions of the patient) are stitched together to create the whole image volume.

7.4 CT-based attenuation correction for PET

The limitation of attenuation correction methods based on rotating sources transmission scans has been described in Sect. 6.5. These types of transmission scans produce noisy attenuation maps. Such noise is easily transferred to PET images when AC is performed, thus significantly increasing image roughness and degrading uniformity. Such limitation can be overcome with the use of the attenuation information obtained from a CT scan [63]. Thanks to the high flux of X-rays used in CT scanning, low noise attenuation maps can be derived in a fast and precise way. On the other hand, the values of the attenuation coefficients are far from being accurate. In fact, the attenuation coefficients $\mu_{\mathrm{CT}}(x, y, z)$ obtained at the CT energies are far from the values of those at 511 keV $\mu_{511\mathrm{keV}}(x, y, z)$ that should be used for PET attenuation correction. The CT-based attenuation correction must then pass through an energy conversion step (called *energy scaling*) where $\mu_{511\mathrm{keV}}(x, y, z)$ are derived from $\mu_{\mathrm{CT}}(x, y, z)$. First,

to make the $\mu_{\mathrm{CT}}(x, y, z)$ nearly independent (at least for mixtures of air and water) from the used CT energy, the Hounsfield Units (HU) are used:

$$HU = \frac{\mu_{\mathrm{tissue}} - \mu_{\mathrm{water}}}{\mu_{\mathrm{water}}} \times 1000. \tag{34}$$

In such a way, the attenuation coefficient of a given tissue (μ_{tissue}) is always referred to the value measured for water ($\mu_{\mathrm{water}} = 0$ HU), while, for example, $\mu_{\mathrm{air}} = -1000$ HU.

Energy scaling cannot be performed with a simple multiplicative factor. In fact, for the energies in use, the relative probability for the various interactions to occur (Compton or photoelectric) varies significantly between CT energies and 511 keV for the various tissues in the human body. In particular strong variations can be observed between bones and soft tissues. For that reason, in its simplest form, energy scaling is obtained with a linear scaling with a coefficient from −1000 HU up to a given HU, and with a different coefficient (typically lower) above that value of HU. In the lower range of HU soft tissues are included while bone lays in the upper range of HU. Conversion coefficients and threshold values are usually suggested by the scanner manufacturer. Some more complex scaling is also used sometimes but it is still based on some form of linear conversion. The linear scaling approximation fails in the presence of high Z materials that cannot be approximated as a mixture of air, water and bone. This may occur in the presence of metal implants or when CT contrast agents are used.

7.5 Time-of-flight PET

Some noise is also introduced by the reconstruction algorithm due to the ill-posedness of the line integral model [52]. As described in Sect. 6.6, the image reconstruction in PET is based on the Line of Response (LOR) determined by the two elements that detect the two γ-rays in coincidence. The positron annihilation point is assigned an equal probability along the chord which is the intersection of the LOR with the human body. In principle from the difference in the arrival time of the two photons onto the opposing elements it would be possible to determine the exact position of the annihilation point as described in Fig. 18. The time of arrival of the two photons emitted from point C to detectors A and B are given by $T_A = dA/c$ and $T_B = dB/c$, where D is the total distance between the two detectors, dA and dB the distance from the annihilation point to the corresponding detector for photon A and B, respectively, and c is the speed of light. dA and dB are related by the constraint $dA + dB = D$. The difference in arrival time is then given by

$$\Delta T = T_A - T_B = \frac{dA - dB}{c} = \frac{2 \cdot \Delta S}{c}, \tag{35}$$

where ΔS is the displacement of the annihilation point from the center. Inverting Eq. (35), ΔS can be then estimated as

$$\Delta S = \frac{c \times \Delta T}{2}. \tag{36}$$

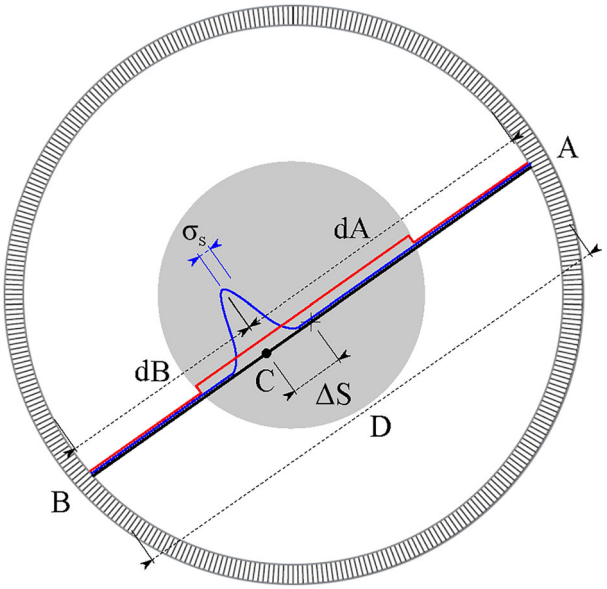

Fig. 18 The time-of-flight PET concept. The displacement of the annihilation point along the LOR (ΔS) is obtained by measuring the difference in arrival time ΔT (see text). Blue and red lines show how data are distributed along the LOR during the retroprojection step. Non-TOF data (red) are uniformly distributed along the LOR while TOF data are distributed around the emission point thus increasing SNR in the reconstructed image

Hence, if one measures ΔT with an infinite precision one obtains the exact difference ΔS and the values dA and dB, thus exactly locating the positron annihilation in 3D. However, because of the finite precision on ΔT, σ_T, the associate uncertainty on ΔS is

$$\sigma_S = \frac{c \cdot \sigma_T}{2}, \tag{37}$$

where σ_T is the CTR/2.35. This technique is called *Time of Flight* PET (TOFPET) because it makes use of the difference in the time of arrival of the photons onto the opposing detectors and it is based on a very high time resolution. As discussed in Sect. 5.1 the time resolution depends upon many factors, mainly the scintillator decay time and the photodetector time jitter. In standard clinical PET a coincidence time resolution of about 1–2 ns (FWHM) is obtained, which provides a spatial resolution along the chord of 15–30 cm, i.e., it does not give useful information for the third coordinate along the LOR. In TOFPET scanners that have CTR of about 500 ps it would be possible to measure the position of the annihilation point with a precision of $\sim$ 7.5 cm (FWHM).

Hence TOF measurements do not improve directly the spatial resolution of a PET reconstruction, which is of the order of 4 mm in clinical PET but contribute to increasing the SNR of the image (Fig. 18).

The concept of TOFPET was introduced in the early 80s [64]. The first prototypes were based on CsF and BaF_2 scintillators that have a very fast decay time. Although

the obtained time resolution on the bench was about 200 ps, it was about a factor 3 worse on the full system [65, 66]. In addition, the light photon yield produced by these scintillators (with a privileged emission in the UV for BaF_2) was rather low, as was their density and Z, thus impairing efficiency and increasing statistical noise. More recently, faster and lower noise photodetectors have allowed reaching a CTR of about 200 ps FWHM on a clinical PET (Siemens Digital Biograph Vision PET/CT) [67]. In this latter case, the related indetermination on the third coordinate will then be of ∼3.0 cm. Although this does not allow a sufficient spatial resolution to immediately obtain a 3D reconstruction it has been proved that this information improves the signal-to-noise ratio as

$$\mathrm{SNR_{TOF}} = \sqrt{\frac{2 \cdot D}{c \cdot \mathrm{CTR}}} \cdot \mathrm{SNR_{no-TOF}}.$$

A lot of research is going on in this field, also for PET-dedicated devices where the TOF technique could be even more beneficial, e.g., combined PET-Ultrasound (see Sect. 9.5) and PET in Hadrontherapy (see Sect. 9.7). A full review of the TOFPET technique can be found in Reference [68].

7.6 Image reconstruction in TOFPET

Also in the case of TOFPET image reconstruction is applied on data stored in sinograms. In the case of TOF data, the sinogram-based approach consists in dividing the maximum allowed time difference between the arrival of the photons into n_{TOF} intervals and thus generating an equal number of sinograms, each corresponding to a specific time interval. All TOF sinograms are then used in the reconstruction process by introducing a proper weight to take the TOF information into account.

7.7 Clinical value of PET

The starting point towards the clinical use of PET was in 1978 when ^{18}F-FDG was synthesized by Wolf and Fowler's group at Brookhaven [69]. The importance of ^{18}F-FDG derives from the fact that its uptake into a living body can be immediately interpreted as the glucose metabolic rate by using the Sokoloff model, originally validated with ^{14}C-DG [70]. This compartment model only requires the measurement of the time course of radioactivity in arterial blood to obtain the Standard Uptake Value (SUV) of FDG in the target, thus providing a semi-quantitative measurement of the local cellular activity. Anomalous SUV values can be an indication of the malfunctioning of an organ or of the presence of a tumor. The capability of ^{18}F-FDG was immediately proved on human volunteers by the UCLA group in 1979 [71]. It was soon clear that this procedure could allow imaging and quantification of metabolic disturbances in cardiology, oncology, and in neurological diseases or disorders. Since then important studies have been done on myocardial viability both using ^{13}N-ammonia and ^{18}F-FDG tracer at UCLA [72], but the "killer application" was the use of PET in oncology. The UCLA group presented the first whole-body

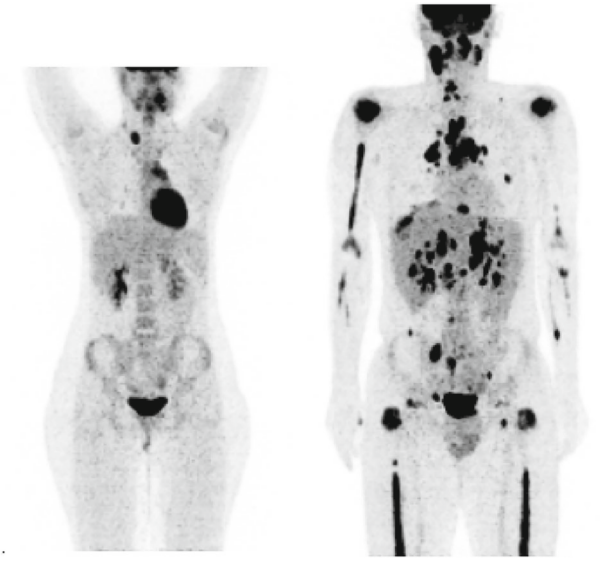

Fig. 19 ^{18}F-FDG PET/CT for the staging of Hodgkin Lymphoma patients. 2D sagittal images: (left) tumor at stage II; (right) tumor at stage IV . (Courtesy of Paola Erba, University of Pisa, 2014)

oncology images in 1992 [73] and the Food and Drug Administration (FDA) in 1997 approved ^{18}F-FDG as a radiotracer. Finally, PET reimbursement was approved in 1998 in the USA for lung cancer and cardiovascular diseases. It is now estimated that most PET scans worldwide make use of ^{18}F-FDG. Almost all PET exams are now made with a PET/CT (see Sect. 7.3) so that the CT provides the anatomy of the patient and allows applying the attenuation correction to the PET images.

We will just provide here two examples of typical oncology applications of ^{18}F-FDG that show the ^{18}F-FDG PET capability of tumor staging and of evaluating the results of a treatment, as an indication for the prognosis of Hodgkin lymphoma.

In Fig. 19, the staging of two patients with Hodgkin lymphoma imaged with ^{18}F-FDG PET are presented. The left and right patients have been diagnosed with a tumor stage II and IV, respectively. In Fig. 20, a case of Hodgkin lymphoma response to chemotherapy is shown: images of the patient before (left) and after treatment (right) show an example where there has been no complete response to chemotherapy. It is important to underline that having the possibility of evaluating the effect of therapy by PET imaging without waiting for clinical changes gives a great advantage in terms of modifying/tailoring an effective therapy for treating the tumor. Many other radiotracers in oncology are ^{18}F-based, e.g., ^{18}F-FLT for measuring tumor cell proliferation and ^{18}F-MISO for measuring tumor oxygenation. Both this information together with the ^{18}F-FDG metabolism are extremely useful in modern radiotherapy for optimizing treatment planning.

^{18}F-FDG PET is also helpful in making differential diagnoses, for instance between inflammation and tumor, notwithstanding the fact that the tracer is a-specific and accumulates in all the cells that are avid of glucose, and in confirming an Alzheimer clinical

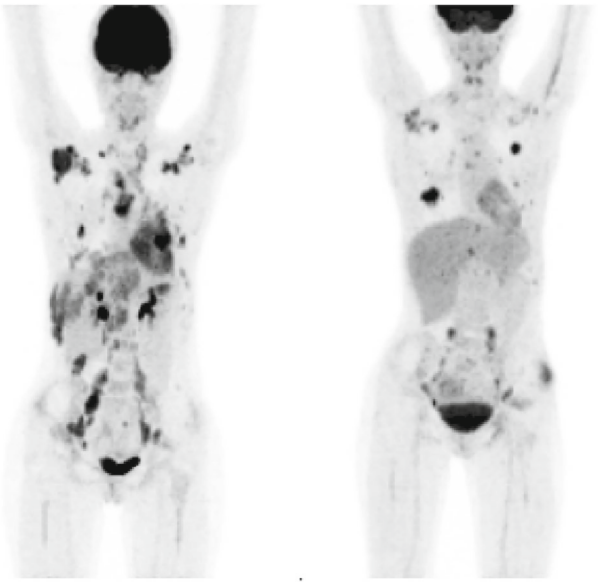

Fig. 20 ^{18}F-FDG PET/CT for the evaluation of the response to chemotherapy in a patient with Hodgkin Lymphoma, see text . (Courtesy of Paola Erba, University of Pisa, 2014)

diagnosis. In 2002, a specific ^{11}C radiotracer for amyloid imaging was developed at the University of Pittsburgh, called *Pittsburgh compound B* [74]. This new radiotracer allows visualizing the amyloid plaques in Alzheimer patients. Several radiotracers both ^{18}F and ^{11}C based have been developed for neurology and psychiatry, i.e., neuroreceptors, dopamine D2/D3 receptors and serotonin transporters. One of the most notable applications is the F-Dopa tracer and L-Dopa drug for Parkinson disease. Additional specific radiotracers are labeled with other radioisotopes, e.g.,^{13}N,^{68}Ga and ^{64}Cu. All provide ample opportunities for diagnosis, prognosis and follow-up of neurological, cardiological and oncological diseases.

Positron Emission Tomography is now used in most of the sub-specialities of medicine and is considered an indispensable instrument in prevention, diagnosis, treatment planning and treatment response, and complementary to all-omics investigations. Since this review paper mostly addresses the basic science of PET and its technological development, the interested reader is referred to [75, 76] for a thorough review of the clinical applications of PET.

8 Pre-clinical scanners: state of the art

8.1 Introduction

From the ‘90s, the fast and intensive development of high-resolution detectors has allowed the building of PET scanners with unprecedented spatial resolution. This made it possible the construction of PET systems dedicated to pre-clinical studies on

small animals. Initially, most of the scanners were built as research prototypes using a wide range of technologies, from a sort of miniaturized block detectors to high-density avalanche gas chambers and using rotating or non-rotating detectors. Soon, the strong scientific interest in small animal systems encouraged the development of commercial products. The first two on the market were the MicroPET, designed and developed at UCLA [77], Los Angeles, and produced and commercialized by Concorde Microsystems Inc. (USA) and HIDAC-PET, produced by Oxford Positron Systems Ltd. (UK) [30].

In the following years, with the consolidation of detector technologies and the increasing interest in molecular imaging (see Sect. 2) major players entered the pre-clinical PET instrumentation market. Among the others, SIEMENS, GE Healthcare, Mediso Medical Imaging Systems launched their own products usually as a result of the technological transfer from Universities. As of today, many other companies, such as, for example, Inviscan, Sedecal, TriFoil Imaging or PerkinElmer, are manufacturing and distributing small animal PET systems.

8.2 Beyond the block detector: high-resolution PET detectors

The relatively small size of the animal under study in pre-clinical imaging makes it difficult the use of imaging instruments developed for human subjects. The spatial resolution of the available clinical PET scanners, as of today not better than 3–4 mm FWHM, is not satisfactory for quantitative and qualitative imaging on rats and mice. Molecular small animal imaging requires instruments with a finer spatial resolution. In order to obtain the same detail visualization as for human scanners it would be necessary to have instruments with a sub-millimetric spatial resolution. However, it is usually acceptable to work with a spatial resolution better than 2 mm FWHM for rats, while for mice it is recommendable to use instruments with a resolution close to 1 mm FWHM.

After the first attempt to develop high-resolution PET detectors using avalanche gas chambers (see Sect. 4) it was clear that such kind of technology, even if offering unsurpassed intrinsic spatial resolution, was affected by two major disadvantages: a poor sensitivity and a high complexity. For example, the HIDAC-PET [30] offered a spatial resolution of 1.2 mm FWHM by using an unconventional detector technology, based on multistacks of hybrid high-Z converter-proportional gas chamber planes, but it offered a very limited sensitivity of 0.89%.

For this reason, the solution based on finely pixelated scintillating crystals coupled with photomultiplier tubes was the most widely used, mainly for its robustness and simplicity.

When using matrices of scintillating crystals as interacting media for PET detectors, the precision of localization is related to the size d of the detector element (more precisely the detector pitch). In this case, the pixel size contribution in the spatial resolution (formula (16)) is $d/2$, while the coding factor is $b \geq 0$. Due to the available technology and a pixel pitch down to 1.1 mm, present small animal systems have a typical spatial resolution of about 1.0–1.6 mm FWHM at the center of the field-of-view [78].

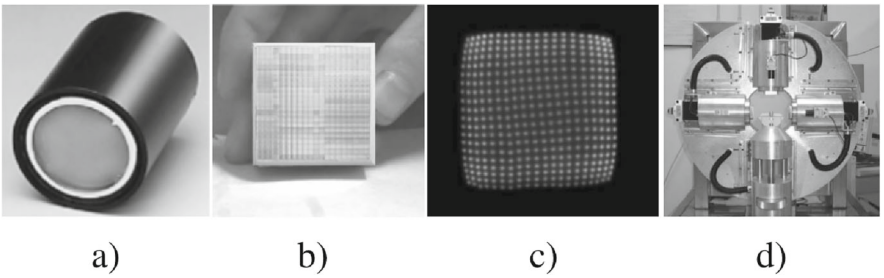

Fig. 21 Example of the application of a Hamamatsu R2486 PS-PMT. **a** Picture of the R2486. **b** A YAP:Ce matrix of 20 × 20 crystals with a 2.0 mm pitch. **c** Flood field image of the YAP:Ce pixel (irradiated with 511 keV γ-rays) as obtained with an R2486 PS-PMT with a resistive chain readout. **d** The combination of the R2486 and the YAP:Ce matrix was used as the building block for the detection system of the YAP-(S)PET pre-clinical scanner featuring four rotating heads [80]

Position-Sensitive Photomultipliers Because of its moderate sampling, the standard four PMTs configuration of the block detector is not adequate for reading out such finely pixelated matrices and position-sensitive PMTs have to be used, instead. The first large-area position-sensitive PMT (Hamamatsu R2486, 3 in. diameter) was developed in 1985 [79] and represented a strong technological advance for gamma-ray imaging. The first generation was based on proximity mesh dynodes by means of which the charge was multiplied around the original position of the light photon striking the photocathode. In this kind of tube, the charge shower has a wide but controlled intrinsic spread and is collected by a crossed-wire anode structure.

Such a family of position-sensitive tubes was characterized by a large detection area (up to 5 in. diameter) but the round geometry and the large peripheral dead area (1 cm or more) prevented these tubes from being tightly assembled in arrays. The Hamamatsu R2486 was used for the construction of a small animal PET scanner (YAP-PET) in 1998 [80] (Fig. 21). In its latest evolution [81] the YAP-(S)PET was made up of four rotating detector heads each composed of an R2486 tube and a matrix of 27 × 27 elements of YAP:Ce crystal (1.5 mm × 1.5 mm × 20 mm size). Due to the planar detector configuration and the use of the YAP:Ce scintillator, the YAP-(S)PET has also SPECT capability by simply adding a parallel hole lead collimator in front of each crystal, and can even perform simultaneous PET/SPECT [82]. In years 2003–2006 the YAP-(S)PET was commercially available from ISE s.r.l., Pisa, Italy.

The second PS-PMT generation was based on metal channel dynode for charge multiplication by which the intrinsic spatial resolution is reduced to 0.5 mm FWHM. A further technological improvement consists of a metal housing that allows a very compact size (about 1 in.). In 1997 the first version of these tubes (model R7600-C8) was employed for the construction of the MicroPET at UCLA [77]. In the R7600-C8 the position-sensitive detection is performed with a special anode made of $4(X) + 4(Y)$ crossed plates. The shape is now square, with an active area of 22 mm × 22 mm. The overall dimensions are 26 mm × 26 mm (area) × 20 mm thick.

In the MicroPET's implementation, the R7600-C8 tubes were used to read out small LSO matrices with 2 mm pitch crystal elements, arranged in a ring geometry. However, the dead area around this tube still prevents a ring configuration with negligible gap size

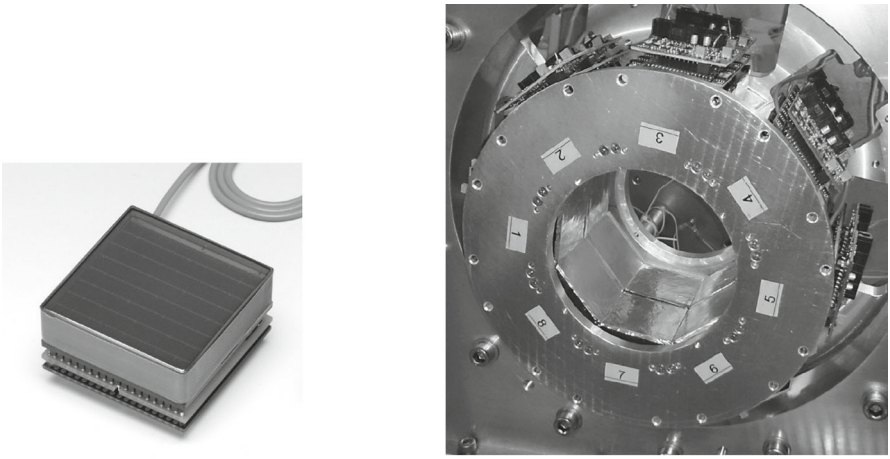

Fig. 22 Left: picture of the Hamamatsu H8500C MA-PMT. Right: picture of the detector systems of the PET component of the IRIS PET/CT [84]. The picture shows the arrangement of the 16 detectors in two octagonal rings

between adjacent scintillating matrices. In order to overcome the packing limitations, a bundle of square fibers (1 mm^2) section was used as a light guide between the scintillators and the PSPMTs.

The evolution of this photodetector was then used in the second and third generations of the MicroPET family (MicroPET Focus and Inveon by Siemens). For example, the MicroPET Focus 120 series used the Hamamatsu R5900-C12 (with $6(X) + 6(Y)$ crossed plates) to read out a 12×12 array of LSO crystal elements coupled to the tube via a bundle of 8×8 optical fibers. Each LSO crystal measured 1.51 mm $\times$ 1.51 mm $\times$ 10.00 mm. The Siemens Inveon was, in turn, using a further evolution of this PS-PMT now called R8900-C12.

Hamamatsu H8500 Flat Panel PMT [83] was the latest generation (usually indicated as the third) of position-sensitive PMTs (Fig. 22, left). Its main feature is the extreme compactness with a minimum peripheral dead zone, resulting in an active area of 89% of the whole surface and a reduced height (12 mm), still maintaining the performance as close as possible to the second-generation tubes. The H8500C tube consists of a 12-stage metal channel dynode for charge multiplication and 8×8 anodes for charge collection and position calculation. For the different anode structures from those of the first (crossed wire) and second (crossed plates) generations, this kind of tube is usually indicated as multi-anode PMT (MA-PMT). It is designed to be assembled into an array to cover a large detection area. This tube has a very compact package with a metal envelope thickness of just 0.25 mm. The external size is 52 mm $\times$ 52 mm $\times$ 28 mm and the active area is 49 mm $\times$ 49 mm. Each individual anode is 5.8 mm $\times$ 5.8 mm in size with a 0.28 mm inter-anode spacing, corresponding to an anode pitch of 6.08 mm. This kind of tube allows the design of densely packed detection systems with minimal detector-to-detector gaps. For example, Hamamatsu H8500C PMTs are utilized in the construction of the IRIS PET/CT pre-clinical system distributed by Inviscan s.a.s. (France) [84]. In this case, The PET component of the scanner consists

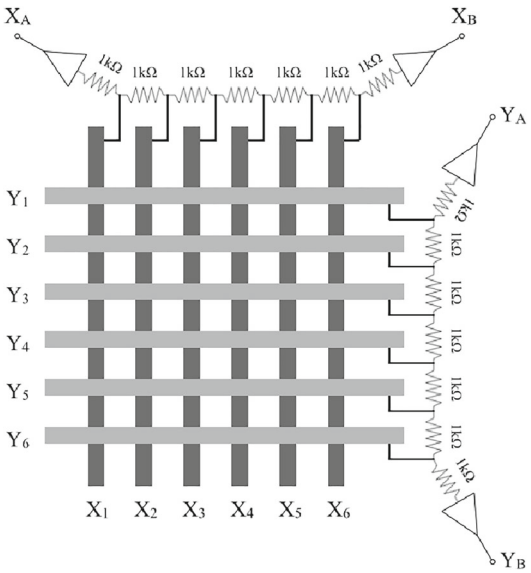

Fig. 23 Example of the resistive readout of $6(X) + 6(Y)$ crossed plate anodes

of 16 modular detectors arranged in two octagonal rings (Fig. 22, right). Each detector module is in coincidence with the 6 opposing modules (three in the same ring and three in the other ring). The corresponding field-of-view has 95 mm axial coverage and a diameter of 80 mm. The H8500C is used to read out a LYSO:Ce matrix of 702 crystals of 1.6 mm × 1.6 mm × 12 mm with a pitch of about 1.7 mm.

Finer sampling PMTs are also available from Hamamatsu. For example, the H9500 model has 16×16 independent anodes. Thanks to these characteristics the Hamamatsu H8500/H9500 line is the preferred choice for the design of PMT-based small animal PET detectors, featuring either multi-ring or planar geometries.

To fully exploit the performance of MA-PMTs each anode should be independently acquired (multi-anode readout) like the four outputs of a block detector. However, in order to simplify the complexity of the readout system, resistive chains [85, 86] can be used to reduce the number of output channels.

For example, with the C12 family, the $6(X) + 6(Y)$ anodes can be read out via a simple resistive chain. Each anode can be connected to the adjacent one with a $1k\Omega$ resistor, as shown in Fig. 23. The two X position signals (X_A and X_B) are then given by the expressions:

$$X_A = \sum_{n=1}^{6} X_n \frac{7-n}{7} \tag{38}$$

$$X_B = \sum_{n=1}^{6} X_n \frac{n}{7}, \tag{39}$$

where X_n is the current in the nth wire along the X direction. Similar expressions determine the Y_A and Y_B signals. In this way, the position information of the scintilla-

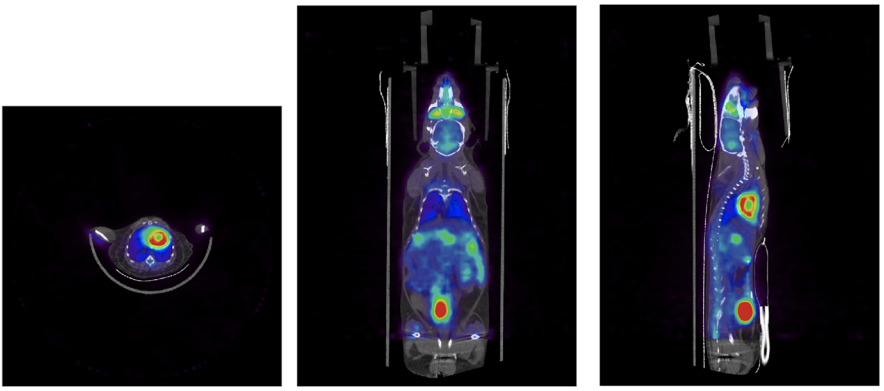

(a) Transaxial section (b) Coronal section (c) Sagittal section

Fig. 24 Co-registered PET/CT image of a mouse obtained with a pre-clinical system. The mouse was injected with 4 MBq of ^{18}F-FDG, intraperitoneal injection. Images obtained with the IRIS PET/CT system. (Courtesy of P. Salvadori, P. Iozzo, IFC-CNR Pisa, Italy.)

tion point can be obtained by means of a center of mass calculation, similar to that used with crossed-wire PS-PMT. Thus, the four signals give the X position measurements by using the following formula:

$$X = \frac{X_A - X_B}{X_A + X_B}, \tag{40}$$

A similar formula is used for the Y coordinate.

The position encoding readout of the H8500 tube is slightly more complicated. For example, a circuit based on the Symmetric Charge Division (SCD) scheme can be used. The SCD circuit is based on the orthogonal positioning algorithm used in multi-wire position-sensitive photomultiplier tubes. Each anode is connected to any other belonging to the same row and column in such a way that the anode structure is similar to an 8 + 8 crossed-wire structure. Each row and column is then connected to a pre-amplifier. The eight outputs of both row (X) and column (Y) are then connected with a simple resistive chain to obtain two X and two Y positioning signals using Eq. (40).

An example of the imaging capabilities of the IRIS PET/CT pre-clinical system is shown in Fig. 24. A mouse is injected with ^{18}F-FDG and the three typical sections are presented from left to right: transaxial, coronal and sagittal, respectively. The color coding goes from red (high uptake) down to blue (low FDG uptake). The left ventricle of the heart is clearly visible. The high uptake region at the bottom of the coronal and sagittal sections is the bladder.

Depth encoding detectors In order to maximize the efficiency of the PET system, the PET heads should be positioned close to the object and the thickness of the photon absorber should be at least one attenuation length at 511 keV.

In this case, the PET system is exposed to a severe parallax error, which is due to the lack of depth-of-interaction information (see Sect. 5.5). A number of techniques

for designing detectors with the capability to estimate the depth of interaction (DOI) have been proposed. These solutions are based either on the direct measurement of the DOI within the crystal (in this case the DOI information is continuous) [87, 88] or by segmenting the crystal into two layers so that the photodetection system is able to discriminate in which layer the event occurs (discrete DOI information) [89, 90].

Although the high potential advantages in using DOI capability only a few present commercial small animal PET systems are actually implementing it. Two systems use 2-layers phoswich crystal matrices of LYSO/LGSO scintillators, namely the Argus system (distributed by Sedecal) and the LabPET system (included in various systems distributed by TriFoil Imaging). Another small animal PET system with DOI capability is the Albira system, distributed by Bruker Corporation. The Albira uses monolithic crystals instead of pixelated matrices. Using this solution, the precision of localization is related to the positioning performance of the photodetector. The pixel size contribution is $d = 0$ while the coding factor is $b > 0$. The DOI is estimated considering the width of the light spot illuminating the PMT: the smaller it is, the deeper the interaction occurs and vice versa.

In summary, the latest generation of multi-anode PMTs has contributed to the spatial resolution of small animal PET systems to reach values very close to the ultimate limit of PET (close to 1 mm FWHM). However, while the PMT technology still represents the state of the art for high-resolution PET, solid-state photodetectors are now the preferred solution for PET mainly thanks to the consolidation of the Silicon Photomultiplier technology. Solid-state photodetectors (see Sect. 9.1) are not a novelty in this field. Various attempts to use Avalanche Photodiodes (APD) have been explored in the past. The major advances, in this case, were the fine granularity of these devices that allowed the one-to-one coupling configuration to fine scintillating pixels. For example, the LabPET, originally developed at the University of Sherbrooke (Canada), uses an array of APDs with 2 mm pitch coupled to equally spaced crystal pixels. Conversely to the monolithic crystal case, in the one-to-one coupling, the coding factor is nearly zero while the pixel contribution is still $d/2$. Today, a major interest in the solid-state photodetector solution (see Sect. 9.1) stays in the intrinsic compatibility of such devices with magnetic fields, thus opening the possibility to develop integrated PET/Magnetic Resonance (MR) devices (see Sect. 9.3). Latest systems, incorporating the high granularity detectors and in some cases DOI capability, offer a volumetric spatial resolution of about 1 mm^3 that is very close to the theoretical limit.

9 Actual trends and future developments

9.1 New photodetectors

Scintillator crystals coupled with photomultipliers tube (PMT) have been the basic choice for most PET detectors since the late '80s of last century [91]. Given the long history of developments of PMTs and scintillators, the technology is nowadays mature in all aspects comprehending also the electronics and fabrication techniques. PMT is the most common photodetector in use in PET thanks to the combination of advantageous features such as high gain (typically of the order of $\approx 10^6$), low noise, fast

response and rather low cost. Nevertheless, new developments in the PET technique impose requirements on the photodetectors that cannot be completely satisfied by the vacuum tube technology. Although it would be desirable to have an individual coupling of the scintillators to the photodetectors, it becomes more and more difficult to achieve it with PMTs as the size of the crystal is reduced to $\approx$ 1 mm to improve spatial resolution. Position-sensitive photomultiplier tubes (PS-PMT) with resistive anode for charge collection or multi-channel photomultiplier tubes with multi-anode readout (MA-PMT) can be used to multiplex several small crystal pixels into a reduced number of readout channels. Although the position of the interacting photons on the PS-PMT or MA-PMTs can be obtained with high precision, light cross-talk between adjacent crystals and PMT glass envelope, as well as photon statistics, can affect the crystal identification accuracy, thus degrading the spatial resolution. Other effects like multiple Compton events can be difficult to identify with light- or charge-sharing detection systems with a consequent loss of contract resolution. Another limitation of the multiplexed systems is the pulse pile-up and the dead time that limit the performance for PET applications where a high count rate is expected (see for instance online PET monitoring in hadrontherapy, Sect. 9.7).

The actual trend in medical imaging is the multimodality approach which is a combination of different techniques to provide fused images with improved diagnostic information. The latest frontier of multimodality is the hardware integration of PET and MR scanners in a unique device. With the PMT technology, such integration would be extremely complicated due to the large sensitivity of the vacuum tubes to magnetic fields. Even very weak magnetic fields affect the PMT signals due to the deflection of the electron trajectories between the photocathode and dynodes. Significant variations of gain and of energy resolution have been observed for PMTs as the magnetic field exceeds $\approx$ 10 mT [92] and the decoding of the crystals is totally compromised for magnetic field strengths typical of the MR clinical devices. Most of the aforementioned issues have been successfully addressed by solid-state photodetectors as an alternative to PMTs both in commercial PET scanners and in research applications. The next subsections describe the working principles of the photodetectors most used in PET and present a review of pre-clinical and clinical devices based on solid-state technology.

Solid-state photodetectors were first produced in the early forties with the invention of the p-n junction in silicon and the study of its optical properties [93]. They received a major boost in the sixties when the p-i-n (PIN) photodiode was developed and successfully used in several applications. The development of devices with internal gain, avalanche photodiodes (APD) first and then Geiger-mode avalanche photodiodes, named single-photon avalanche diode (SPAD), led to a substantial improvement in sensitivity and allowed single-photon detection. Later on, thousands of SPADs were assembled in arrays of a few millimeters squared (named silicon photomultiplier, SiPM) with single-photon resolution. The high internal gain of SiPMs, together with other features peculiar to the silicon technology like compactness, speed and compatibility with magnetic fields, promoted SiPMs as the principal photodetector competitor of photomultipliers in PET [94]. They can have a signal rise time shorter than 1 ns being suitable for applications requiring good time resolution as TOFPET. Moreover, silicon detectors can be fabricated in miniaturized sizes (of the order of

few mm^2), ideal for applications requiring high spatial resolution (pre-clinical PET) or compactness (intra-operative probes). Finally, APDs (and now SiPMs) enabled the construction of hybrid PET/MR systems. Silicon photodetectors are in fact insensitive to magnetic fields and do not require shielding. Moreover, the compactness of these devices has allowed the full integration of the two imaging techniques.

Avalanche photodiodes An avalanche photodiode (APD) is a p-n device with an internal gain due to the high electric field at the p-n junction. A photoelectron could reach energy to create an e/h pair by impact ionization. The original photoelectron and the additional one can generate further e/h pairs providing a charge multiplication. Thus, in the APDs, the signal generated by the incident light is internally amplified, typically by a factor of a few hundred. Even though the signal of an APD is amplified by the multiplication process, it is not high enough to be used without external amplification. The noise level of the device is dependent on the bias voltage and on temperature. APDs are usually connected to a cooling system to stabilize the signal, thus improving the signal-to-noise ratio. APDs have been also designed to collect the charge at different anodes, typically placed at the four corners of a square device, to obtain information on the position of the interaction of the detected photon. Using this kind of device, called position-sensitive APD (PS-APD), a matrix of scintillating crystals has been decoded [95, 96].

Silicon photomultipliers If the bias voltage of an APD is greater than the junction breakdown voltage, the charge multiplication is a diverging self-sustaining process (Geiger regime). A quenching resistor, connected in series with the junction, is used to interrupt the avalanche: when the current in the junction is high enough to generate a voltage drop across the resistor close to the applied overvoltage (i.e., the difference between the bias voltage and the breakdown voltage), the flowing current becomes low enough that the avalanche can be statistically quenched and the junction is recharged. The device based on this working mechanism is called Single Photon Avalanche Diodes (SPADs) [97, 98]. A SiPM (also known as Geiger-mode avalanche photodiode, G-APD or Multi Pixel Photon Counter, MPPC) is a device obtained by connecting in parallel several miniaturized SPADs (few tens of μm^2) belonging to the same silicon substrate so that the output signal of the SiPM is the sum of the SPADs outputs [99]. The small SPADs in the SiPM are named micro-cells. An electrical scheme of the SiPM (left) and the structure of a single micro-cell (right) are shown in Fig. 25. The SiPMs represent an effective alternative to the current detectors used in PET scanners, since they have a very fast rise time due to the Geiger mechanism [100], are insensitive to magnetic fields [101] and show high gain at few tens of bias voltage. Furthermore, arrays of SiPMs composed of single sensors as small as 1 mm^2 can be produced, either by assembling several devices in a matrix or by fabricating replicas of the same sensor on a common silicon substrate [102]. Both approaches have allowed the development of high spatial resolution detectors. A single-photon time resolution close to 80 ps FWHM [103] has been obtained by irradiating two SiPMs in coincidence with a laser source, while a standard deviation of about 20 ps has been achieved by increasing the number of micro-cells triggered simultaneously. This demonstrates that such photosensors can be applied in high-timing resolution PET detectors. The noise in SiPM devices is mainly due to the dark count rate: an e/h pair can be thermally generated, triggering an avalanche in a micro-cell without an optical photon impinging on it. The

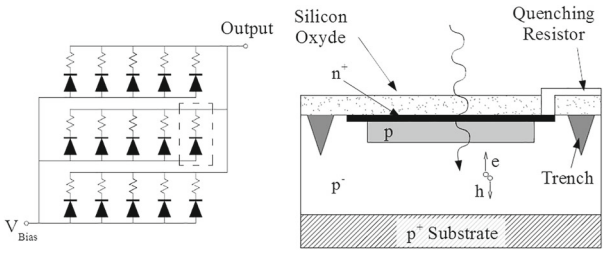

Fig. 25 Electrical scheme of a SiPM. The SPADs are connected on one side to the bias voltage end (Vbias) and on the other side, through the individual quenching resistors, to the Output end (left). The basic structure of a single micro-cell (right)

dark noise rate depends on the working temperature and on the overvoltage, and it is directly proportional to the active area of the device. The newest SiPM technologies guarantee a dark count rate of about 100 kHz/mm^2 at room temperature [104].

Digital versions of SiPMs have also been produced [105, 106]. Digital SiPMs (dSiPM) consist of an array of SPADs each one equipped with a locally integrated active quenching circuit. Moreover, additional circuits for digital processing, acquisition and readout of the optical signal are integrated in the sensor. For instance, the implementation of enabling logic to mask noisy SPADs allows for reducing the Dark Count Rate of the whole device. Furthermore, the digital signal processing circuit integrated in a dSiPM can be optimized for a specific application. For instance, in TOFPET a high-speed trigger network and an integrated TDC can be implemented to extract the time information in digital form. A comprehensive review of these devices is given in [107].

9.2 Pre-clinical and clinical PET and PET/CT systems based on solid-state photodetectors

The capability of PS-APD to give continuous information about the position of the interaction of the optical photons and the high granularity of APDs and SiPMs make these devices particularly attractive for applications requiring high spatial resolution. In pre-clinical imaging, due to the different dimensions of the anatomical structures of small animals with respect to humans, a spatial resolution below the millimeter is needed to obtain in mice the same functional information that is provided by clinical scanners based on pixelated crystals of 4 mm pitch. To achieve such a high spatial resolution, the capabilities of both pixelated (with pitch of 2 mm or smaller) and continuous crystals have been investigated, showing the advantages and limitations of both solutions.

Arrays of SiPMs with a pitch of 1.5 mm or less [102] have been produced and tested to decode arrays of scintillators with the same pitch. As mentioned earlier, monolithic arrays of SiPMs have been produced with minimal dead area among photo-sensors. An array of thin crystals (as small as 0.7 mm in size) has been decoded using an array of SiPMs with a 3 $\times$ 3 mm^2 active area and using light sharing between pixels [108]. However, a degradation of the energy resolution has been observed when using

thin crystals coupled to SiPMs, due to the limited light output efficiency of crystals with high *aspect − ratio* and to the saturation effect in SiPMs with a small number of micro-cells facing each scintillator. Results show an energy resolution between 15% and 17% for LYSO crystals of 1.5 mm × 1.5 mm section coupled to a SiPM array [109]. PS-APDs have been used to decode arrays of thin crystals with a pitch of 1 mm [95, 96], reading out the scintillator from both sides to maximize the light collection and identify the depth-of-interaction position of the photon in the crystal. A spatial resolution close to the millimeter at the center of the field-of-view has been reached in pre-clinical PET, using arrays of thin LYSO scintillating crystals [110]. Furthermore, position-sensitive SiPMs have been developed. These devices collect the signal of the SPADs at four anodes and the SPADs connections are such that an array of scintillators can be decoded with a single device using the center of gravity algorithm [111, 112].

The adoption of monolithic scintillating crystals coupled to photodetectors for high spatial resolution in pre-clinical systems [113, 114] had already been proposed using PMTs, but the availability of the compact solid-state photodetectors with small pitch allows further increasing the spatial resolution well below 1 mm FWHM thanks to a finer sampling of the light distribution. Monolithic crystals can also provide the depth of interaction of the photon since the light response, e.g., the width of the light spot reaching the output side, depends on this parameter, too. PET detectors composed of a slab of LYSO scintillator coupled to an array of SiPMs or APDs on one side [115, 116] or on two sides [117] have been developed. In these configurations, the scintillating photons are shared between several detectors. Therefore the light collection needs to be maximized using a white or reflective coating on the top surface of the crystal (readout on one side) and adopting arrays of photodetectors with a high fill factor. The lateral sides of the scintillator, instead, are usually painted black to avoid reflections that would destroy the spatial coherence of the light distribution. Still, the partial sampling of the light spot close to the edges of the crystals usually does not allow reconstructing the interaction position using an analytical centroid calculation. For this reason, several methods have been studied to reach a high three-dimensional spatial resolution over the entire volume of the crystal, using statistical methods [118, 119], non-linear least square methods based on empirical models of light distribution [120, 121] and artificial neural networks [122]. Furthermore, new bright crystals like $LaBr_3$:Ce [123] have been investigated [124]. Two detector architectures with depth of interaction capability implemented using SiPMs are represented in Fig. 26. The scheme of a monolithic crystal readout by photodetectors on one side (left) and on both sides (center) is shown. Even though a spatial resolution close to millimeter has been reached in monolithic detectors, their application to commercial systems is still limited because of the complexity of the calibration process. The development of a fast and handy calibration method could represent a breakthrough in the use of monolithic crystals in pre-clinical systems. In the last few years, a new interest in solutions based on monolithic crystals has risen again, thanks to the availability of more sophisticated AI-based algorithms that allow overcoming limitations and exploiting their full potential (see Sect. 9.8).

In the last ten years, there has also been outstanding progress in the application of digital SiPM to PET both in pre-clinical and clinical scanners. In 2012, Degenhardt et al. first published the performance of a small PET scanner prototype based on dSiPM

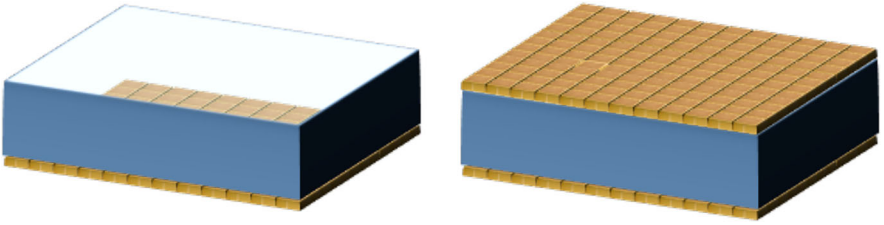

Fig. 26 Scheme of a monolithic crystal readout by photodetectors on one side (left, reflecting coating on top not shown) and on both sides (right)

arrays [125]. This ring consists of 10 modules and has a transaxial and axial field-of-view of 20 cm and 6.5 cm, respectively. Each module contains 4 detectors, each detector consisting of an 8×8 array of $4 \times 4 \times 22$ mm LYSO:Ce crystals coupled one-to-one to the pixels of a dSiPM array. The system coincidence time resolution (CRT) was found to be 266 ps, the energy resolution 10.7% FWHM and the spatial resolution 2.4 mm (reconstructed with an OS-EM algorithm).

The first commercial PET/CT clinical scanner based on the digital SiPM technology was released by Philips. Performance evaluation and first clinical trials of the whole-body TOFPET/CT system have been reported in [126–128]. The system comprises LYSO crystals $4 \times 4 \times 19$ mm coupled 1:1 to dSiPM sensors. The transaxial FOV is 676 mm and the axial FOV is 164 mm. The spatial resolution reported is 4 mm FWHM (both axial and transverse at 1 cm from the FOV center). The energy resolution is 11% FWHM and the CRT is 345 ps FWHM, which represents a significant improvement with respect to commercial TOFPET/CT based on PMT technology, where CTR is comprised between 500 and 700 ps. All these figures have been proved to be almost independent from the count rate.

9.3 PET/MR hybrid systems

Magnetic resonance (MR) reveals structure and functions through the interaction of a strong magnetic field with primarily the protons present in water and tissues and their chemical environment. This modality has also a good sensitivity (10^{-3}–10^{-5} mol/l) and an excellent spatial resolution (≈ 1 mm isotropic for clinical systems). The fusion of this anatomical MRI information with the nano-molar functional information given by PET provides a whole spectrum of information that can be used to understand new aspects of the anatomy and the physiology of a disease [129]. The principal applications of the PET/MR hybrid systems are diagnosis, treatment and follow-up of tumors, mainly of the head and neck, and of the abdomen and prostate, for which the superior imaging capabilities of MR for soft tissues over computed tomography (CT) are more relevant [130]. Furthermore, PET/MR opens new fields of neurology research thanks to the capability to provide co-registered images and to monitor time-dependent metabolic processes. The development of new bi-modal tracers can be particularly useful in the study of neurological diseases and in pre-clinical applications for pharmaceutical research.

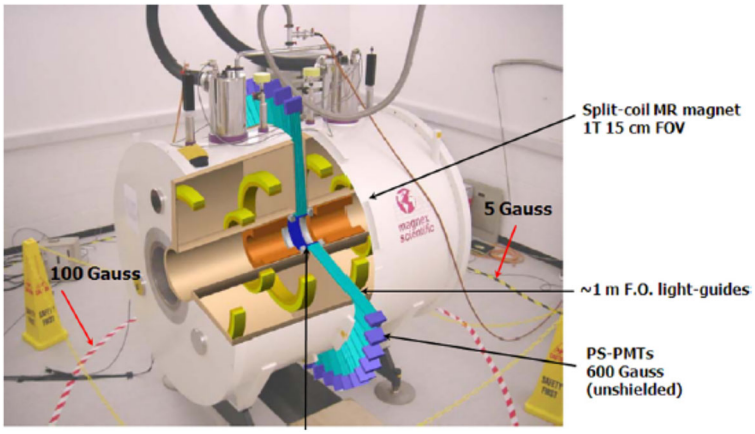

Fig. 27 Schematic of PET/MR system with split-magnet. The cut-away shows scintillating crystal ring (dark blue), fiber bundles (light blue), and screened PMTs (dark blue outside magnet cryostat) and "split" gradient coil (grey) [132]

Hybrid PET/MR scanners were initially developed using bundles of optical fibers or light guides to convey the light from the scintillator PET ring positioned inside the bore of the MR scanner to a region with low magnetic field where photomultiplier tubes read out the light without distortion of the signal due to the magnetic field [131]. Figure 27 shows the schematic of a PET/MR system with a split-magnet and PET ring scintillators connected to PMT through light guides as described in [132]. The cut-away shows a scintillating crystal ring (dark blue), fiber bundles (light blue), screened PMTs (dark blue outside magnet cryostat) and a "split" gradient coil (grey). The main limitations of these methods are the signal attenuation in the fibers and the complexity of the optical cabling for a PET system with a large field-of-view.

Scanners composed of a PET/MR tandem, in which the patient bed is automatically moved from the MR to the PET scanner have been also developed using shielded PMT detectors [133]. The main disadvantage of this configuration is that the two images need to be acquired separately and then merged together. The availability of the new generation of photodetectors based on semiconductor materials has allowed the development of PET systems fully integrated inside the MR bore and of PET inserts that can be employed in existing MR facilities. The possibility to employ silicon detectors with ultra-high magnetic fields without worsening the performances has been shown [134]. Large efforts have been invested in the development of a PET/MR scanner; hybrid systems for simultaneous bi-modal acquisitions are now available both for clinical [135] and pre-clinical applications [136]. Figure 28 shows an artistic cross-view of various designs of combined PET/MR systems: (a) tandem: The two scanners are mounted together back-to-back allowing sequential (like PET/CT) rather than simultaneous acquisition, (b) insert: The PET scanner is inserted between the RF-coil and gradient set of the MR system, (c) full integration: the two systems are fully integrated within the same gantry.

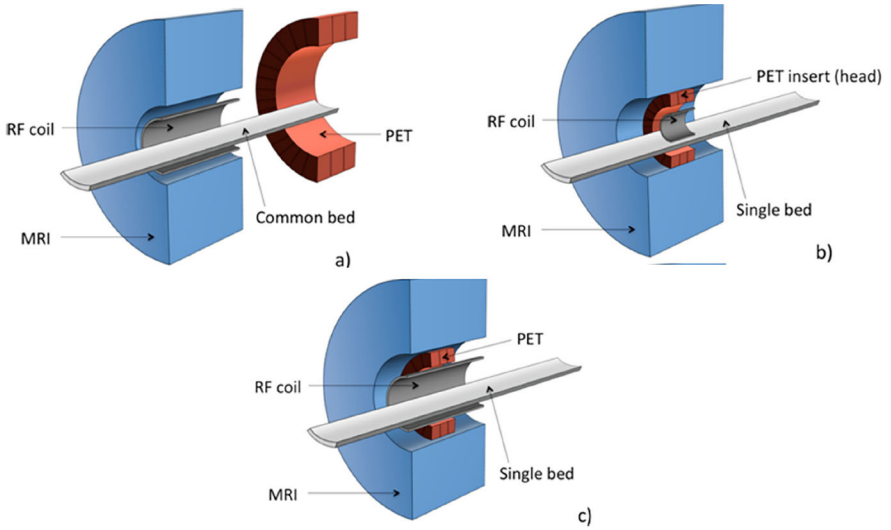

Fig. 28 Artistic cross-view of various designs of combined PET/ MR systems: **a** tandem: The two scanners are mounted together back-to-back allowing sequential (like PET/CT) rather than simultaneous acquisition, **b** insert: The PET scanner is inserted between the RF-coil and gradient set of the MR system, **c** full integration: the two systems are fully integrated within the same gantry [92]

The Siemens mMR whole-body integrated simultaneous PET/MR was the first commercial clinical scanner. The PET detector, based on the previous brainPET technology [137], is composed of 8 rings of 56 detector blocks. The block is composed of 8 × 8 LSO crystals (4 × 4 × 20 mm), coupled to 3 × 3 APDs arrays, for a total of 4032 channels. The PET assembly is installed between the gradient and the body coils of a 3T whole-body MR scanner. The time resolution is 2.93 ns, which prevents the TOF application. Despite the relatively small PET ring diameter (transaxial field-of-view of 59.4 cm), large axial FOV (25.8 cm) and large time coincidence window, the performance of this system in terms of NEC is better than most PET/CT systems, demonstrating that the integration and operation of the PET system in the MR scanner does not impact its performance.

The first commercial PET/MR system based on the SiPM technology has been produced by GE [138]. The PET system with TOF capability [139] has a transversal FOV of 60 cm and an axial one of 25 cm. The PET module thickness is less than 5 cm overall. The detector is based on a Lutetium-based Scintillator, with a similar density of LSO and dimensions $4 \times 5.3 \times 25$ mm. The scintillators are coupled to analogue SiPMs combined with UV transparent light guides for light sharing to reduce the number of readout channels. The MR scanner, based on the GE 3T discovery 750, maintained is full performance after the integration with the PET detectors. The reported specs of the PET system are 10.5% energy resolution and 390 ps FWHM time CTR for the whole system, in the range of the Philips PET/CT based on dSiPMs. The transverse spatial resolution is 4.2 mm and the sensitivity is 22 kcps/MBq (measured with a PET NEMA phantom with the source at the center). Comparable results have been achieved with and without the RF of the MR turned on.

In 2012, the first simultaneous PET/MR device equipped with digital PET detector modules based on digital SiPMs was presented [140, 141]. The main component of this device is the MRI-compatible sensor stack composed on a sensor and interface board. The sensor stack is connected to digital readout electronics to form a Single Detection Module (SDM). Ten of these SDM have been used to build the first simultaneous PET/MR scanner equipped with digital SiPM, called Hyperion IID [142]. It comprises $3 \times 3 \times 10$ detector stacks for a FOV of 96 mm (transaxial) $\times$ 209.6 mm (axial). Based on this architecture, a pre-clinical system (3 rings of LYSO:Ce arrays of 30×30 crystals of $1 \times 1 \times 12$ mm^3 each) and a clinical scanner configuration (1 ring of LYSO:Ce arrays of 8×8 crystals $4 \times 4 \times 10$ mm^3 each) have been characterized in terms of energy, time and spatial resolution. The pre-clinical prototype has an energy resolution of 12.6% and a 3D spatial resolution of 0.73 mm. The time resolution was 260 ps FWHM obtained for a specific trigger configuration. The pre-clinical insert was tested in an MR system by developing dedicated MR sequences [143]. The authors reported degradation of the PET performances of 10% in energy resolution and of 14% in time resolution. They also observed MR SNR degradation and B0 field distortion. Schug et al. [144] assembled and tested a configuration with clinical-like detectors and an updated version of the interface board. The paper reports an energy resolution of 11% and a CRT of 215 ps FWHM and the performance of the PET system were not degraded even under extreme MR conditions.

9.4 Total-body PET

Despite significant advances in PET technology, both in the detector field and in the reconstruction software, the length of the detector cylinder, or axial length, has remained the same for decades. With an axial length of 15–18 cm, only a small fraction of events are acquired [145]. Even with the larger axial extent of last-generation PET systems (20–25 cm), performing whole-body studies requires a series of static scans (from six to eight for an 80 cm whole-body examination) which must be sequentially acquired and combined. This procedure presents major drawbacks. First, the limited extent of the sensitive volume imposes the need for multiple acquisitions, thus prolonging the overall duration of the examination and introducing artifacts in the reconstructed total image. Furthermore, the axial length limits the maximum LOR angle (with respect to the radial direction). As a matter of fact, PET sensitivity increases as the square of the LOR angle, so the system low global efficiency is essentially due to the limited acceptance angle (between 2 and 7 % for a point source placed at the center of the FOV. PET systems with extended axial length would be the ideal solution for addressing present limitations and, at the same time, increasing the scanner sensitivity and the fraction of the patient body seen in one bed position. Ideally, the scanner should be as long as the human body. This PET concept is usually called the "total-body" PET. Although the term total-body PET has been used for such a scanner, strictly speaking, this is only correct for systems with an axial FOV of at least 2 m. To be more general, the name "long axial field of view" (LAFOV) PET seems more appropriate, indicating any scanner with a significantly extended axial FOV (typically longer than 90–100 cm), enabling simultaneous and dynamic acquisitions of all rel-

evant organs or body lesions in a single bed position. LAFOV-PET imaging is not a new idea. Terry Jones proposed the first concept of LAFOV-PET based on dual panel geometry in 1990 at the first IEEE MIC Conference in Washington. Although the idea was never abandoned [146, 147], the cost of the technology and the complexity of the coincidence circuitry with such a large number of detector elements, impeded its practical realization for many years. Furthermore, the extended geometry poses problems from physics and cost. On one hand, the greater the angular coverage, the greater the fraction of random and scattered events as well as the parallax effect. Fast readout electronics and TOF capability are the key elements for this kind of system. On the other hand, the major problem is the cost which in PET is largely determined (about 50% when using LYSO) by the volume of crystal scintillators used. A further technical challenge encountered in the creation of a scanner is the greater complexity of the image reconstruction algorithm [148]. A longer axial extension of the FOV implies first of all a much greater amount of data, as well as a significantly higher data rate, compared to standard clinical scanners, with a number of LORs that depend on the axial extension squared. The calculation of the System Response Matrix (SRM), that typically requires high computational and storage resources, also needs a dedicated strategy, such as the use of factorized components and the exploitation of the high sparsity of the SRM. Furthermore, the greater inclination of the LORs and the increased fraction of random and scattered coincidences make the application of the relevant corrections more critical. Thus, the whole reconstruction process requires the use of large data storage and fast CPUs and/or GPUs which have become available only in the last few years.

Despite the technological difficulties, first prototypes of "total-body" scanners were developed by Siemens Healthineers [149] and by Hamamatsu [150]. The first system (axial length 53 cm) is based on large LSO flat panels arranged to form the sides of a hexagon in constant rotation. This prototype has been tested with two patients. The images showed low resolution and high noise. The second system (axial length of 68.5 cm) consists of 12 layers of block detector rings stacked axially with metal septa to reduce the scatter fraction. Also this system was tested with patients. The authors showed high-resolution images but artifacts due to the movement of the septa are clearly visible. A similar approach is the one followed by the Explorer PET scanner [151], based on modular block detectors of LYSO crystals. The conceptual idea comprised of 40 rings, 48 detectors/ring, for an axial FOV of 215 cm, the longest ever conceived for a PET system. In 2015, the NIH-funded Explorer Consortium was formed to develop this concept. This project has resulted in two TB-PET scanners, both of which have recently demonstrated their potential in human imaging: the uExplorer scanner developed by United Imaging Healthcare (Shanghai, China) in collaboration with the UC Davis team, and the PennPET Explorer scanner developed at the University of Pennsylvania in collaboration with Philips Healthcare (Cleveland, Ohio).

As of today, the uExplorer by United Imaging Healthcare Co. (see Fig. 29, left) is the one and only "total-body" PET/CT scanner available on the market with more than 20 systems in operation, primarily in China and the United States while two systems are being installed in Europe. The present commercial system is based on LYSO matrices and SiPMs and features an axial FOV of 194 cm and 76 cm aperture. The PET is combined with a 160-slice CT. The principal limit to the widespread

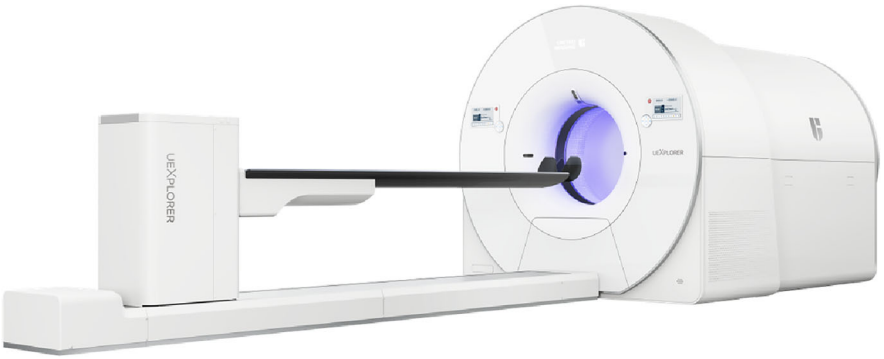

Fig. 29 The "total-body" explorer PET/CT produced by united imaging healthcare

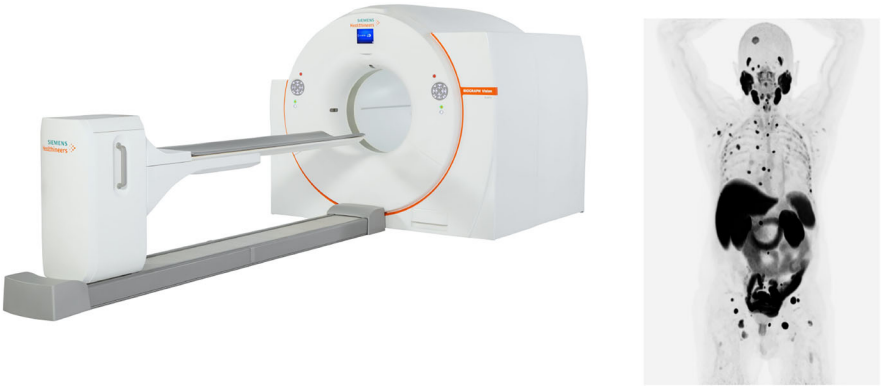

Fig. 30 Left: picture of the Biograph Vision Quadra by Siemens Healthineers. Right: PET image of the head and torso of a patient taken in a single bed position with the Biograph Vision Quadra . Image courtesy of Siemens Healthineers

adoption of this kind of system is the high cost that makes it unaffordable for most hospitals, even in high-income countries [152]. Driven by the necessity to reach a more sustainable performance-to-cost ratio, manufacturers have now launched on the market LAFOV-PET/CT scanners without reaching the true "total-body" coverage. Today, a popular example is the Biograph Vision Quadra by Siemens Healthineers. With a 106 cm axial FOV, it can image the whole torso in one bed position [153] as shown in Fig. 30.

The most direct advantage of a LAFOV-PET is the substantial increase in sensitivity, especially when visualizing the whole body. In fact, considering that the sensitivity for a point-like source is proportional to the solid angle covered by the scanner's detectors when locating the source at the center of the field-of-view in a cylindrical scanner, the sensitivity is maximum and proportional to $4\pi \sin\theta$ where θ is the maximum inclination of the possible LOF with respect to the direct planes ($\theta = 0$). This means that, for short axial FOV scanners the sensitivity varies linearly with the FOV length, but as soon as the axial FOV becomes comparable to the scanner radius it rapidly converges to the maximum. For example, with a 50 cm long-axial FOV, the geometrical coverage

is about 50% and is already 80% with a length of 1 m [154]. This point-source example mimics the sensitivity behavior of single-organ imaging. Furthermore, one has to consider the efficiency reduction induced by the attenuation in the body (especially for very inclined LOF's) which limits the sensitivity gain for single-organ imaging to a factor of 3–4 with respect to standard 20–25 cm axial FOV PET/CT scanners. This gain is nearly stable beyond a scanner length of about 70–80 cm. This fact demonstrates a substantial equivalence of 1 m and 2 m long scanners for applications in which a single hot spot or organ has to be visualized. Conversely, for long objects (like a full body), the above-reported point-source sensitivity must be integrated over the whole extent of the object, leading to a nearly quadratic dependence of the sensitivity with the axial FOV length. In this way, a gain factor of 10–40 can be observed in long-axial FOV systems [154].

The increment in sensitivity has several immediate practical advantages. On the one hand, the higher sensitivity can be used to obtain an image of the same quality as a 20-min scan in a time of one order of magnitude shorter permitting to scan more patients in the same time period, e.g., in a single working day. Indeed, the patient turnover (including entering/exiting the room and patient positioning time) limit the maximum number of patient per hour to 6–8, but still significantly higher than usual. The shorter acquisition time could be also beneficial for those patients who have difficulties keeping the still position for a long time. On the other hand, the higher sensitivity can be exploited to obtain an appreciable reduction in injected dose, leading to new clinical indications and research possibilities, including the use of new PET radiotracers and new uses for conventional ones that were previously unviable due to efficiency issues. For example, the dose can be lower to an extent for which PET/CT can be applied for the screening of high-risk populations, for pediatric patients who often show a diffuse pattern of involvement which requires whole-body scanning or even for maternal-fetal imaging which has normally no application in humans because of concerns over the effects of radiation on the fetus. These aspects would become even more interesting if one can rid of the CT scan as possibly allowed in the future generating synthetic CT with PET images and/or Lutetium background transmission scans with artificial intelligence (see Sect. 9.8). Another paradigm in which high sensitivity is generally a prerequisite is imaging studies designed to track the fate of cells [155] or nanoparticles in vivo. Radiolabeling these entities renders them visible, but with current PET scanners, they can be followed for only a relatively short time. Total-body PET has the potential to allow lower numbers of cells and particles to be detected, and after an injection of cells or particles labeled with a long-lived positron emitter such as ^{89}Zr (half-life, 3.3 days), it may be possible to follow their fate in vivo for weeks or even a month.

One of the early results that shocked researchers in the field, was the first human dynamic image [156] obtained with the uExplorer PET/CT that showed the FDG propagation in the body over 1 h after injection with a clarity never seen before. Thanks to the whole-body high sensitivity, the feasibility of dynamic imaging with frame durations down to 100 ms was also demonstrated [157] enabling the study of fast radiotracer dynamics. Dynamic scans are also the key element for achieving true parametric (or quantitative) PET which is crucial to ensure the full clinical value of

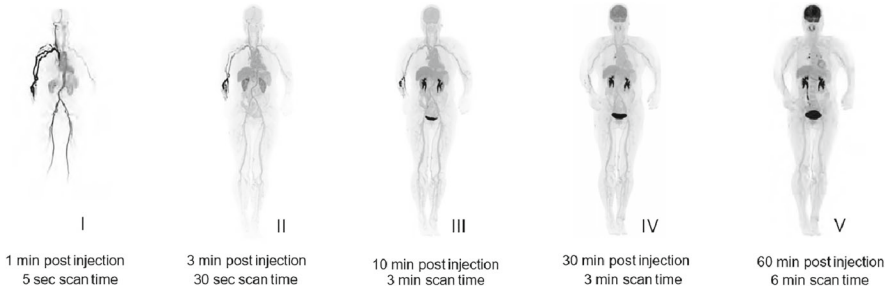

Fig. 31 Total-body dynamic imaging in one bed position obtained with the uExplorer . Image courtesy of Zhongshan Hospital

molecular imaging in all its main application fields [158]. An example of true total-body dynamic imaging obtained with the uExplorer is shown in Fig. 31.

Quantitative biomarkers can be obtained by exploiting the pharmacokinetic information from dynamic PET scans [159]. Pharmacokinetics allows more accurate modeling and quantification of radiotracer delivery and heterogeneity in a given tumor or tissue type and variations in radiotracer diffusion in different tissues (too fast/slow, too early/late). It also allows explaining the complex spatio-temporal evolution of neurotransmission, thus providing information on the onset and progression of disease well beyond the traditional semi-quantitative approach. Pharmacokinetics requires estimating the time-dependent concentration of radiotracer in the arterial blood plasma, which is commonly known as the input function (IF). The standard procedure for IF measurement requires blood sampling during the PET acquisition: this is done invasively and requires arterial cannulation to sample specific quantities at precise times and several corrections and approximations are typically necessary. A different and non-invasive approach is the derivation of the input function from PET images. This is referred to as image-derived input function or IDIF [160]: the activity over time in the plasma is estimated from a blood vessel's images at different time frames. Most importantly, IDIF is possible only for those scanners that have a field-of-view (FOV) large enough to acquire the site of interest, e.g., the brain, and a major blood vessel simultaneously. Early results obtained with the uExplorer have shown the potential of IDIF for brain studies using the concentration acquired from the aorta or left ventricle [157]. However, despite the high sensitivity of the PET scanner, the slow kinetics of ^{18}F-FDG imposes a scanning time of at least 45–60 min to generate whole-body parametric PET images, e.g., using the Patlak model [161]. The main problem is the long scan which is necessary to derive the full input function to be used in the Patlak model. Indeed, recent studies have demonstrated that using a population-averaged input function, normalized to the specific patient using late dynamics only, is it possible to scan the patient between 40 min and 60 min post-injection obtaining results similar to those obtainable with to full 60 min scanning time. Encouraging results using this method have been obtained both with the Biograph Vision Quadra [162] and with the uExplorer [163]. Alternative approaches based on artificial intelligence in combination with LAFOV PET data have been also studied to reconstruct high-quality direct Patlak Ki images

directly from a few consecutive sinograms without the need for an explicit derivation of the input function [164].

The capability to enable full kinetic PET investigations is probably the most powerful and game-changing abilities of total-body PET scanners, with a real potential to finally transform clinical PET from a semi-quantitative into a true quantitative imaging modality reinforcing the PET role towards a true personalized medicine.

The above-mentioned ability to determine the pharmacokinetics of all the organs and tissues can be also applied to study new drugs, therapeutic agents or new imaging radiotracer and speed up their development and translation to humans.

Although clinical oncology remains the main field of application for LAFOV PET with significant advantages with respect to standard whole-body PET/CT [165], another exciting field of applications where the widespread use of LAFOV-PET scanners can have a significant impact is the study of the so-called "organ axes" [166]. The human body is a complex network in which the organs represent the nodes. Each organ displays its how features and functioning. Many diseases first appear as a single-organ malfunctioning and, even in complex disorders, the treatment is often made according to this very limited perspective. In fact, each organ constantly interacts with the others through feedback mechanisms which may occur on different time scales. The regulating process is oriented toward the preservation of physiological homeostasis. When an organ is subject to malfunctioning, its connections can cause a more generalized dysfunction involving other organs or even the entire body. Examples are inflammation in response to infection or tissue damage as a response of the system to restore the original homeostatic state. In this perspective, LAFOV-PET can contribute to the visualization of this whole-body metabolic connectivity framework [167, 168] and some peculiar organ-to-organ interconnections or "organ axes" for its capability to dynamically and simultaneously visualize multiple organs in a single bed position. As an example, the gut-brain axis is a well-known connection in neuroscience. One of the possible connections between the two organs is the effect on the brain of the bacteria in the gut and the link with a whole family of disorders is under investigation [169]. Moreover, recent studies have found evidence of how gut-resident bacteria of the gastrointestinal tract, regulate and influence cognitive dysfunctions [170]. In this field, LAFOV-PET scanners can contribute to the elucidation of the underlying mechanism by providing dynamic images of the immune system, e.g., tracking immune cells of the gut and their interaction with adjacent as well as distant organs [166].

9.5 Organ-specific PET systems

During the past years, PET systems dedicated to the imaging of particular organs have been proposed [171, 172], for instance, imaging of the brain, breast, prostate and extremities. The requirement for the invention of new special systems stemmed from the inadequacies of whole-body PET systems in terms of spatial resolution and sensitivity. The diminished spatial resolution is mainly caused by the acollinearity effect for a detector separation of 80–100 cm (see Sect. 5.5). In addition, the detection efficiency is very limited in whole-body systems. As a result, PET systems are unable to detect lesions with uptake lower than 10 mm. Organ-specific PET systems, such

as pre-clinical ones, can have an improved spatial resolution and a higher sensitivity to detect finer details in the images.

PET has been instrumental in supplying unique information about the human brain that has been applied to a range of research projects from basic neuroscience to clinical applications. Dedicated brain PET systems were catalyzed by the requirement for superior performance compared to whole-body scanner, particularly greater spatial resolution or higher sensitivity to image small brain structures [173]. Not only was better performance sought, but much effort was put into elevating the portability, mobility, or wearability of the device. In addition, the smaller total size made integration with MRI scanners simpler, leading to the development of MR-compatible PET inserts. One of the first examples of organ dedicated system was the HRRT system designed for the imaging of the brain [174]. It consists of eight high-resolution panel detectors arranged in an octagon. The detector separation is 46.9 cm and the FOV is 31.2 cm wide and 25.2 cm long. The detectors have DOI resolution capability with a resolution of 7.5 mm (with two detector layers of 5 mm each). The spatial resolution is 2.5 mm across the whole FOV. To allow the subjects to be scanned standing or moving, other compact solutions were proposed like the NeuroLF [175] or the wearable Helmet-PET [176], the ambulatory microdose PET concept [177] and the upright wearable PET imager [178]. The first simultaneous human brain PET/MR system was presented in 2007 as a PET insert in the bore of a Siemens 3T MAGNETOM Trio MRI scanner [137, 179]. The Siemens brainPET insert (see Fig. 32), produced in a limited number of samples, was based on the same LSO/APD technology pioneered by the Tubingen group for the small animal PET insert and later on successfully applied to the whole body Siemens PET/MR scanner. The brainPET insert is composed of 32 modules each one comprising LSO arrays (12×12 pixels of $2.5 \times 2.5 \times 20$ mm^3 crystals) coupled to a 3×3 array of 5×5 mm^2 APDs. The detectors and Front-End electronics are air-cooled and contained in 32 copper-shielded cassettes and the insert is placed inside the MR body coil, which is disabled when the PET system is in place. A dedicated head coil is placed in the FOV of the PET system. The small diameter (37.6 cm) and a relatively long-axial extent (19.1 cm) result in a very high sensitivity of 7% that combined with a spatial resolution as low as 3 mm FWHM provides excellent image quality. Furthermore, the ability to perform functional studies in MR (fMRI) and proton spectroscopy was demonstrated [180]. Other brain PET inserts developed in the framework of research projects [181, 182] demonstrated the substantial progress made in the field of dedicated brain PET instrumentation. However, sustained effort is still needed to move from promising concepts to specialized products that can broaden our understanding of the human brain and, ultimately, address the many unmet clinical needs in neurology and psychiatry.

Breast imaging with positron-emitting tracers is usually called Positron Emission Mammography (PEM). Several systems have been proposed but in general, they can be grouped into two categories: partial and fully tomographic systems [183]. A partial tomographic system is generally composed of two flat detectors used for imaging the breast in a geometry similar to X-ray mammography [184]. The breast is mildly compressed between the two detectors and imaged to match the mammography. As a result of the limited angular sampling, the spatial resolution is not isotropic but overall the spatial resolution is superior to whole-body PET systems and a significantly better

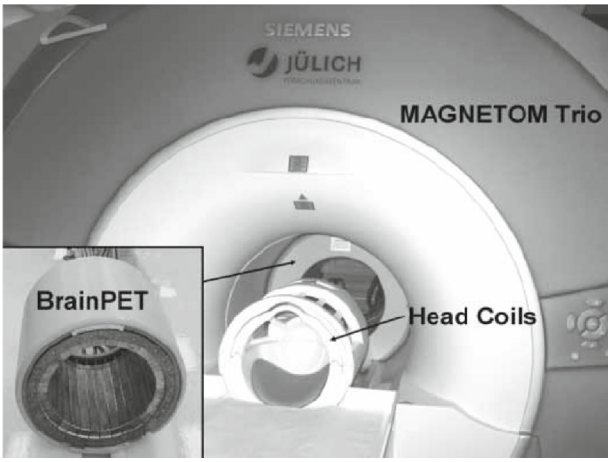

Fig. 32 The BrainPET insert in the MAGNETOM Trio MRI and also separately with removed inner cover [179]

sensitivity for sub-centimeter lesions has been observed. The first commercial system approved by the US Food and Drug Administration (FDA) was the Flex Solo II from CMR-Naviscan [185]. The system in-plane resolution is about 2.4 mm. In the group of fully tomographic systems, a commercially available system is the MAMmography with Molecular Imaging (MAMMI, Oncovision, Valencia, Spain) [186, 187] where the patient breast is imaged in a prone position as shown in Fig. 33A and B. This system is based on monolithic LYSO crystals coupled to position-sensitive PMTs and arranged in a full ring of detectors (Fig. 33C, D). The spatial resolution is 1.6 mm. A meta-analysis conducted on 873 breast lesions showed a sensitivity of 85% and a specificity of 79% on a lesion basis, using ^{18}F-FDG with PEM in women with suspected breast malignancies. A dedicated breast PET (dbPET) with a photomultiplier tube (PMT)-based detector (ElmammoTM; Shimadzu Corp., Kyoto, Japan) was developed, and this system was shown to achieve higher spatial resolution than whole-body PET/CT by using a highly photon-sensitive detector placed close to the breast and scanning with reduced respiratory motion [188]. A newly developed organ-specific PET device (BresTome from Shimadzu Corp, Japan) is a SiPM based TOFPET scanner that can switch the position of a cylindrical detector into two imaging positions, one for the head and one for the breast. Recent studies have evaluated the image quality provided by this scanner as a head and breast PET [189].

Dedicated prototypal systems have been also developed for prostate imaging. This organ is a challenge to imaging with conventional whole-body PET systems due to low tracer uptake in the organ and high uptake in the bladder. Prototype systems with higher sensitivity than clinical ones have been developed. Some of them were conceptually similar to breast devices in the sense they had a smaller detector separation to increase efficiency [190]. An alternative approach is the one proposed in the EndoTOFPET-US project [191, 192]. One of the two PET detectors is a scintillator array coupled to a SiPM array integrated in an endoscopic probe. This allows minimizing the distance between the region of interest and the detector, thus increasing the sensitivity. The

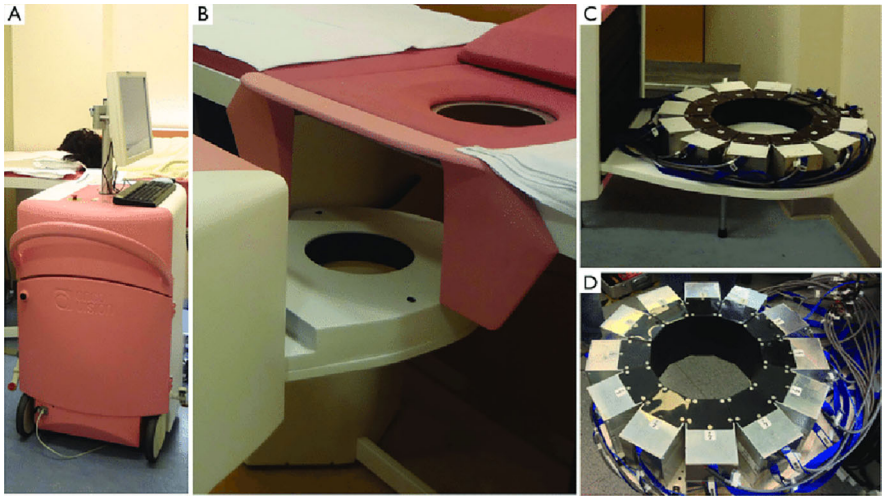

Fig. 33 MAMMI-PET system for breast imaging with patient in prone position (**A**) hanging breast thanks to the special bed and ring camera (**B**). Internal view of the scanner version with a single (**C**) and a double (**D**) full ring of detectors . Reproduced from [187]

miniaturized detector installed in the endoscopic probe is composed of an array of $0.7 \times 0.7 \times 10$ mm^3 LYSO crystals optically coupled to a digital SiPM array, while the external detector plate is composed of $3 \times 3 \times 15$ mm^3 scintillators readout by analog SiPMs. The asymmetric configuration of the detectors, with the probe very close to the region of interest, requires a high time resolution to employ TOF in the reconstruction algorithm so as to remove the background of the surrounding tissue. Despite its benefits, there are no commercial PET systems dedicated to the prostate. Further improvements in instrumentation are required to introduce them in the market [193].

9.6 Ultra-fast timing PET

As already illustrated in Sect. 7.5, the introduction of the time-of-flight PET concept has a beneficial effect on image noise, which can be exploited not only for improving, e.g., lesion detectability, but also for reducing the examination time or the patient dose or for aiding the image reconstruction process in the presence of inconsistent or missing data. This could be of great importance in scanners characterized by an incomplete angular coverage like, e.g., scanners for PET monitoring in particle therapy (see Sect. 9.7) or total-body scanners with flat-panel geometry [194]. Although some indirect improvement in spatial resolution can be observed [195], the size of the tube-of-response along the direction of flight of the γ-rays ($\sigma_{\parallel}$) is still much larger than its transversal size ($\sigma_{\perp}$) which is limited by crystal width, photon non-collinearity, positron range, detector coding and parallax effects (see Sect. 5.5). Thus, $\sigma_{\perp}$ still remains the limiting factor for the maximum achievable spatial resolution. However, it has been recently suggested that, in the regime where $\sigma_{\parallel} \leq \sigma_{\perp}$, TOF information enables PET imaging with resolutions below this fundamental limit [196].

Taking into account the speed of light (≈30 cm/ns), a CTR in the 10–20 ps (FWHM) range, corresponding to a $\sigma_{\parallel}$ equal to 1.5–3.0 mm, would be necessary to achieve the objective. Such small confinement could suggest the possibility of avoiding the reconstruction step leading to the so-called "reconstruction-free (or direct) PET imaging" [197]. Although this attractive modality is in principle possible in the absence of scattered coincidences [198], the noise and spatial resolution of the images that can be achieved could be sub-optimal compared to images reconstructed via advanced iterative algorithms. Furthermore, the road to the full exploitation of such extreme TOFPET information is still not well defined. In fact, it may happen that the standard iterative reconstruction approach is not yet the best one when quasi-perfect TOF information is available. In the future, the introduction of artificial intelligence-based approaches and more accurate physical modeling of the emission detection processes may change the PET image formation paradigm, but a sort of image reconstruction process is expected to remain a fundamental step in PET imaging. Furthermore, with a CTR of 10 ps the SNR gain would be around 16× for a 40 cm diameter object and therefore comparable with that of a total-body PET scanner, thus making ultra-fast timing PET extremely attractive from this point of view.

The unceasing progress, as well as the introduction of novel materials, in the sub-components of the whole detection chain, is contributing to the continuous improvement in TOFPET performance [199]. Using sophisticated setups obtaining a CTR in the 70 ps range seems today possible. However, most of the solutions providing ultra-fast timing performance can be hardly transferable to real medical devices for the use of non-scalable bulky electronics or devices ultimately showing a very low sensitivity (e.g., due to thin scintillators or reduced geometrical efficiency). Thus, the real-world implementation of ultra-fast timing detectors, which must also show other features such as high sensitivity, a small dead area, a good count rate performance as well as a high reliability, requires a number of innovations that involve the whole detection chain, including the scintillator, the photodetector, and the readout electronics as well as a higher level of technology integration. Here below, some of the most promising technologies for developing ultra-fast timing TOFPET components are reported.

Scintillators Although silicon-based solid-state detectors have been proposed in last years for TOFPET applications, scintillators are still the key components of a TOFPET detector for their ease of use, performance-to-cost ratio and scalability. Indeed, they remain one of the major limitations for reaching ultra-fast timing performance. In fact, our capability in extracting the time information from a scintillator depends on the dynamics of the scintillation light pulse, which is characterized by a certain rise time τ_r, a decay time τ_d and a light yield (LY). The effect of τ_r is to delay the emission of the first produced photons and then to increase their time jitter and to reduce the time resolution of the scintillator. The scintillator scintillation decay time τ_d also affects the CTR that can be achieved with a scintillator. In fact, the higher the impulse, the better our ability to determine the time of the interaction (e.g., with a fixed threshold discriminator). Then, for a given light yield, the decay time linearly contributes to broadening in time the light pulse, ultimately reducing the actual height of the pulse. In general, the contribution of the scintillator parameters to the CTR can be summarized according to the following formula:

$$\mathrm{CTR} \propto \sqrt{\frac{\tau_r \cdot \tau_d}{LY}}.$$

Considering that LYSO, has a light yield of 40,000 ph/MeV, a τ_r of 70 ps and a τ_d of 40 ps, it is clear how the best achievable CTR using the material which is today still considered the best for PET can hardly be better than 100 ps. Even if new inorganic scintillator materials and doping elements are continuously proposed, due to the intrinsic mechanism of scintillation it is unlikely that a CTR in the 10–20 ps range can be achieved with these materials [200]. A possible way to overcome this limitation is the production of a small number of prompt photons by means of different scintillation mechanisms such as hot intraband luminescence, organic scintillation or nanocrystals [199]. The idea of creating a sort of heterostructure which combines a standard scintillator with a material producing prompt photons is at the base of the concept of metacrystal [201]. For example, thin layers of LYSO or BGO can be interleaved with layers of faster inorganic materials (such as BaF_2), plastic scintillators, or polystyrene with embedded nanocrystals. Although the γ-ray can interact either in one or the other material, the recoil electron could have enough energy to travel in both, thus always creating a fraction of prompt light photons. Although encouraging results are already reported in the literature, the production cost and the reduction in density with respect to the bulk material remain a challenge for the adoption of metascintillators in PET systems.

Cherenkov PET Another possible source of prompt photons is the Cherenkov emission and the PET concept exploiting this effect is typically called the Cherenkov PET. The general working principle is shown in Fig. 34. The 511 keV photons produced in the annihilation of the positron emitted by the β^+ source reach the Cherenkov radiators, interact in their volume and the secondary photoelectrons and Compton electrons that have a velocity greater than the speed of light (c/n) in the radiator emit Cherenkov radiation (CR). If the radiators are transparent, the CR can be detected by the photodetectors coupled with them. The arrival time of the Cherenkov photons in a determined coincidence time window can be used to limit the range of possible positions on the LOR for the annihilation event. Contrary to the delayed scintillation light, the CR is emitted promptly, therefore the time resolution in Cherenkov TOFPET is limited only by the spread in the optical photon path in the radiator (due to the different distance between the production point and the photodetector) and by the photodetector time performances.

The first proposal of Cherenkov TOFPET suggested to use silica aerogel with refractive index n of 1.2 as a Cherenkov radiator [202]. In fact, this material is transparent to the visible CR and the value of the refractive index allows detecting only photopeak events by automatically discarding the Compton ones. For a photoelectron (arising from the photoelectric interaction of a 511 keV photon in the radiator) an index of refraction of 1.156 is sufficient to produce CR, while a Compton electron (with energy $E \leq 341$ keV) needs at least an n of 1.25 for the Cherenkov effect to take place. This first study suggested also the use of fast multi-channel plate photomultiplier tubes (MCP PMTs) as photodetectors coupled with the silica aerogel to further improve the TOFPET time resolution. Subsequent studies suggest the use of scintillators with high refractive index, high visible light transmission properties, high density and high

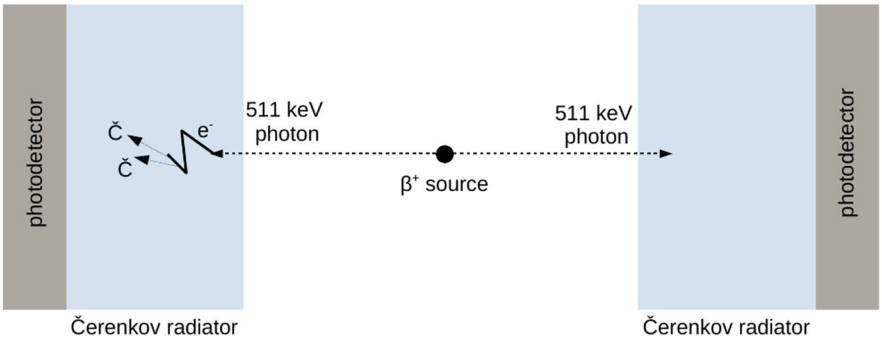

Fig. 34 General working principle of the Cherenkov PET

effective atomic number coupled with MCP PMTs. In [203], a system with cylindrical symmetry was used, obtaining an FWHM time resolution of 1.2 ns in BaF_2 and of 170 ps in lead glass. In [204], PbF_2 and PWO crystals were used in the back-to-back layout of Fig. 34. Crystals of 5 and 15 mm thickness were tested, and different surface treatments (Teflon wrapping and painted black surfaces) were evaluated. The best time resolution (σ of 68 ps) was obtained with the 5 mm thick PbF_2 crystal with painted black surfaces. In [205], the time resolution of PbF_2 was strongly improved (σ of 30 ps) for the 5 mm thick crystal with painted black surfaces and the performances of $PbWO_4$ were simulated and validated against those of PbF_2, indicating worse time performances than PbF_2 (less transmission, optical photons with lower speed due to the higher refractive index and scintillation background). Pestotnik in [206] explores the use of PbF_2 in combination with SiPMs for TOFPET. The conclusions are an efficiency comparable to LSO-based detectors but SiPMs need further improvements in timing and front-end electronics to achieve sufficient time resolution.

Simulations in [207] studied the Cherenkov TOFPET timing performances of LSO:Ce scintillators of thickness ranging from 1 to 30 mm, giving a FWHM comprised between 12 and 125 ps. The study also showed how the information on the light output and arrival time distribution can be used to improve time resolution (from a σ of 39–30 ps), and how the DOI estimation could improve it further. In [208], the simulation study was extended to other inorganic scintillators (LuAg:Ce, BGO, PWO and lead glass). It was concluded that, being Cherenkov photon yield rather low, CR is very challenging to be used in PET since energy determination and Compton events discrimination are difficult to perform. Yet, the CR can be exploited in combination with scintillation to achieve a sufficient energy resolution. In [209], the authors investigate the potential of BGO as a cost-effective, hybrid scintillator/Cherenkov radiator for TOFPET. The results suggested the feasibility to combine event timing based on Cherenkov emission with energy discrimination based scintillation in BGO.

Photodetectors and readout electronics As of today, SiPMs (see Sect. 9.1) still remain the preferred choice for the development of TOFPET detectors. In fact, thanks to their intrinsic properties and in particular to the high photon detection efficiency (PDE) (which includes the QE and the fill factor of the design in silicon) the contribution of the SiPMs to the CTR is not the limiting factor, at least using the scintillating

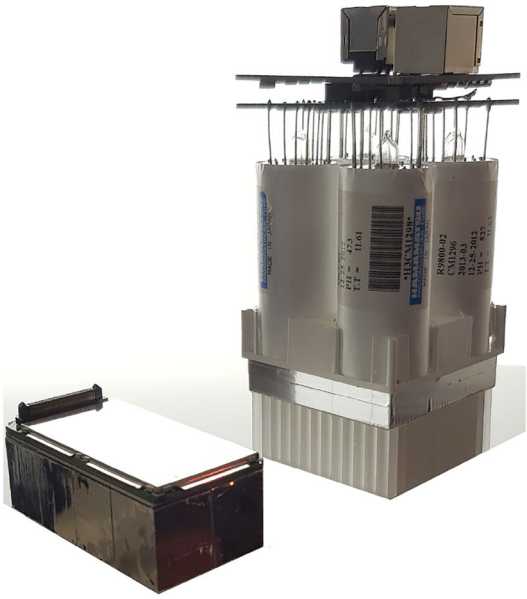

Fig. 35 Picture showing the comparison between a traditional block detector (right) and a SiPM based detector for clinical PET. Both detectors are manufactured by Siemens Healthineers and are featured in different generations of commercial products

materials available today. Their flexibility in terms of detector design choices (SiPMs are available both in the form of matrices and single-pixel elements) and in terms of compatibility with several readout strategies have represented a winning factor leading to the fact that in almost all modern PET scanners SiPM based solutions have replaced the PMT-based block detector (Fig. 35). As a matter of fact, the indeed promising digital SiPM concept has been progressively abandoned for its complexity and the limited possibility of customization with respect to analog SiPMs. The readout electronic is also a key factor for reaching ultra-fast timing performance. Although solutions based on discrete components provide state-of-the-art timing performance [210], they are typically used during the development of new devices or implemented in demonstrator prototypes, only. They do not represent the optimal choice when the density of readout channels is high, such as those necessary when single channel readout, i.e., without any channel multiplexing (e.g., row/column readout) is required.

The need for high channel density data acquisition systems encouraged the recent development of several application-specific integrated circuits (ASICs) dedicated to the readout of matrices of SiPMs while still preserving the high time resolution. These devices can be classified into two main families: mixed-mode and fully analog circuits. The first type of ASIC includes both the analog, i.e., the front-end part and the digitization part. The advantage of this solution consists in the completeness of their capability at the expense of increased complexity and reduced flexibility. Examples of recent mixed-mode ASICs for SiPM readout are: the TOFPET2 [211] and the PETA6-SE [212]. Conversely, the fully analog ASICs rely on external ADCs or TDCs for the digitization of their outputs. An example of these ASICs is the HRFlexToT, developed by the University of Barcelona [213], which is a 16-channel ASIC in which the energy and the timing information are encoded into two consecutive digital pulses. By means

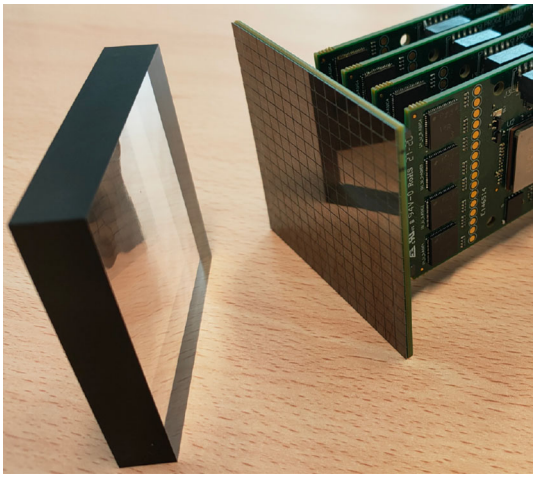

Fig. 36 Picture of the UTOFPET detector developed by the University of Pisa. The detector is based on a 67.2 mm × 67.2 mm LYSO monolithic block and coupled to 4.2 mm pitch SiPM by Broadcom arranged on 16 × 16 matrix. The 256 SiPMs are read out by sixteen 16-channel FlexToTHR ASICs hosted on four readout boards, which are visible to the right side of the picture. Each readout board has an FPGA for the readout of four ASICs via TDCs

of external TDCs (either in the form of dedicated IC or implemented in FPGA [214]) the timestamp and energy of the output of each single SiPM can be decoded. A more recent version of this ASIC is the 8-channel FastIC [215]. A picture of a PET detector based on a monolithic scintillator coupled to a 16 × 16 matrix of SiPMs and read out by mixed-mode ASICs is shown in Fig. 36.

With the future development of novel materials potentially offering the possibility to approach 20 ps CTR, the present ASIC technology could be not adequate to exploit in full the superior timing performance. Hence, new strategies based, e.g., on 3D and 2.5D (i.e., by means of through silicon vias) integration of the photosensor with the readout electronics might represent a necessary step for future ultra-fast timing PET detectors [216].

9.7 PET monitoring in particle therapy

Particle therapy or hadrontherapy deploys ions (usually protons and carbon ions) to treat radioresistant and solid tumors [217]. Robert Wilson in 1946 proposed the usage of the depth dose curve of charged particles, which had a peak (known as the Bragg Peak) at the end of the range, for the treatment of deep-seated tumors through cancer therapy [218]. In comparison to conventional radiotherapy, the integral dose (total energy released within the tissue) for any given target dose is always lower as the entrance and exit doses are minimized. In addition, the sharp dose gradients facilitate a more accurate definition of the target area appropriate for treating tumors close to critical organs (e.g., skull base chondrosarcomas situated near the spinal cord) [219]. Despite this, particle therapy is more vulnerable to inaccuracies than conventional radiotherapy and the consequences of an erroneous quantification can be more serious. Dose computation inaccuracies, calibration errors and imaging artifacts in the treatment planning, coupled with issues in the treatment delivery (organ motion, anatomical/morphological changes, patient setup) are all sources of uncertainty [220]. As a precautionary measure, a conservative margin of safety is included in the treatment

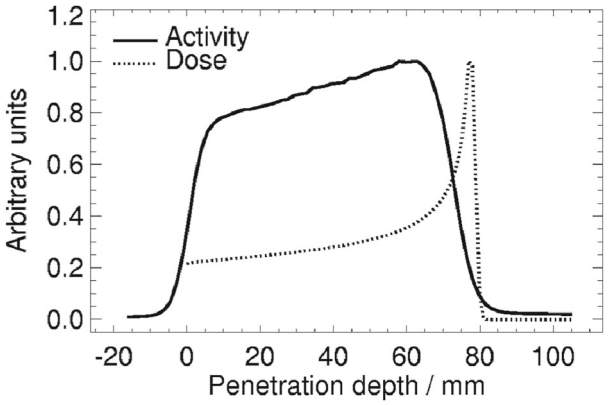

Fig. 37 Calculated depth dose distribution (dotted line) and corresponding activity profiles (solid line) for a homogeneous polymethyl methacrylate (PMMA) target irradiated with a 110 MeV proton beam[224]

plan to cover any potential range discrepancies. As an example, in proton treatments an allowance of 3.5% of the range plus an additional 1–3 mm are taken into consideration [221]. The in vivo range verification systems provide confirmation of the planned treatment by allowing the accuracy of beam delivery to be checked. This is usually done through the detection of secondary radiation exiting the patient after nuclear reactions along the beam path [222]. Nuclear reactions keep occurring until close to the Bragg peak region when the kinetic energy goes beneath the Coulomb barrier. This suggests that the secondary radiation emission is connected to the primary ion range, even though the nuclear processes are not the same as the electromagnetic interactions determining dose deposition. PET is the most consolidated and clinically investigated in vivo verification technique [223]. The difference with PET in nuclear medicine is that the positron is emitted in the decay of a radioisotope created by the interaction of the primary beam with the tissue. Protons and light ions ($Z \leq 4$) produce positron-emitting target nuclei such as ^{11}C, ^{15}O, ^{13}N with half-lives of about 20, 2 and 10 min, respectively. The activation occurs as long as the beam energy is above the nuclear reaction threshold that typically corresponds to 1–4 mm of residual range of the primaries in tissue. Figure 37 shows the calculated depth dose distribution (dotted line) and the activation profile in a homogeneous polymethyl methacrylate (PMMA) target (solid line) produced by 110 MeV protons showing a slow rise followed by an abrupt distal fall-off a few mm's before the Bragg peak.

On top of the beta-activated target nuclei, heavier ions ($Z \geq 5$) can also yield positron-emitting projectile fragments when they stop, near the end of their range. For instance, for ^{12}C beams, the activity is mainly due to ^{11}C and, to a lesser extent, to the short-lived ^{10}C ($T_{1/2} = 20s$). Both radionuclides accumulate shortly before the ^{12}C Bragg peak. PET imaging in particle therapy monitoring is primarily applied to estimate the range of the primary particles penetrating the tissues, not the dose since induced activity and dose delivery are based on different physical processes. Despite this, one can still determine whether the dose administered to the patient met the expectations by comparing the acquired PET image with a reference Monte Carlo

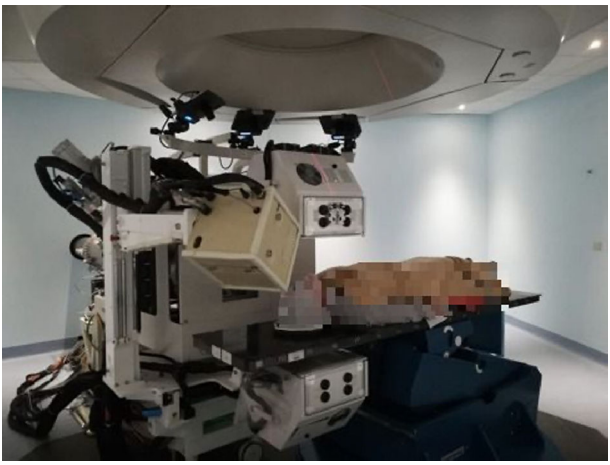

Fig. 38 The INSIDE system at CNAO Pavia, Italy

simulation or an analytical model, to test the accuracy, or with a PET image acquired during the first day to test the reproducibility among fractions of the same treatment. During the last 25 years, PET as range monitoring has been extensively investigated and is now a recognized, albeit not generally used, approach. The reduced signal levels it produces and physiological washout are the main issues hampering its widespread clinical use. In fact, the activity formed in nuclear interactions (a few (kBq/ml)/Gy) is almost two orders of magnitude below the typical activity concentrations in nuclear medicine (order of 50 kBq/ml in hot spots). In addition, the induced activity is rapidly lost due to the physical decay of the sources (the main isotopes produced, ^{15}O and ^{11}C, have half-lives of 2 min and 20 min, respectively) and to the physiological washout in which isotopes created bond to different molecules and travel along functional pathways like diffusion and perfusion [223].

After the first pioneering experience with He beams 50 years ago at the Lawrence Berkeley National Laboratory [225], a more extensive clinical study was performed at the horizontal beamline of the GSI Helmholtzzentrum für Schwerionen Forschung in Darmstadt, Germany. Here a commercial PET scanner based on BGO crystals was modified in a dual head camera to be adapted at the beam nozzle [226]. Between 1997 and 2008, Carbon ion treatment of over 400 patients with head and neck and pelvis tumors was successfully monitored via PET scanner. At the National Cancer Center Hospital East in Kashiwa, Japan, a beam online planar PET system [227] was mounted on a rotating gantry for dose-volume delivery-guided proton therapy. Activity measurements were performed in patients with head and neck tumors, liver, lungs, prostate, and brain. The comparison between the reference activity image (acquired at the first fraction) and the daily activity images revealed modifications in the proton-irradiated volume.

More recently the INSIDE system started a clinical trial at the National Center of Oncological Hadrontherapy (CNAO) in Pavia, Italy (see Fig. 38). INSIDE is a bi-modal system composed of a charged particle tracker (named Dose Profiler) for the detection

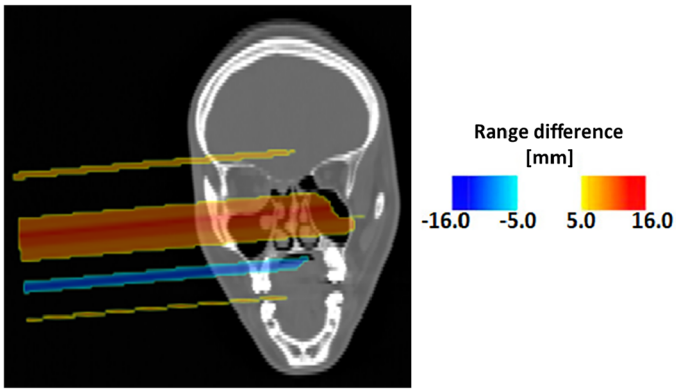

Fig. 39 Color map referring to a patient treated with protons at CNAO and monitored with the INSIDE in-beam PET showing a morphological variation during the course of the therapy. The map is overlaid on the planning CT and the LUT of the range difference is shown on the right

of nuclear fragments emitted by the fragmentation of the primary ^{12}C ions in the tissues, and of an in-beam PET, a dual head systems based on LFS crystals and SiPMs [228]. The INSIDE trial enrolled 20 patients with head and neck and brain issues that were treated using either protons or carbon ions. The activity PET images acquired during different fractions were analyzed with a robust approach based on a multi-threshold procedure to detect possible range deviations [229, 230]. Figure 39 shows the colored map of the significant areas where a deviation between the reference and the actual range was found, superimposed to the patient CT acquired for the treatment planning. The purpose was to assist the radio-oncologist in assessing patient morphological changes with a control CT. Reproducibility tests showed that a precision of 4 mm in the range determination was achieved in patients treated with protons.

In-room solutions have been clinically explored for passive scattering proton therapy at the Massachusetts General Hospital [231], where a prototype PET scanner was positioned next to the treatment head after treatment. Off-line PET/CT-based treatment verification was clinically explored at the Heidelberg Ion Beam Therapy Centre (HIT) with actively scanned proton and Carbon ion beams [232, 233]. A commercial full-ring PET/CT scanner installed in close vicinity to the treatment rooms was used to image the patients after selected irradiation fractions. Head, head/neck, liver and pelvic tumors were monitored. Quantitative range analysis showed that accuracy was 1–5 mm for most examined cases due to the limitations of the physical prediction and washout model. Clinical studies with off-line PET/CT were also reported by Hyogo facility [234] and Florida Proton Therapy Institute [235]. Particularly, the latter one conducted systematic analyses of proton-activated positron emitter distributions to offer patient-specific information about intra-fractional prostate motion and patient position variability during proton beam delivery. This data proved helpful in determining patient-specific planning target volume (PTV) margins. The latest generation in beam dual-head PET prototypes was recently proposed with improved performances. In particular, ultra-fast time-of-flight detectors with time resolution below 10 ps [236] would allow the direct localization of the annihilation events and the reconstruction of

the 3D activity distribution with minimal degradation of the image due to the limited angle geometry (see Sect. 6.6). Other interesting approaches rely on the possibility of detecting short-lived positron emitters like ^{12}N ($T_{1/2} = 11$ ms) with dual head PET systems stand-alone [237, 238]. The detection of such radionuclides could in principle allow almost immediate feedback on the dose delivery, being minimally influenced by biological washout and by previously produced radioactivity.

Completely different approaches undertaken to overcome the limitations of the dual head geometry are those based on special full-rings featuring both a dual ring and a slanted or axially-shifted single-ring configuration leaving an opening for the beam path. This option has been made viable by the depth-of-interaction capability of the PET detectors, enabling the exploitation of obliques line of response [239]. This system has been used at HIMAC in Chiba Japan to visualize the full path of ^{11}C ions across the body [240], renewing the interest of PET range verification with radioactive beams now that facilities with high-intensity beams are in construction [241]. Advances in detector technology and data processing enabled to investigate other imaging methodologies, like a combination of PET and charged particle trackers [242, 243], triple coincidence detection of annihilation and prompt gammas (e.g., in the decay of ^{10}C and ^{14}O) [244], or visualization of the positronium mean lifetime [245].

FLASH Therapy is an emerging, clinically not-yet-practiced single-fraction modality of ultra-high dose of up to about 40 Gy delivered in less than 200 ms. It achieves an instantaneous dose rate that is several orders of magnitude higher than what is currently used in conventional clinical radiotherapy. There are experiments indicating that FLASH radiotherapy results in a surprising, not yet understood, and unexpectedly promising better sparing effect of the healthy tissues. Recently, the first-ever PET imaging of a FLASH proton beam at the Proton Center of the MD Anderson Cancer Center has been demonstrated [246]. Two scintillating LYSO crystal arrays, read out by silicon photomultipliers, were used to collect annihilation gammas from a cylindrical PMMA phantom irradiated by a FLASH proton beam. Preliminary results yielded quantitative imaging and dosimetry of beam-activated isotopes in the PMMA phantom. By incorporating in-beam quasi-real-time range verification, the precision and safety of proton FLASH therapy could be substantially enhanced.

9.8 Impact of artificial intelligence in PET

Artificial intelligence (AI) is having a major influence on many aspects of our lives, and nuclear medicine is no exception. Although the application of AI techniques in the field of PET is at its very early stage, they have already demonstrated their capability in many aspects of image formation, post-processing and image analysis, including direct image reconstruction, attenuation correction, segmentation, noise reduction and quantitative analysis, even if the full potential is yet to be discovered [247, 248]. Some of the most promising applications of AI techniques in PET are described below.

AI for PET image reconstruction The capability of deep learning methods in solving complex inverse problems is well known and image reconstruction from projections seems to be well suited for their application. In fact, AI for medical image reconstruc-

tion has been proposed since the early 1980s [249]. Still, it was only when technological advances made available large amounts of computational power at inexpensive costs that artificial Neural Networks (NN) and Deep Learning (DL) started to be widely adopted. Since 2018, the use of deep NN specifically for PET image reconstruction has been increasingly published in the literature [250–253]. An approach where PET images are directly derived from scanner data, either represented as listmode data or in the form of a set of sinograms, is more complex to realize but also more potentially rewarding. In this case, the algorithm is trained to learn the direct non-linear mapping between the projection and the image space. Several works have been done in the direction of the use of a data-driven supervised learning method, such as DeepPET [251] and AUTOMAP [254]. The AI models trained with this approach are huge but can potentially be fully autonomous, eliminating the need for conventional reconstruction software and significantly shortening the reconstruction time. Despite neglecting the underlying physics, these methods have shown encouraging results. For example, the Deep PET method has achieved similar performance to standard OS-EM with less noise and an acceleration in reconstruction time of a factor $\sim$100. This approach has a more significant possible return, but it faces several difficulties. Extensive models are required to have good quality in the reconstructed image, and enormous training datasets are needed. Moreover, if the AI is trained using images reconstructed with standard software, it is generally unlikely that it will be able to improve quality over that very software. This approach also strictly limits the amount of data used to train the models to the number of existing images that can be acquired. If the model is instead trained with simulations, it may overfit the training set and could not generalize well to real-world images. Indeed, the introduction of excessively parameterizable AI methods is met with skepticism by the nuclear medicine community due to the ethical consideration that a "black box" reconstruction approach would entail. Other groups followed a more "informed" approach. For example, the so-called "Direct-PET" method, uses a dedicated fully-connected layer in the NN to learn the Radon transform. "Softer" strategies have been also explored in the form of a combination of analytical image reconstruction algorithms and AI approaches to reach an optimized solution to the image reconstruction problem [255]. A further step towards a true "physics informed" image reconstruction is a more selective incorporation of AI in the standard iterative reconstruction process. This approach uses smaller models, it requires less training data and time and is less prone to overfitting than the other methods above. It is also more likely to introduce significant improvements than the first approach, as shown by, e.g., the EM-NET [256] and FBSEM-NET [257].

AI for attenuation correction Most of the methods used in PET to correct for the attenuation in the patient rely on patient-specific μ-maps derived from CT images (see 7.4). With the advent of combined PET/MR scanners, the lack of a reliable method for the derivation of attenuation coefficients has stimulated the research around the generation of μ-maps from MR images. Available methods typically start from specialized MR sequences such as ultrashort- or zero-echo-time sequences, followed by material segmentation. A promising alternative approach is to directly derive pseudo-CT images from specialized MR images. Interesting results have been obtained in this field for pelvis [258] and brain [259] PET/MR. Techniques for deriving simultaneously the activity and the attenuation maps in whole-body imaging using a convolutional

neural network approach have been also explored using PET/MR [260]. The possibility of obtaining pseudo-images from other modalities has inspired the idea of deriving μ-maps from the residual morphological information of PET images or even directly producing attenuation-corrected PET images from the corresponding non-attenuation-corrected counterpart. Examples of this approach have been demonstrated in brain imaging [261]. More advanced algorithms using Generative Adversarial Networks (GANs, i.e., model that consists of two neural networks, a generator, and a discriminator, that work together to generate and evaluate data, often used for creating realistic image) have been demonstrated to be also effective for whole body imaging. This opens the possibility of CT-less PET scans, which could lead to a return of cheaper PET-only scanners. Thanks to the dose spared to the patient this can pave the way towards the use of PET for screening, especially if this AI-based attenuation correction is used in combination with LAFOV-PET scanners (see Sect. 9.4) which have the potential for very low-dose imaging.

Image denoising PET images taken at low doses or with very short time frames are typically affected by a higher Poisson noise leading to a low image quality which limits their clinical use. Even if the dose is not a major issue in PET scans, its reduction could widen the target population, while a faster scan could enable a higher temporal frame dynamic scan and be also beneficial to diminish scanning time for critical patients like elderly people, patients with neurodegenerative diseases and those suffering from pain. Today, the possibility of low-dose or fast scanning options is offered by LAFOV-PET scanners, but it is currently unthinkable that their use could extend to clinical routine. An aid for enabling both options comes from the use of AI techniques which apply in the image space. In this sort of image-to-image translation, the model is trained to produce regularized or even virtually noise-free images from already-reconstructed images [262]. Although this approach can only enhance features already present in the reconstructed image and in principle lacks the foundations to bring significant image quality improvements, encouraging results have been obtained in brain imaging. Exploiting the high-resolution priors from MR images and using convolutional neural networks, U-net architectures or unsupervised deep learning, with a dose reduction up to 99% can be obtained with no degradation of image quality [263–265]. The need for MR priors is a strong limiting factor for the clinical application of these methods. The help comes from more advanced algorithms like unsupervised GANs to obtain a significant dose reduction by using PET/CT images only [266]. In the last year, research in this field has been prolific with a constant stream of research papers and new ideas, and the potential, theoretical foundations and possible limitations have still to be fully understood. Even if the denoising of PET images seems to be the most promising application of AI-based image enhancement other valuable applications are resolution modeling and motion correction. It should be not surprising that most of these features are widely experimented in computational photography where AI is today a widely diffused reality even in mobile devices such as smartphones [267].

AI in detectors The use of artificial intelligence (AI) and neural networks has also extended to the level of PET detectors, contributing to advancements in imaging technology. In particular, the development of monolithic scintillators and the integration of neural networks have shown promise in improving PET image quality and performance. Monolithic scintillators consist of a single, continuous scintillation crystal

typically coupled to an array of photodetectors. AI techniques, such as neural networks, can be applied to optimize the performance of monolithic scintillators. Neural networks have the ability to learn and extract complex patterns from data, making them well suited for tasks such as event positioning. Event positioning refers to accurately determining the location of gamma-ray interactions within the detector. Neural networks can be trained to learn the complex relationship between the scintillation light distribution and the position of the interaction event and their integration with event positioning algorithms can improve event positioning accuracy.

In the last few years, various approaches have been used to improve positioning accuracy in monolithic detectors. For example, AI-based methods were used to estimate 2D or DOI position, only using gradient tree boosting [268] or deep neural networks [269] approaches, respectively. Deep neural networks have been demonstrated to be also suitable to accurately estimate the 3D coordinates of gamma-ray interactions within the detector improving the positioning accuracy compared to traditional algorithms [270]. One of the relevant issues with this approach is represented by the NN training. Measurement-based approaches typically require long calibration times. For example, a 2D position network can be trained by hitting the crystals in hundreds of known positions on a regular grid on the crystal surface. The need for fine collimation reduces the counting rate but still high counting statistics for each point are required for effective NN training. Alternatively, training methods based on Monte Carlo simulation can be used, but with the difficulty in realistic reproducing the detection process including scintillation, light transport, signal digitization and the possible inter-detector differences. The determination of the time of the impact of the γ-ray in a monolithic detector is also a highly non-linear problem. In fact, each photodetector can provide its own timestamp and energy measurement for a given event. Analytical approaches for the derivation of the impact time are typically based on energy weighting of the various timestamps [271], but they can hardly reach the same performance as pixel-based detectors. Convolutional neural networks have been first proposed to estimate the interaction time using the waveforms of the photodetector signals [272]. Although effective, this approach is difficult to implement for the hard scalability of data acquisition systems capable of recording the whole waveform.

A notable work in this field which aims to synergistically solve the time and 3D positioning problem in monolithic crystals was proposed by Carra et al. [273]. In this case, a timestamping algorithm based on neural networks provides a first estimation of the arrival time t while a second neural network estimates the 3D event position with the aid of a few engineered features. Then, a third neural network receives the outputs of the first two, e.g., x, y, z, t and energy and refines their estimation using the mutual information. In fact, it is well known that, for example, the estimation of t is affected by z for the delay in the transit time for different depths of interactions. A key method implemented in this work is a sort of hybrid NN training using both experimental and simulation data. For the measurements, 90° and 45° irradiations were used to provide the ground truth for 2D and DOI values, respectively, while the coincidence with a faster detector is taken as the reference value for the time estimation. The simulation also includes a custom-made module for the reproduction of the SiPM signal waveform as a key element to reproduce the variability in the estimation of the timestamps. A further feature of this method is the size of the neural networks

which result lightweight enough to be implemented in FPGAs or GPUs for real-time processing. The proposed method achieved superior positioning accuracy compared to other AI-based positioning and timing algorithms, with a 3D PSF smaller than 1 mm^3 and a CTR of 150 ps when applied on a 51 mm × 51 mm × 12 mm thick LYSO crystal coupled to an array of 256 SiPMs with a pitch of 3.2 mm.

In summary, artificial intelligence techniques have a profound impact on positron emission tomography (PET) imaging, advancing image reconstruction, denoising, and quantitative analysis. AI-based methods have demonstrated improved accuracy and efficiency in attenuation correction, lesion detection, noise reduction, motion correction, and quantitative assessment and their continuous integration in PET imaging holds great promise for further advancements in diagnostic accuracy, patient care, and personalized medicine. AI techniques have been also demonstrated to be effective in boosting detector performance but is expected that the use of AI could also help make them more cost-effective. For example, interesting preliminary results have been obtained on BGO-based monolithic scintillators showing LYSO-like performance enabling BGO for cheaper TOFPET/CT systems or even for total-body scanners [194].

9.9 Social, environmental and economic sustainability of PET

The PET is one important pillar of diagnostic medical imaging especially in oncology and neuroscience. This is due to its quantitation capability and to the radiotracers availability that are specific for making a differential diagnosis, e.g., inflammation versus cancer. As an example, such a capability has been used for studying post-Covid inflammation [274]. PET is an expensive medical device both for its installation and operational activity, because of the two components: the tracers and the scanner. On the other hand, its importance for cancer diagnosis, therapy selection, therapy planning, and post-therapy follow-up is well established. The "Lancet Oncology Commission on Medical Imaging and Nuclear Medicine" in 2021 issued a document [275] that highlights the social need to increase patient access to active cancer imaging worldwide. This recommendation applies to all medical imaging devices and particularly to PET. However, the installation of a complete PET facility, which includes the scanner and the radiotracers availability (either by production in-house with a cyclotron or by delivery from an external company), plus the medical personnel, is very expensive and not all the newly developed countries could afford to install the needed number of devices. Eurostat estimated the number of PET/CT installed in the European countries is equal to 0.19 every 100,000 inhabitants [276]. In this respect, an interesting example is given by the analysis made in 2021 to evaluate the possibility of integrating one PET/CT facility into the national Health System for the 850,000 citizens of Cyprus [277]. The authors proved that this solution is not financially viable, and the Cyprus citizens must rely on the private sector or abroad facilities, with reimbursement by the State. Hence, it is evident that a PET facility cannot be available to the citizens of low- and middle-income countries. This suggests that the effort in technology should be maximum in trying to reduce the cost of the scanner and the radiotracers production/distribution to improve access to early cancer diagnosis worldwide. Furthermore,

it must be reminded that the activity that is injected with the radiotracer into the patient who has a PET exam should be taken under control until the level of activity is below the limits, as given by the radioprotection rules for the patient, the population at large, and the environment. Hence, it would be desirable to reduce the activity to be injected, alas without impairing the diagnostic performance of the exam. This requires a higher efficiency scanner, e.g., LAFOV (see Sect. 9.4) and/or ultra-fast timing PET (see Sect. 9.6). In conclusion, it is auspicious for the technological development of PET to go towards the direction of both economic and environmental sustainability.

10 Conclusions and future outlook

This review means to be a comprehensive compendium of the history, the basic physics principles, the current technologies, the most recent advancements, and the major applications of PET in clinical and pre-clinical PET imaging. It also includes a description of the most recent hybrid types of tomographs, e.g., PET/MR, and of novel PET applications, such as quality assurance in hadrontherapy. In the last section of this review, we summarize the recent developments and we provide an outlook of the future outcomes.

10.1 The first 65 years of PET

Positron Emission Tomography was a newborn technique more than 70 years ago when the first proof-of-principle was made in 1951 at MGH (see Sect. 1). In the next 30 years, PET had an impressive technological development to provide the performance of spatial resolution and sensitivity that were required for the new fields such as cardiology and neurology. By the new century, PET has become the medical imaging technique of choice in oncology applications for the diagnosis, staging and prognosis of cancer lesions. The development of radiation detectors in the field of nuclear and particle physics has had a terrific impact on medical imaging, particularly on PET, which is one of the best examples of successful technology transfer from fundamental physics research to applied Medical Physics. The massive use in Nuclear Physics and High Energy Physics of position-sensitive gas detectors, high-Z and high-density scintillators coupled to Photomultiplier (PMT) and Position-Sensitive Photomultipliers (PS-PMT) and solid-state detectors APD and SiPM, have triggered a series of novel applications, moving towards high-resolution/high-sensitivity pre-clinical devices and large field-of-view 3D PET tomographs. The accelerated scientific progression in genetics and molecular biology has posed additional challenges not only in the technology of radiation detectors, but more and more in the ASIC electronics, fast digital readout, and parallel software.

10.2 The last 10 years of PET development

The target is now to make clinical TOFPET systems with an increased coincidence time resolution (less than 100 ps FWHM), so as to improve the spatial resolution,

the signal-to-noise ratio and then the quantitation accuracy of a PET measurement. It is now clear that the next step in healthcare, the so-called personalized medicine (see Sect. 2) requires a combination of various techniques. In this respect, PET is and will continue to be fundamental due to its high sensitivity at picomolar level and the exquisite richness of information that can provide. The photodetectors are now always solid-state detectors, mainly SiPM (see Sect. 9.1) and the data acquisition is now completely digital, often integrated on-chip and with an increasing utilization of Field Programmable Gate Array (FPGA). The hybrid device PET/CT (see Sect. 7.2) and the most recent one, PET/MR (see Sect. 9.3), are clear examples of the increased value of PET. New multi-modal tracers are being under study. These are labeled both with a positron emitter and a paramagnetic radioisotope, e.g., ^{68}Ga and ^{67}Ga, respectively. 18F-FDG PET has now become a mandatory clinical investigation to be done before any treatment planning system (TPS) in radiotherapy. 18F-FLT and 18F-F-MISO have joined 18F-FDG in the study of the biology of tumor, for "avid" and hypoxic tumor, respectively. PET has also become one of the most reliable techniques for quality assurance in hadrontherapy (see Sect. 9.7). New developments are also in the field of LAFOV-PET, organ-specific scanners, ultra-fast timing detectors and AI. It is expected that future technical developments on PET will be mainly devoted to further increasing imaging sensitivity for enabling novel applications and expanding the use of PET towards new target populations. LAFOV-PET (see Sect. 9.4), Organ-specific PET systems (see Sect. 9.5) and ultra-fast timing TOFPET with or without the Cerenkov effect (see Sect. 9.6) are different strategies to approach this problem each with its advantages and compromises. LAFOV-PET/CT complement the high sensitivity with the possibility to perform full kinetic studies and true quantitative imaging, but the high cost could limit the widespread adoption in the clinics. Organ-specific PET targets high spatial resolution performance but the dedicated approach often results in performance compromises and could make these systems not cost-effective for hospitals. Ultra-fast timing PET detectors can boost the sensitivity of standard geometry scanners, but the present technology limits the ultimate performance and the 20 ps target is still a distant dream. Finally, Artificial Intelligence has been extremely fast in the last years to revolutionize various aspects of PET imaging with exciting applications in image reconstruction and in boosting detector performance, but the field in which a more immediate contribution is expected is image denoising which can be seen as a sort of artificial sensitivity augmentation.

10.3 What next?

The impact of AI in Medicine and in Medical Imaging will be rapidly increasing. Currently, the primary constraint is the limited accessibility of training datasets. However, if there is widespread access to a substantial amount of data for training algorithms, the potential of AI could be unleashed to an extent that is currently beyond full imagination. It is well known that the use of AI in many fields of applications and even more in medicine requires a regulatory framework to be defined. The European Commission has very recently proposed the first-ever legal framework on AI, which addresses the risks of AI and positions Europe to play a leading role globally [278]. Hybrid PET/MR

systems are also expected to receive further attention from the scientific community [279]. In fact, liquid helium-free superconducting magnets, already developed in early 2000 [280], are now ready to hit the market and all major manufacturers are developing their own liquid He-free MRI scanners. This is a boost for the use of MRI with increased safety and reduced maintenance expenses and it can also ease the integration with PET. Furthermore, the combination of the metabolic and metabolomic information from the MRI with the molecular information from PET is gaining new interest and a series of new PET as well as combined PET and MR tracers will probably be introduced for oncological, cardiological and neurological clinical studies. Another development topic will be in standard radiotherapy, where there are already systems where a split gradient coil MRI is integrated with a LINAC radiotherapy system [281]. There is an increasing interest in the use of it in combination with a PET/MR system, so as to improve the quality of the planning on a patient-by-patient basis according to the molecular information of the tumor "in-vivo". Also, in the field of particle therapy, an increasing interest in PET quality assurance for ion therapy is expected to have an increasing interest, because of the future possibility of delivering, in the same treatment, different ions to different zones of the tumor according to their biological status. Finally, PET will move from Molecular Imaging to Biological Imaging, when the optical imaging that is now able to obtain a spatial resolution below 1 micron on cell culture will be integrated with PET to study the biology of a tumor. More than 70 years after the first proposal, PET is still alive and kicking and certainly will be so for many years to come.

Author Contributions All the authors contributed to the writing and revision of the paper.

Funding Open access funding provided by Universitá di Pisa within the CRUI-CARE Agreement.

Data availability statement No datasets were either generated or used during the preparation of the current review paper.

Declarations

Conflict of interest The authors have no relevant financial or non-financial interests to disclose.

References

1. J. Radon, Ber. der Sachische Akad. der Wissenschaften Leipzig (Germany) **69**, 262 (1917)
2. W.H. Sweet, N. Engl. J. Med. **245**, 875 (1951)
3. G.L. Brownell, W.H. Sweet, Nucleonics **11**, 40 (1953)
4. D.A. Rich, J. Nucl. Med. Technol. **25**, 4 (1997)

5. Y.L. Yamamoto, C.J. Thompson, E. Meyer, J.S. Robertson, W. Feindel, J. Comput. Assist. Tomogr. **1**, 43 (1977)
6. E.J. Hoffman, S.-C. Huang, M.E. Phelps, J. Comput. Assist. Tomogr. **3**, 299 (1979)
7. S.-C. Huang, E.J. Hoffman, M.E. Phelps, D.E. Kuhl, J. Comput. Assist. Tomogr. **3**, 804 (1979)
8. S.-C. Huang, E.J. Hoffman, M.E. Phelps, D.E. Kuhl, J. Comput. Assist. Tomogr. **4**, 819 (1980)
9. E.J. Hoffman, S.-C. Huang, M.E. Phelps, D.E. Kuhl, J. Comput. Assist. Tomogr. **5**, 391 (1981)
10. E.J. Hoffman, S.-C. Huang, D. Plummer, M.E. Phelps, J. Comput. Assist. Tomogr. **6**, 987 (1982)
11. M.E. Casey, E.J. Hoffman, J. Comput. Assist. Tomogr. **10**, 845 (1986)
12. M. Casey, R. Nutt, IEEE Trans. Nucl. Sci. **33**, 460 (1986)
13. T. Beyer, D.W. Townsend, T. Brun, P.E. Kinahan, M. Charron, R. Roddy, J. Jerin, J. Young, L. Byars, R. Nutt et al., J. Nucl. Med. **41**, 1369 (2000)
14. T.F. Massoud, S.S. Gambhir, Genes Dev. **17**, 545 (2003)
15. ESF Forward look, European Science Foundation, Strasbourg November (2012)
16. European Society of Radiology (ESR), Insights Imaging **6**, 141 (2015)
17. J. Orear, E. Fermi, *Nuclear Physics: A Course Given by Enrico Fermi at the University of Chicago, Midway reprint* (University of Chicago Press, Chicago, 1950)
18. A. Del Guerra, *Ionizing Radiation Detectors for Medical Imaging* (World Scientific Pub, Singapore, 2004)
19. G. Knoll, *Radiation Detection and Measurement* (Wiley, New York, 2010)
20. R. Hagedorn, *Relativistic Kinematics: A Guide to the Kinematic Problems of High-energy Physics, Mathematics Lecture Note Series* (W. A. Benjamin, New York, 1973)
21. W. Heitler, *The Quantum Theory of Radiation, Dover Books on Physics* (Dover Publications, New York, 1954)
22. P. Colombino, B. Fiscella, L. Trossi, Il Nuovo Cimento Ser. 10 **38**, 707 (1965)
23. S. DeBenedetti, C.E. Cowan, W.R. Konneker, H. Primakoff, Phys. Rev. **77**, 205 (1950)
24. S. Mohorovičić, Astron. Nachr. **253**, 93 (1934)
25. M.H. Pirenne, *The Diffraction of X-rays and Electrons by Free Molecules* (The University Press, Oxford, 1946)
26. M. Deutsch, Phys. Rev. **82**, 455 (1951)
27. A. Rich, Rev. Mod. Phys. **53**, 127 (1981)
28. S.E. Derenzo, W.W. Moses, R.H. Huesman, T.F. Budinger et al., *Quantification of Brain Function* (Elsevier Science Publishers, Amsterdam, 1993), p.25
29. D. Townsend, P. Frey, A. Jeavons, G. Reich, H. Tochon-Danguy, A. Donath, A. Christin, G. Schaller et al., J. Nucl. Med. **28**, 1554 (1987)
30. A. Jeavons, R. Chandler, C. Dettmar, IEEE Trans. Nucl. Sci. **46**, 468 (1999)
31. C.W. Van Eijk et al., Phys. Med. Biol. **47**, R85 (2002)
32. R. Lecomte, Eur. J. Nucl. Med. Mol. Imaging **36**, 69 (2009)
33. P. Minié, J. Santiard, D. Scigocki, M. Suffert, S. Tavernier, G. Charpak, Nucl. Instrum. Methods Phys. Res. Sect. A Accel. Spectrom. Detect. Assoc. Equip. **273**, 881 (1988)
34. L. Hyman, Rev. Sci. Instrum. **36**, 193 (1965)
35. M. Moszyński, B. Bengtson, Nucl. Instrum. Methods **158**, 1 (1979)
36. T. Szczsniak, M. Moszynski, A. Nassalski, P. Lavoute, M. Kapusta et al., Fast photomultipliers for tof pet, in *Proceedings of Nuclear Science Symposium Conference Record, 2007*, vol. 4 (IEEE, 2007), p. 2651–2659
37. R. Post, L. Schiff, Phys. Rev. **80**, 1113 (1950)
38. D. Townsend, T. Sprinks, T. Jones, A. Geissbuhler, M. Defrise, M. Gilardi, J. Heather, IEEE Trans. Nucl. Sci. **36**, 1056 (1989)
39. W.W. Moses, Nucl. Instrum. Methods Phys. Res. Sect. A Accel. Spectrom Detect Assoc. Equip. **648**, S236 (2011)
40. B. Cooke, A. Evans, E. Fanthome, R. Alarie, A. Sendyk, IEEE Trans. Nucl. Sci. **31**, 640 (1984)
41. M. Defrise, P.E. Kinahan, D.W. Townsend, C. Michel, M. Sibomana, D. Newport, IEEE Trans. Med. Imaging **16**, 145 (1997)
42. D.L. Bailey, S.R. Meikle, Phys. Med. Biol. **39**, 411 (1994)
43. M. Bentourkia, P. Msaki, J. Cadorette, R. Lecomte, J. Nucl. Med. **36**, 121 (1995)
44. C.S. Levin, M. Dahlbom, E.J. Hoffman, IEEE Trans. Nucl. Sci. **42**, 1181 (1995)
45. S. Grootoonk, T. Spinks, D. Sashin, N. Spyrou, T. Jones, Phys. Med. Biol. **41**, 2757 (1996)
46. L. Shao, R. Freifelder, J.S. Karp, IEEE Trans. Med. Imaging **13**, 641 (1994)

47. J.M. Ollinger, Phys. Med. Biol. **41**, 153 (1996)
48. C.C. Watson, IEEE Trans. Nucl. Sci. **47**, 1587 (2000)
49. S.R. Cherry, S.-C. Huang, IEEE Trans. Nucl. Sci. **42**, 1174 (1995)
50. D.L. Bailey, Eur. J. Nucl. Med. **25**, 774 (1998)
51. F. Natterer et al., *Mathematical Methods in Image Reconstruction* (Siam, New Delhi, 2001)
52. G.L. Zeng, *Medical Image Reconstruction* (Springer, Berlin, 2010)
53. L.A. Shepp, B.F. Logan, IEEE Trans. Nucl. Sci. **21**, 21 (1974)
54. L.A. Shepp, Y. Vardi, IEEE Trans. Med. Imaging **1**, 113 (1982)
55. G. Pratx, L. Xing, Med. Phys. **38**, 2685 (2011)
56. H.M. Hudson, R.S. Larkin, IEEE Trans. Med. Imaging **13**, 601 (1994)
57. D. Strul, R. Slates, M. Dahlbom, S.R. Cherry, P. Marsden, Phys. Med. Biol. **48**, 979 (2003)
58. J. Qi, R.M. Leahy, S.R. Cherry, A. Chatziioannou, T.H. Farquhar, Phys. Med. Biol. **43**, 1001 (1998)
59. A.M. Alessio, P.E. Kinahan, T.K. Lewellen, IEEE Trans. Med. Imaging **25**, 828 (2006)
60. V.Y. Panin, F. Kehren, C. Michel, M. Casey, IEEE Trans. Med. Imaging **25**, 907 (2006)
61. W.A. Kalender, W. Seissler, E. Klotz, P. Vock, Radiology **176**, 181 (1990)
62. A. Brahme, T. Budinger, D. Panetta, M. Demi, D. Belkić, E.F. Alves, B. Persson, K. Belkić, J. Hendry et al., *Comprehensive Biomedical Physics*, vol. 2 (Elsevier, New York, 2014)
63. P. Kinahan, D. Townsend, T. Beyer, D. Sashin, Med. Phys. **25**, 2046 (1998)
64. N. Mullani, J. Markham, M. Ter-Pogossian, V.J. Sank, J. Comput. Assist. Tomogr. **5**, 454 (1981)
65. R. Allemand, C. Gresset, J. Vacher, J. Nucl. Med. **21**, 153 (1980)
66. M. Laval, M. Moszyński, R. Allemand, E. Cormoreche, P. Guinet, R. Odru, J. Vacher, Nucl. Instrum. Methods Phys. Res. **206**, 169 (1983)
67. J. van Sluis, J. de Jong, J. Schaar, W. Noordzij, P. van Snick, R. Dierckx, R. Borra, A. Willemsen, R. Boellaard, J. Nucl. Med. **60**, 1031 (2019)
68. M. Conti, Phys. Med. **25**, 1 (2009)
69. T. Ido, C.-N. Wan, V. Casella, J. Fowler, A. Wolf, M. Reivich, D. Kuhl, J. Label. Compd. Radiopharm. **14**, 175 (1978)
70. L. Sokolov, M. Reivich, C. Kennedy, M. DesRosiers, C. Patlak, K. Pettigrew, O. Sakurada, M. Shiniohara, J. Neurochem. **28**, 897 (1977)
71. M. Phelps, S. Huang, E. Hoffman, C. Selin, L. Sokoloff, D. Kuhl, Ann. Neurol. **6**, 371 (1979)
72. J. Tillisch, R. Brunken, R. Marshall, M. Schwaiger, M. Mandelkern, M. Phelps, H. Schelbert, N. Engl. J. Med. **314**, 884 (1986)
73. M. Dahlbom, E. Hoffman, C. Hoh, C. Schiepers, G. Rosenqvist, R. Hawkins, M. Phelps et al., J. Nucl. Med. **33**, 1191 (1992)
74. C.A. Mathis, B.J. Bacskai, S.T. Kajdasz, M.E. McLellan, M.P. Frosch, B.T. Hyman, D.P. Holt, Y. Wang, G.-F. Huang, M.L. Debnath et al., Bioorg. Med. Chem. Lett. **12**, 295 (2002)
75. E. Lin, A. Alavi, *PET and PET/CT: A Clinical Guide* (Thieme Medical Publishers, New York, 2005)
76. P.E. Valk, D. Delbeke, D.L. Bailey, D.W. Townsend, M.N. Maisey, *Positron Emission Tomography: Clinical Practice* (Springer Science & Business Media, Berlin, 2006)
77. S. Cherry, Y. Shao, R. Silverman, K. Meadors, S. Siegel, A. Chatziioannou, J. Young, W. Jones, J. Moyers, D. Newport et al., IEEE Trans. Nucl. Sci. **44**, 1161 (1997)
78. A.L. Goertzen, Q. Bao, M. Bergeron, E. Blankemeyer, S. Blinder, M. Cañadas, A.F. Chatziioannou, K. Dinelle, E. Elhami, H.-S. Jans et al., J. Nucl. Med. **53**, 1300 (2012)
79. H. Kume, S. Suzuki, J. Takeuchi, K. Oba, IEEE Trans. Nucl. Sci. **32**, 448 (1985)
80. A. Del Guerra, G. Di Domenico, M. Scandola, G. Zavattini, IEEE Trans. Nucl. Sci. **45**, 3105 (1998)
81. N. Belcari, A. Del Guerra, A. Bartoli, D. Bianchi, M. Lazzarotti, L. Sensi, L. Menichetti, M. Lecchi, P.A. Erba, G. Mariani et al., Nucl. Instrum. Methods Phys. Res. Sect. A Accel. Spectrom. Detect. Assoc. Equip. **571**, 18 (2007)
82. A. Bartoli, N. Belcari, A.D. Guerra, S. Fabbri, Simultaneous pet/spect imaging with the small animal scanner YAP-(S) PET, in *Proceedings of Nuclear Science Symposium Conference Record*, vol. 5 (IEEE, 2007), p. 3408–3413
83. R. Pani, M. Cinti, R. Pellegrini, C. Trotta, G. Trotta, L. Montani, S. Ridolfi, F. Garibaldi, R. Scafè, N. Belcari, A.D. Guerra, Nucl. Instrum. Methods Phys. Res. Sect. A Accel. Spectrom. Detect. Assoc. Equip. **504**, 262 (2003). (**Proceedings of the 3rd International Conference on New Developments in Photodetection**)
84. N. Belcari, N. Camarlinghi, S. Ferretti, P. Iozzo, D. Panetta, P.A. Salvadori, G. Sportelli, A. Del Guerra, IEEE Trans. Radiat. Plasma Med. Sci. **1**, 301 (2017)

85. V. Popov, S. Majewski, A. Weisenberger, R. Wojcik, Analog readout system with charge division type output, in *Proceedings of Nuclear Science Symposium Conference Record*, vol. 4 (IEEE, 2001), p. 1937–1940
86. P.D. Olcott, J. Talcott, C.S. Levin, F. Habte, A.M. Foudray et al., IEEE Trans. Nucl. Sci. **52**, 21 (2005)
87. W. Moses, S.E. Derenzo, IEEE Trans. Nucl. Sci. **41**, 1441 (1994)
88. M. Balcerzyk, G. Kontaxakis, M. Delgado, L. Garcia-Garcia, C. Correcher, A.J. Gonzalez, A. Gonzalez, J.L. Rubio, J.M. Benlloch, M.A. Pozo, Meas. Sci. Technol. **20**, 104011 (2009)
89. A. Saoudi, C. Pepin, F. Dion, M. Bentourkia, R. Lecomte, M. Andreaco, M. Casey, R. Nutt, H. Dautet, IEEE Trans. Nucl. Sci. **46**, 462 (1999)
90. J. Seidel, J.J. Vaquero, S. Siegel, W.R. Gandler, M.V. Green, IEEE Trans. Nucl. Sci. **46**, 485 (1999)
91. T.K. Lewellen, Am. J. Roentgenol. **195**, 301 (2010)
92. H. Zaidi, A. Del Guerra, Med. Phys. **38**, 5667 (2011)
93. D. Renker, E. Lorenz, J. Instrum. **4**, P04004 (2009)
94. M.G. Bisogni, M. Morrocchi, Nucl. Instrum. Methods Phys. Res. Sect. A Accel. Spectrom. Detect. Assoc. Equip. (2015). https://doi.org/10.1016/j.nima.2015.09.114
95. K.S. Shah, R. Farrell, R. Grazioso, E.S. Harmon, E. Karplus, IEEE Trans. Nucl. Sci. **49**, 1687 (2002)
96. K.S. Shah, R. Grazioso, R. Farrell, J. Glodo, M. McClish, G. Entine, P. Dokhale, S.R. Cherry, IEEE Trans. Nucl. Sci. **51**, 91 (2004)
97. S. Cova, G. Ripamonti, A. Lacaita, Nucl. Instrum. Methods Phys. Res. Sect. A Accel. Spectrom. Detect. Assoc. Equip. **253**, 482 (1987)
98. S. Cova, A. Longoni, A. Andreoni, R. Cubeddu, IEEE J. Quantum Electron. **19**, 630 (1983)
99. D. Renker, Nucl. Instrum. Methods Phys. Res. Sect. A Accel. Spectrom. Detect. Assoc. Equip. **567**, 48 (2006)
100. G. Collazuol, G. Ambrosi, M. Boscardin, F. Corsi, G.F. Dalla Betta, A. Del Guerra, N. Dinu, M. Galimberti, D. Giulietti, L.A. Gizzi, Nucl. Instrum. Methods Phys. Res. Sect. A Accel. Spectrom. Detect. Assoc. Equip. **581**, 461 (2007)
101. S. España, L.M. Fraile, J.L. Herraiz, J.M. Udías, M. Desco, J.J. Vaquero, Nucl. Instrum. Methods Phys. Res. Sect. A Accel. Spectrom. Detect. Assoc. Equip. **613**, 308 (2010)
102. G. Llosá, N. Belcari, M.G. Bisogni, G. Collazuol, S. Marcatili, P. Barrillon, C. de La Taille, S. Bondil-Blin, N. Dinu, M. Melchiorri, IEEE Trans. Nucl. Sci. **56**, 2586 (2009)
103. S. Gundacker, E. Auffray, N. Di Vara, B. Frisch, H. Hillemanns, P. Jarron, B. Lang, T. Meyer, S. Mosquera-Vazquez, E. Vauthey, Nucl. Instrum. Methods Phys. Res. Sect. A Accel. Spectrom. Detect. Assoc. Equip. **718**, 569 (2013)
104. F. Acerbi, A. Ferri, G. Zappala, G. Paternoster, A. Picciotto, A. Gola, N. Zorzi, C. Piemonte, IEEE Trans. Nucl. Sci. **62**, 1318 (2015)
105. T. Frach, G. Prescher, C. Degenhardt, R. De Gruyter, A. Schmitz, R. Ballizany, The digital silicon photomultiplierprinciple of operation and intrinsic detector performance, in *Proceedings of Nuclear Science Symposium Conference Record* (IEEE, 2009), p. 1959–1965
106. S. Seifert, G. Van der Lei, H.T. Van Dam, D.R. Schaart, Phys. Med. Biol. **58**, 3061 (2013)
107. D.R. Schaart, E. Charbon, T. Frach, V. Schulz, Nucl. Instrum. Methods Phys. Res. Sect. A Accel. Spectrom. Detect. Assoc. Equip. (2015). https://doi.org/10.1016/j.nima.2015.10.078
108. S. Yamamoto, H. Watabe, J. Hatazawa, Phys. Med. Biol. **56**, N227 (2011)
109. A.V. Stolin, S. Majewski, G. Jaliparthi, R.R. Raylman, J. Proffitt, IEEE Trans. Nucl. Sci. **61**, 2433 (2014)
110. S.I. Kwon, J.S. Lee, H.S. Yoon, M. Ito, G.B. Ko, J.Y. Choi, S.-H.H. Lee, I.C. Song, J.M. Jeong, D.S. Lee, J. Nucl. Med. **52**, 572 (2011)
111. V. Schulz, P. Dueppenbecker, C.W. Lerche, A. Gola, A. Ferri, A. Tarolli, C. Piemonte, Sensitivity encoded silicon photomultipliers (sesps): a novel detector design for uniform crystal identification, in *Proceedings of Nuclear Science Symposium and Medical Conference Record* (IEEE, 2011), p. 3027–3029
112. V. Schulz, Y. Berker, A. Berneking, N. Omidvari, F. Kiessling, A. Gola, C. Piemonte, Phys. Med. Biol. **58**, 4733 (2013)
113. J. Joung, R.S. Miyaoka, T.K. Lewellen, Nucl. Instrum. Methods Phys. Res. Sect. A Accel. Spectrom. Detect. Assoc. Equip. **489**, 584 (2002)
114. T.E. Peterson, L.R. Furenlid, Phys. Med. Biol. **56**, R145 (2011)
115. X. Li, C. Lockhart, T.K. Lewellen, R.S. Miyaoka, IEEE Trans. Nucl. Sci. **58**, 590 (2011)

116. G. Llosa, J. Barrio, C. Lacasta, M.G. Bisogni, A. Del Guerra, S. Marcatili, P. Barrillon, S. Bondil-Blin, C. de La Taille, C. Piemonte, Phys. Med. Biol. **55**, 7299 (2010)
117. M. Morrocchi, G. Ambrosi, M.G. Bisogni, P. Cerello, F. Corsi, M. Ionica, N. Marino, C. Marzocca, F. Pennazio, G. Pirrone, Nucl. Instrum. Methods Phys. Res. Sect. A Accel. Spectrom. Detect. Assoc. Equip. **732**, 603 (2013)
118. R.M. Gray, A. Macovski, IEEE Trans. Nucl. Sci. **23**, 849 (1976)
119. W.C. Hunter, H.H. Barrett, L.R. Furenlid, IEEE Trans. Nucl. Sci. **56**, 189 (2009)
120. Z. Li, M. Wedrowski, P. Bruyndonckx, G. Vandersteen, Phys. Med. Biol. **55**, 6515 (2010)
121. D. Bonifacio, M. Moralles, Modeling of 3d gamma interaction position in a monolithic scintillator block with a row-column summing readout, in *Proceedings of Nuclear Science Symposium Conference Record* (IEEE, 2012), p. 2606–2613
122. Y. Wang, W. Zhu, X. Cheng, D. Li, Phys. Med. Biol. **58**, 1375 (2013)
123. A. Kuhn, S. Surti, J.S. Karp, G. Muehllehner, F.M. Newcomer, R. VanBerg, IEEE Trans. Nucl. Sci. **53**, 1090 (2006)
124. S. Seifert, H.T. van Dam, J. Huizenga, R. Vinke, P. Dendooven, H. Löhner, D.R. Schaart, Phys. Med. Biol. **57**, 2219 (2012)
125. C. Degenhardt, P. Rodrigues, A. Trindade, B. Zwaans, O. Mulhens, R. Dorscheid, A. Thon, A. Salomon, T. Frach, Performance evaluation of a prototype positron emission tomography scanner using digital photon counters (dpc), in *Proceedings of Nuclear Science Symposium Conference Record* (IEEE, 2012), p. 2820–2824
126. M. Miller, J. Griesmer, D. Jordan, T. Laurence, R. Muzic, M. Narayanan, D. Natarajamani, K.-H.H. Su, S. Wang, J. Nucl. Med. **55**, 658 (2014)
127. M. Miller, J. Zhang, K. Binzel, J. Griesmer, T. Laurence, M. Narayanan, D. Natarajamani, S. Wang, M. Knopp, J. Nucl. Med. **56**, 434 (2015)
128. N.C. Nguyen, J.L. Vercher-Conejero, A. Sattar, M.A. Miller, P.J. Maniawski, D.W. Jordan, R.F. Muzic, K.-H.H. Su, J.K. O'Donnell, P.F. Faulhaber, J. Nucl. Med. **56**, 1378 (2015)
129. S. Vandenberghe, P.K. Marsden, Phys. Med. Biol. **60**, R115 (2015)
130. D.A. Torigian, H. Zaidi, T.C. Kwee, B. Saboury, J.K. Udupa, Z.-H.H. Cho, A. Alavi, Radiology **267**, 26 (2013)
131. N.L. Christensen, B.E. Hammer, B.G. Heil, K. Fetterly, Phys. Med. Biol. **40**, 691 (1995)
132. A.J. Lucas, R.C. Hawkes, R.E. Ansorge, G.B. Williams, R.E. Nutt, J.C. Clark, T.D. Fryer, T.A. Carpenter, Technol. Cancer Res Treat **5**, 337 (2006)
133. H. Zaidi, N. Ojha, M. Morich, J. Griesmer, Z. Hu, P. Maniawski, O. Ratib, D. Izquierdo-Garcia, Z.A. Fayad, L. Shao, Phys. Med. Biol. **56**, 3091 (2011)
134. B.J. Pichler, H.F. Wehrl, A. Kolb, M.S. Judenhofer, Positron emission tomography/magnetic resonance imaging: the next generation of multimodality imaging? in *Proceedings of Seminars in Nuclear Medicine*, vol. 38 (Elsevier, 2008), p. 199–208
135. G. Delso, S. Fürst, B. Jakoby, R. Ladebeck, C. Ganter, S.G. Nekolla, M. Schwaiger, S.I. Ziegler, J. Nucl. Med. **52**, 1914 (2011)
136. S.H. Maramraju, S.D. Smith, S.S. Junnarkar, D. Schulz, S. Stoll, B. Ravindranath, M.L. Purschke, S. Rescia, S. Southekal, J.-F.F. Pratte, Phys. Med. Biol. **56**, 2459 (2011)
137. A. Kolb, H.F. Wehrl, M. Hofmann, M.S. Judenhofer, L. Eriksson, R. Ladebeck, M.P. Lichy, L. Byars, C. Michel, H.-P.P. Schlemmer, Eur. Radiol. **22**, 1776 (2012)
138. G.E. Healthcare, http://www3.gehealthcare.com, document ID: JB26282XX (website Accessed 3 July 2015)
139. C. Levin, G. Glover, T. Deller, D. McDaniel, W. Peterson, S.H. Maramraju, J. Nucl. Med. **54**, 148 (2013)
140. B. Weissler, P. Gebhardt, P. Diippenbecker, B. Goldschmidt, A. Salomon, D. Schug, J. Wehner, C. Lerche, D. Wirtz, W. Renz, Design concept of world's first preclinical pet/mr insert with fully digital silicon photomultiplier technology, in *Proceedings of Nuclear Science Symposium Conference Record* (IEEE, 2012), p. 2113–2116
141. B. Weissler, P. Gebhardt, P. Dueppenbecker, J. Wehner, D. Schug, C. Lerche, B. Goldschmidt, A. Salomon, I. Verel, E. Heijman, M. Perkuhn, D. Heberling, R. Botnar, F. Kiessling, V. Schulz, IEEE Trans. Med. Imaging **34**, 2258 (2015)
142. D. Schug, J. Wehner, B. Goldschmidt, C. Lerche, P. Dueppenbecker, P. Hallen, B. Weissler, P. Gebhardt, F. Kiessling, V. Schulz, IEEE Trans. Nucl. Sci. **62**, 669 (2015)

143. J. Wehner, B. Weissler, P.M. Dueppenbecker, P. Gebhardt, B. Goldschmidt, D. Schug, F. Kiessling, V. Schulz, Phys. Med. Biol. **60**, 2231 (2015)
144. D. Schug, J. Wehner, P. Dueppenbecker, B. Weissler, P. Gebhardt, B. Goldschmidt, T. Solf, F. Kiessling, V. Schulz, IEEE Trans. Nucl. Sci. **62**, 658 (2015)
145. G. Borasi, F. Fioroni, A. Del Guerra, G. Lucignani, Eur. J. Nucl. Med. Mol. Imaging **37**, 1629 (2010)
146. D. Crosetto, The 3d complete body screening (3d-cbs) features and implementation, in *Proceedings of 2003 IEEE Nuclear Science Symposium. Conference Record (IEEE Cat. No.03CH37515)*, vol. 4 (2003) p. 2415–2419
147. L. Eriksson, D. Townsend, M. Conti, C. Melcher, M. Eriksson, B.W. Jakoby, H. Rothfuss, M. Casey, B. Bendriem, Potentials for large axial field of view positron camera systems, in *Proceedings of 2008 IEEE Nuclear Science Symposium Conference Record*, p. 1632–1636 (2008)
148. N.E. PET Clin., **15**, 453 (2020)
149. M. Conti, B. Bendriem, M. Casey, L. Eriksson, B. Jakoby, W.F. Jones, J. Jones, C. Michel, C. Nahmias, V. Panin, IEEE Trans. Nucl. Sci. **53**, 1136 (2006)
150. M. Watanabe, K. Shimizu, T. Omura, N. Sato, M. Takahashi, T. Kosugi, K. Ote, A. Katabe, R. Yamada, T. Yamashita, A high-throughput whole-body pet scanner using flat panel ps-pmts, in *Proceedings of Nuclear Science Symposium Conference Record*, vol. 4 (IEEE, 2003), p. 2442–2446
151. X. Zhang, J. Zhou, G. Wang, J. Poon, S. Cherry, R. Badawi, J. Qi, J. Nucl. Med. **55**, 269 (2014)
152. S.R. Cherry, T.K.J.Q.J.M.W.B.R. Jones, J. Nucl. Med. **59**, 3 (2018)
153. G.A. Prenosil, H. Sari, M. Fürstner, A. Afshar-Oromieh, K. Shi, A. Rominger, M. Hentschel, J. Nucl. Med. **63**, 476 (2022)
154. S.M.P.K.J. Vandenberghe, EJNMMI Phys. **7** (2020)
155. M.F. Kircher, S.S. Gambhir, Nat. Rev. Clin. Oncol. **8**, 677 (2011)
156. T.Z.Y.S.H.L.H.Z.X.W.G.P.P.B.R.C.S.J.T. Feng, J. Nucl. Med. **62**, 738 (2021)
157. X. Zhang, S.R. Cherry, Z. Xie, H. Shi, R.D. Badawi, J. Qi, Proc. Natl. Acad. Sci. **117**, 2265 (2020)
158. H. Zaidi, N. Karakatsanis, Br. J. Radiol. **91**, 20170508 (2018)
159. S.-C. Huang, Nucl. Med. Biol. **27**, 643 (2000)
160. P. Zanotti-Fregonara, K. Chen, J.-S. Liow, M. Fujita, R.B. Innis, J. Cereb. Blood Flow Metab. **31**, 2011 (1986)
161. N.A. Karakatsanis, M.E. Casey, M.A. Lodge, A. Rahmim, H. Zaidi, Phys. Med. Biol. **61**, 5456 (2016)
162. J. van Sluis, J.H. van Snick, A.H. Brouwers, W. Noordzij, R.A. Dierckx, R.J. Borra, A.A. Lammertsma, A.W. Glaudemans, R.H. Slart, M. Yaqub et al., EJNMMI Phys. **9**, 1 (2022)
163. Y. Wu, T. Feng, Y. Shen, F. Fu, N. Meng, X. Li, T. Xu, T. Sun, F. Gu, Q. Wu et al., Med. Phys. **49**, 4529 (2022)
164. Y. Li, J. Hu, H. Sari, S. Xue, R. Ma, S. Kandarpa, D. Visvikis, A. Rominger, H. Liu, K. Shi, Eur. J. Nucl. Med. Mol. Imaging **50**, 701 (2023)
165. A. Dimitrakopoulou-Strauss, L. Pan, C. Sachpekidis, Eur. J. Nucl. Med. Mol. Imaging **1** (2023)
166. R.H.J.A.T.C.G.A. Slart, et al., Eur. J. Nucl. Med. Mol. Imaging **7**, 4236–4245 (2021)
167. M.B. Reed, M.P. de León, C. Vraka, I. Rausch, G.M. Godbersen, V. Popper, B.K. Geist, A. Komorowski, L. Nics, C. Schmidt et al., Neuroimage **271**, 120030 (2023)
168. L.K.S. Sundar, M. Hacker, T. Beyer, J. Nucl. Med. **64**, 197 (2023)
169. C. Willyard, Nature **590**, 22 (2021)
170. S. Zhu, Y. Jiang, K. Xu, M. Cui, W. Ye, G. Zhao, L. Jin, X. Chen, J. Neuroinflamm. **17**, 1 (2020)
171. M. Dahlbom, Pet imaging: basics and new trends, in *Handbook of Particle Detection and Imaging* (Springer, 2012), p. 935–971
172. A.J. González, F. Sánchez, J.M. Benlloch, IEEE Trans. Radiat. Plasma Med. Sci. **2**, 388 (2018)
173. C. Catana, J. Nucl. Med. **60**, 1044 (2019)
174. K. Wienhard, M. Schmand, M.E. Casey, K. Baker, J. Bao, L. Eriksson, W.F. Jones, C. Knoess, M. Lenox, M. Lercher, IEEE Trans. Nucl. Sci. **49**, 104 (2002)
175. NeuroLF, https://www.positrigo.com/product/ (website Accessed 09 Nov 2023)
176. S. Majewski, J. Proffitt, J. Brefczynski-Lewis, A. Stolin, A. Weisenberger, W. Xi, R. Wojcik, *IEEE Nuclear Science Symposium Conference Record* (2011)
177. K. Gong, S. Majewski, P.E. Kinahan, R.L. Harrison, B.F. Elston, R. Manjeshwar, S. Dolinsky, A.V. Stolin, J.A. Brefczynski-Lewis, J. Qi, Phys. Med. Biol. **61**, 3681 (2016)
178. C.E. Bauer, J. Brefczynski-Lewis, G. Marano, M.-B. Mandich, A. Stolin, P. Martone, J.W. Lewis, G. Jaliparthi, R.R. Raylman, S. Majewski, Brain Behav. **6**, e00530 (2016)

179. H. Herzog, K.-J. Langen, C. Weirich, E. Rota Kops, J. Kaffanke, L. Tellmann, J. Scheins, I. Neuner, G. Stoffels, K. Fischer, L. Caldeira, H. Coenen, N. Shah, Nuklearmedizin. Nucl. Med. **50**, 74 (2011)
180. N.J. Shah, A.-M.M. Oros-Peusquens, J. Arrubla, K. Zhang, T. Warbrick, J. Mauler, K. Vahedipour, S. Romanzetti, J. Felder, A. Celik, J. Magn. Reson. **229**, 101 (2013)
181. J.M. Benlloch, A.J. González, R. Pani, E. Preziosi, C. Jackson, J. Murphy, J. Barberá, C. Correcher, S. Aussenhofer, D. Gareis et al., Eur. Psychiatry **50**, 21–27 (2018)
182. A. Del Guerra, S. Ahmad, M. Avram, N. Belcari, A. Berneking, L. Biagi, M.G. Bisogni, F. Brandl, J. Cabello, N. Camarlinghi, P. Cerello, C.-H. Choi, S. Coli, S. Colpo, J. Fleury, V. Gagliardi, G. Giraudo, K. Heekeren, W. Kawohl, T. Kostou, J.-L. Lefaucheur, C. Lerche, G. Loudos, M. Morrocchi, J. Muller, M. Mustafa, I. Neuner, P. Papadimitroulas, F. Pennazio, R. Rajkumar, C.R. Brambilla, J. Rivoire, E.R. Kops, J. Scheins, R. Schimpf, N.J. Shah, C. Sorg, G. Sportelli, M. Tosetti, R. Trinchero, C. Wyss, S. Ziegler, Eur. Psychiatry **50**, 7 (2018). (**workshop on Schizophrenia and other mental disorders - S. Frangou (Editor in Chief), A. Del Guerra, S. Galderisi (Guest Editors)**)
183. R. Subramaniam, PET/CT and Patient Outcomes Part I, An Issue of PET Clinics (2015)
184. I. Weinberg, S. Majewski, A. Weisenberger, A. Markowitz, L. Aloj, L. Majewski, D. Danforth, J. Mulshine, K. Cowan, J. Zujewski, Eur. J. Nucl. Med. **23**, 804 (1996)
185. CMR-NAVISCAN, http://cmr-naviscan.com/ (website Accessed 07 Nov 2023)
186. L. Moliner, A.J. Gonzalez, A. Soriano, F. Sánchez, C. Correcher, A. Orero, M. Carles, L.F. Vidal, J. Barberá, L. Caballero, Med. Phys. **39**, 5393 (2012)
187. A. Collarino, V. Fuoco, L. Arias-Bouda, A. Sanchez, L.-F. de Geus-Oei, R. Masetti, R. Olmos, Transl. Cancer Res. **7**, S295 (2018)
188. Y. Satoh, U. Motosugi, M. Imai, H. Onishi, Ann. Nucl. Med. **34**, 119 (2020)
189. Y. Satoh, K. Hanaoka, C. Ikegawa, M. Imai, S. Watanabe, D. Morimoto-Ishikawa, H. Onishi, T. Ito, Y. Komoike, K. Ishii, Diagnostics **13** (2023)
190. T.G. Turkington, T.C. Hawk, R.E. Coleman, M.F. Smith, S. Majewski, B.J. Kross, R. Wojcik, A.G. Weisenberger, T.R. DeGrado, Pet prostate imaging with small planar detectors, in *Proceedings of Nuclear Science Symposium Conference Record*, vol. 5 (IEEE, 2004), p. 2806–2809
191. N. Aubry, E. Auffray, F.B. Mimoun, N. Brillouet, R. Bugalho, E. Charbon, O. Charles, D. Cortinovis, P. Courday, A. Cserkaszky, J. Instrum. **8**, C04002 (2013)
192. M. Zvolsk, *Endotofpet-us-a Miniaturised Calorimeter for Endoscopic Time-of-flight Positron Emission Tomography*, vol. 587 (Institute of Physics Publishing, Bristol, 2015)
193. A.J. Gonzalez, A. Gonzalez-Montoro, PET Clinics (2023)
194. S. Vandenberghe, F.M. Muller, N. Withofs, M. Dadgar, J. Maebe, B. Vervenne, M.A. Akl, S. Xue, K. Shi, G. Sportelli, N. Belcari, R. Hustinx, C. Vanhove, J.S. Karp, Eur. J. Nucl. Med. Mol. Imaging (2023)
195. M. Conti, Eur. J. Nucl. Med. Mol. Imaging **38**, 1147 (2011)
196. M. Toussaint, R. Lecomte, J.-P. Dussault, IEEE Trans. Radiat. Plasma Med. Sci. **5**, 729 (2021)
197. S.I. Kwon, R. Ota, E. Berg, F. Hashimoto, K. Nakajima, I. Ogawa, Y. Tamagawa, T. Omura, T. Hasegawa, S.R. Cherry, Nat. Photonics (2021)
198. G. Schramm, Front. Nucl. Med. **2**, (2022)
199. P. Lecoq, IEEE Trans. Radiat. Plasma Med. Sci. **1**, 473 (2017)
200. D.R. Schaart, S. Ziegler, H. Zaidi, Med. Phys. **47**, 2721 (2020)
201. R.M. Turtos, S. Gundacker, E. Auffray, P. Lecoq, Phys. Med. Biol. **64**, 185018 (2019)
202. T. Ooba, T. Fukushima, H. Kawai, M. Konishi, H. Nakayama, M. Tabata, I. Adachi, S. Nishida, H. Kishimoto, H. Yokogawa Proposal of cherenkov tofpet with silica aerogel, in *Proceedings of Nuclear Science Symposium Conference Record*, vol. 6 (IEEE, 2004), p. 3781–3784
203. M. Miyata, H. Tomita, K. Watanabe, J. Kawarabayashi, T. Iguchi, J. Nucl. Sci. Technol. **43**, 339 (2006)
204. R. Dolenec, S. Korpar, P. Krizan, R. Pestotnik, A. Stanovnik, R. Verheyden, Time-of-flight measurements with cherenkov photons produced by 511 kev photons in lead crystals, in *Proceedings of Nuclear Science Symposium Conference Record* (IEEE, 2010), p. 280–284
205. S. Korpar, R. Dolenec, P. Krizan, R. Pestotnik, A. Stanovnik, Nucl. Instrum. Methods Phys. Res. Sect. A Accel. Spectrom. Detect. Assoc. Equip. **654**, 532 (2011)
206. R. Pestotnik, Il Nuovo Cimento C **43**, 1 (2020)
207. S.E. Brunner, L. Gruber, J. Marton, K. Suzuki, A. Hirtl, Nucl. Instrum. Methods Phys. Res. Sect. A Accel. Spectrom. Detect. Assoc. Equip. **732**, 560 (2013)
208. S.E. Brunner, L. Gruber, J. Marton, K. Suzuki, A. Hirtl, IEEE Trans. Nucl. Sci. **61**, 443 (2014)

209. S. Brunner, D. Schaart, Phys. Med. Biol. **62**, 4421 (2017)
210. J.W. Cates, W.-S. Choong, Phys. Med. Biol. **67**, 195009 (2022)
211. A.D. Francesco, R. Bugalho, L. Oliveira, L. Pacher, A. Rivetti, M. Rolo, J. Silva, R. Silva, J. Varela, J. Instrum. **11**, C03042 (2016)
212. I. Sacco, R. Dohle, P. Fischer, C. Piemonte, M. Ritzert, Nucl. Instrum. Methods Phys. Res. Sect. A Accel. Spectrom. Detect. Assoc. Equip. **824**, 233 (2016)
213. D. Sánchez, S. Gómez, J. Mauricio, L. Freixas, A. Sanuy, G. Guixé, A. López, R. Manera, J. Marín, J.M. Pérez, E. Picatoste, C. Pujol, A. Sanmukh, P. Rato, O. Vela, D. Gascón, IEEE Trans. Radiat. Plasma Med. Sci. **6**, 51 (2022)
214. P. Carra, M. Bertazzoni, M.G. Bisogni, J.M. Cela Ruiz, A. Del Guerra, D. Gascon, S. Gomez, M. Morrocchi, G. Pazzi, D. Sanchez, I. Sarasola Martin, G. Sportelli, N. Belcari, IEEE Trans. Radiat. Plasma Med. Sci. **3**, 549 (2019)
215. S. Gómez, J. Alozy, M. Campbell, J. Fernandez-Tenllado, R. Manera, J. Mauricio, C. Pujol, D. Sanchez, A. Sanmukh, A. Sanuy, R. Ballabriga, D. Gascon, J. Instrum. **17**, C05027 (2022)
216. J.-F. Pratte, F. Nolet, S. Parent, F. Vachon, N. Roy, T. Rossignol, K. Deslandes, H. Dautet, R. Fontaine, S.A. Charlebois, Sensors **21**, (2021)
217. M. Durante, R. Orecchia, J.S. Loeffler, Nat. Rev. Clin. Oncol. **14**, 483 (2017)
218. R.R. Wilson, Radiology **47**, 487 (1946). (**pMID: 20274616**)
219. M. Durante, H. Paganetti, Rep. Prog. Phys. **79**, 096702 (2016)
220. A.-C. Knopf, A. Lomax, Phys. Med. Biol. **58**, R131 (2013)
221. H. Paganetti, Phys. Med. Biol. **57**, R99 (2012)
222. K. Parodi, Nucl. Instrum. Methods Phys. Res. Sect. A Accel. Spectrom. Detect. Assoc. Equip. **809**, 113 (2016). (**Advances in detectors and applications for medicine**)
223. K. Parodi, Med. Phys. **42**, 7153 (2015)
224. W. Enghardt, K. Parodi, P. Crespo, F. Fiedler, J. Pawelke, F. Pönisch, Radiother. Oncol. **73**, S96 (2004)
225. H.D. Maccabee, U. Madhvanath, M.R. Raju, Phys. Med. Biol. **14**, 213 (1969)
226. W. Enghardt, K. Parodi, P. Crespo, F. Fiedler, J. Pawelke, F. Pnisch, Radiother. Oncol. **73**, S96 (2004). (**Carbon-Ion Theraphy**)
227. T. Nishio, A. Miyatake, T. Ogino, K. Nakagawa, N. Saijo, H. Esumi, Int. J. Radiat. Oncol. Biol. Phys. **76**, 277 (2010)
228. M.G. Bisogni, A. Attili, G. Battistoni, N. Belcari, N. Camarlinghi, P. Cerello, S. Coli, A.D. Guerra, A. Ferrari, V. Ferrero, E. Fiorina, G. Giraudo, E. Kostara, M. Morrocchi, F. Pennazio, C. Peroni, M.A. Piliero, G. Pirrone, A. Rivetti, M.D. Rolo, V. Rosso, P. Sala, G. Sportelli, R. Wheadon, J. Med. Imaging **4**, 011005 (2016)
229. E. Fiorina, V. Ferrero, G. Baroni, G. Battistoni, N. Belcari, N. Camarlinghi, P. Cerello, M. Ciocca, M. De Simoni, M. Donetti, Y. Dong, A. Embriaco, M. Fischetti, G. Franciosini, G. Giraudo, A. Kraan, F. Laruina, C. Luongo, D. Maestri, M. Magi, G. Magro, E. Malekzadeh, C. Mancini Terracciano, M. Marafini, I. Mattei, E. Mazzoni, P. Mereu, R. Mirabelli, A. Mirandola, M. Morrocchi, S. Muraro, A. Patera, V. Patera, F. Pennazio, A. Retico, A. Rivetti, M.D. Da Rocha Rolo, V. Rosso, A. Sarti, A. Schiavi, A. Sciubba, E. Solfaroli Camillocci, G. Sportelli, S. Tampellini, M. Toppi, G. Traini, S.M. Valle, F. Valvo, B. Vischioni, V. Vitolo, R. Wheadon, M.G. Bisogni, Front. Phys. **8** (2021)
230. M. Moglioni, A.C. Kraan, G. Baroni, G. Battistoni, N. Belcari, A. Berti, P. Carra, P. Cerello, M. Ciocca, A. De Gregorio, M. De Simoni, D. Del Sarto, M. Donetti, Y. Dong, A. Embriaco, M.E. Fantacci, V. Ferrero, E. Fiorina, M. Fischetti, G. Franciosini, G. Giraudo, F. Laruina, D. Maestri, M. Magi, G. Magro, E. Malekzadeh, M. Marafini, I. Mattei, E. Mazzoni, P. Mereu, A. Mirandola, M. Morrocchi, S. Muraro, E. Orlandi, V. Patera, F. Pennazio, M. Pullia, A. Retico, A. Rivetti, M.D. Da Rocha Rolo, V. Rosso, A. Sarti, A. Schiavi, A. Sciubba, G. Sportelli, S. Tampellini, M. Toppi, G. Traini, A. Trigilio, S.M. Valle, F. Valvo, B. Vischioni, V. Vitolo, R. Wheadon, M.G. Bisogni, Front. Oncol. **12** (2022)
231. X. Zhu, S. España, J. Daartz, N. Liebsch, J. Ouyang, H. Paganetti, T.R. Bortfeld, G.E. Fakhri, Phys. Med. Biol. **56**, 4041 (2011)
232. S.P. Nischwitz, J. Bauer, T. Welzel, H. Rief, O. Jäkel, T. Haberer, K. Frey, J. Debus, K. Parodi, S.E. Combs, S. Rieken, Radiother. Oncol. **115**, 179 (2015)
233. J. Handrack, T. Tessonnier, K. Parodi, Acta Oncol. **56**, 1451 (2017)
234. M. Abe, Proc. Jpn. Acad. Ser. B **83** (2007)
235. W.C. Hsi, D.J. Indelicato, C. Vargas, S. Duvvuri, Z. Li, J. Palta, Med. Phys. **36**, 4136 (2009)

236. P. Lecoq, C. Morel, J.O. Prior, D. Visvikis, S. Gundacker, E. Auffray, P. Križan, R.M. Turtos, D. Thers, E. Charbon, J. Varela, C. de La Taille, A. Rivetti, D. Breton, J.-F. Pratte, J. Nuyts, S. Surti, S. Vandenberghe, P. Marsden, K. Parodi, J.M. Benlloch, M. Benoit, Phys. Med. Biol. **65**, 21RM01 (2020)
237. P. Dendooven, H.J.T. Buitenhuis, F. Diblen, P.N. Heeres, A.K. Biegun, F. Fiedler, M.-J. van Goethem, E.R. van der Graaf, S. Brandenburg, Phys. Med. Biol. **60**, 8923 (2015)
238. I. Ozoemelam, E. van der Graaf, M.-J. van Goethem, M. Kapusta, N. Zhang, S. Brandenburg, P. Dendooven, Phys. Med. Biol. **65**, 245013 (2020)
239. H. Tashima, E. Yoshida, N. Inadama, F. Nishikido, Y. Nakajima, H. Wakizaka, T. Shinaji, M. Nitta, S. Kinouchi, M. Suga, H. Haneishi, T. Inaniwa, T. Yamaya, Phys. Med. Biol. **61**, 1795 (2016)
240. Y. Hirano, H. Takuwa, E. Yoshida, F. Nishikido, Y. Nakajima, H. Wakizaka, T. Yamaya, Phys. Med. Biol. **61**, 2016 (1875)
241. M. Durante, A. Golubev, W.-Y. Park, C. Trautmann, Phys. Rep. **800**, 1 (2019). (**applied nuclear physics at the new high-energy particle accelerator facilities**)
242. M. Toppi, G. Baroni, G. Battistoni, M.G. Bisogni, P. Cerello, M. Ciocca, P. De Maria, M. De Simoni, M. Donetti, Y. Dong, A. Embriaco, V. Ferrero, E. Fiorina, M. Fischetti, G. Franciosini, A.C. Kraan, C. Luongo, E. Malekzadeh, M. Magi, C. Mancini-Terracciano, M. Marafini, I. Mattei, E. Mazzoni, R. Mirabelli, A. Mirandola, M. Morrocchi, S. Muraro, V. Patera, F. Pennazio, A. Schiavi, A. Sciubba, E. Solfaroli-Camillocci, G. Sportelli, S. Tampellini, G. Traini, S.M. Valle, B. Vischioni, V. Vitolo, A. Sarti, Front. Oncol. **11** (2021)
243. G. Traini, I. Mattei, G. Battistoni, M. Bisogni, M. De Simoni, Y. Dong, A. Embriaco, M. Fischetti, M. Magi, C. Mancini-Terracciano, M. Marafini, R. Mirabelli, S. Muraro, V. Patera, A. Schiavi, A. Sciubba, Camillocci E. Solfaroli, S. Valle, A. Sarti, Phys. Med. **65**, 84 (2019)
244. K. Parodi, T. Yamaya, P. Moskal, Z. Med. Phys. **33**, 22 (2023). (**special Issue: Recent Developments in Nuclear Medicine Imaging and Therapy**)
245. P. Moskal, K. Dulski, N. Chug, C. Curceanu, E. Czerwiński, M. Dadgar, J. Gajewski, A. Gajos, G. Grudzień, B.C. Hiesmayr, K. Kacprzak, Łukasz Kapłon, H. Karimi, K. Klimaszewski, G. Korcyl, P. Kowalski, T. Kozik, N. Krawczyk, W. Krzemień, E. Kubicz, P. Małczak, S. Niedźwiecki, M. Pawlik-Niedźwiecka, M. Pędziwiatr, L. Raczyński, J. Raj, A. Ruciński, S. Sharma, S. Null, R.Y. Shopa, M. Silarski, M. Skurzok, E. Stępień, M. Szczepanek, F. Tayefi, W. Wiślicki, Sci. Adv. **7**, eabh4394 (2021)
246. F. Abouzahr, J.P. Cesar, P. Crespo, M. Gajda, Z. Hu, W. Kaye, K. Klein, A.S. Kuo, S. Majewski, O. Mawlawi, A. Morozov, A. Ojha, F. Poenisch, J.C. Polf, M. Proga, N. Sahoo, J. Seco, T. Takaoka, S. Tavernier, U. Titt, X. Wang, X.R. Zhu, K. Lang, Phys. Med. Biol. **68**, 125001 (2023)
247. G. Zaharchuk, G. Davidzon, Artificial intelligence for optimization and interpretation of pet/ct and pet/mr images, in *Proceedings of Seminars in Nuclear Medicine*, vol. 51 (Elsevier, 2021), p. 134–142
248. H. Arabi, A. AkhavanAllaf, A. Sanaat, I. Shiri, H. Zaidi, Phys. Med. **83**, 122 (2021)
249. C. Floyd, IEEE Trans. Med. Imaging **10**, 485 (1991)
250. K. Gong, C. Catana, J. Qi, Q. Li, IEEE Trans. Med. Imaging **38**, 1655 (2018)
251. I. Häggström, C.R. Schmidtlein, G. Campanella, T.J. Fuchs, Med. Image Anal. **54**, 253 (2019)
252. K. Kim, D. Wu, K. Gong, J. Dutta, J.H. Kim, Y.D. Son, H.K. Kim, G. El Fakhri, Q. Li, IEEE Trans. Med. Imaging **37**, 1478 (2018)
253. Z. Liu, H. Chen, H. Liu, Deep learning based framework for direct reconstruction of pet images, in *Proceedings of Medical Image Computing and Computer Assisted Intervention-MICCAI 2019: 22nd International Conference, Shenzhen, China, October 13–17, 2019, Proceedings, Part III 22* (Springer, 2019), p. 48–56
254. B. Zhu, J.Z. Liu, S.F. Cauley, B.R. Rosen, M.S. Rosen, Nature **555**, 487 (2018)
255. A.J. Reader, G. Corda, A. Mehranian, C. da Costa-Luis, S. Ellis, J.A. Schnabel, IEEE Trans. Radiat. Plasma Med. Sci. **5**, 1 (2020)
256. K. Gong, D. Wu, K. Kim, J. Yang, G. El Fakhri, Y. Seo, Q. Li, Emnet: an unrolled deep neural network for pet image reconstruction, in *Proceedings of Medical Imaging 2019: Physics of Medical Imaging*, vol. 10948 (SPIE, 2019), p. 1203–1208
257. A. Mehranian, A.J. Reader, IEEE Trans. Radiat. Plasma Med. Sci. **5**, 54 (2020)
258. A.P. Leynes, J. Yang, F. Wiesinger, S.S. Kaushik, D.D. Shanbhag, Y. Seo, T.A. Hope, P.E. Larson, J. Nucl. Med. **59**, 852 (2018)
259. F. Liu, H. Jang, R. Kijowski, T. Bradshaw, A.B. McMillan, Radiology **286**, 676 (2018)
260. D. Hwang, S.K. Kang, K.Y. Kim, S. Seo, J.C. Paeng, D.S. Lee, J.S. Lee, J. Nucl. Med. **60**, 1183 (2019)

261. F. Liu, H. Jang, R. Kijowski, G. Zhao, T. Bradshaw, A.B. McMillan, EJNMMI Phys. **5**, 1 (2018)
262. C.O. da Costa-Luis, A.J. Reader, IEEE Trans. Radiat. Plasma Med. Sci. **5**, 202 (2020)
263. L. Xiang, Y. Qiao, D. Nie, L. An, W. Lin, Q. Wang, D. Shen, Neurocomputing **267**, 406 (2017)
264. J. Xu, E. Gong, J. Ouyang, J. Pauly, G. Zaharchuk, Ultra-low-dose 18f-fdg brain pet/mr denoising using deep learning and multi-contrast information, in *Proceedings of Medical imaging 2020: Image processing*, vol. 11313 (SPIE, 2020), p. 420–432
265. J. Cui, K. Gong, N. Guo, C. Wu, X. Meng, K. Kim, K. Zheng, Z. Wu, L. Fu, B. Xu et al., Eur. J. Nucl. Med. Mol. Imaging **46**, 2780 (2019)
266. K. Zhao, L. Zhou, S. Gao, X. Wang, Y. Wang, X. Zhao, H. Wang, K. Liu, Y. Zhu, H. Ye, PLoS One **15**, e0238455 (2020)
267. M. Delbracio, D. Kelly, M.S. Brown, P. Milanfar, Ann. Rev. Vis. Sci. **7**, 571 (2021)
268. F. Müller, D. Schug, P. Hallen, J. Grahe, V. Schulz, IEEE Trans. Radiat. Plasma Med. Sci. **2**, 411 (2018)
269. A. Sanaat, H. Zaidi, Appl. Sci. **10**, 4753 (2020)
270. M. Decuyper, M. Stockhoff, S. Vandenberghe, R. Van Holen, Phys. Med. Biol. **66**, 075001 (2021)
271. E. Lamprou, A.J. Gonzalez, F. Sanchez, J.M. Benlloch, Phys. Med. **70**, 10 (2020)
272. E. Berg, S.R. Cherry, Phys. Med. Biol. **63**, 02LT01 (2018)
273. P. Carra, M.G. Bisogni, E. Ciarrocchi, M. Morrocchi, G. Sportelli, V. Rosso, N. Belcari, Phys. Med. Biol. **67**, 135001 (2022)
274. T. Rudroff, C.D. Workman, L.L.B. Ponto, Viruses **13**, 2283 (2021)
275. H. Hricak, M. Abdel-Wahab, R. Atun, M.M. Lette, D. Paez, J.A. Brink, L. Donoso-Bach, G. Frija, M. Hierath, O. Holmberg et al., Lancet Oncol. **22**, e136 (2021)
276. Eurostat (2020). https://ec.europa.eu/eurostat/statistics-explained/index.php?title=Healthcare_resource_statistics_-_technical_resources_and_medical_technology. (Website Accessed 19 Dec 2023)
277. D. Kefallonitou, I. Polycarpou, K. Souliotis, K. Giannakou, Front. Public Health **9**, 607761 (2021)
278. European Commission (2023). https://digital-strategy.ec.europa.eu/en/policies/regulatory-framework-ai. (Website Accessed 19 Dec 2023)
279. S. Musafargani, K.K. Ghosh, S. Mishra, P. Mahalakshmi, P. Padmanabhan, B. Gulyás, Eur. J. Hybrid Imaging **2**, 1 (2018)
280. J. Sakuraba, Y. Mikami, K. Watazawa, K. Watanabe, S. Awaji, Supercond. Sci. Technol. **13**, 12 (2000)
281. E.S. Paulson, E. Ahunbay, X. Chen, N.J. Mickevicius, G.-P. Chen, C. Schultz, B. Erickson, M. Straza, W.A. Hall, X.A. Li, Clin. Transl. Radiat. Oncol. **23**, 72 (2020)